

A Study of the Crab-like Supernova Remnant G21.5-0.9 with  
the Chandra X-ray Observatory

by

Heather Colleen Matheson

A Thesis submitted to the Faculty of Graduate Studies of

The University of Manitoba

in partial fulfilment of the requirements of the degree of

MASTER OF SCIENCE

Department of Physics & Astronomy

University of Manitoba

Winnipeg, Manitoba

Copyright © 2006 by Heather Colleen Matheson

**THE UNIVERSITY OF MANITOBA**  
**FACULTY OF GRADUATE STUDIES**  
\*\*\*\*\*  
**COPYRIGHT PERMISSION**

**A Study of the Crab-like Supernova Remnant G21.5-0.9 with  
the Chandra X-ray Observatory**

**BY**

**Heather Colleen Matheson**

**A Thesis/Practicum submitted to the Faculty of Graduate Studies of The University of  
Manitoba in partial fulfillment of the requirement of the degree**

**OF**

**MASTER OF SCIENCE**

**Heather Colleen Matheson © 2006**

**Permission has been granted to the Library of the University of Manitoba to lend or sell copies of this thesis/practicum, to the National Library of Canada to microfilm this thesis and to lend or sell copies of the film, and to University Microfilms Inc. to publish an abstract of this thesis/practicum.**

**This reproduction or copy of this thesis has been made available by authority of the copyright owner solely for the purpose of private study and research, and may only be reproduced and copied as permitted by copyright laws or with express written authorization from the copyright owner.**

For Dusty.

My best friend through good times and bad.

Thank you for the years of company on all the late nights.

The world would be a darker place without you.

# ACKNOWLEDGEMENTS

This work would not have been possible without all of the support I received during my years at the University of Manitoba.

First and foremost, thank you to Dr. Samar Safi-Harb for the guidance, enthusiasm and encouragement. I am very grateful for the opportunities given to pursue a fascinating research area.

Thank you to my thesis committee, Dr. Jayanne English and Dr. Barbara Sherriff, for taking the time to review my work in detail and provide insightful and useful comments.

I am grateful to have a loving and supportive family. Thank you to my parents, Frank and Lori Matheson, and to my sisters, Gail and Amanda, for their unconditional love and support.

Many thanks to Maiko Langelaar for the computer support and the enthusiasm shown toward astrophysics in general.

Thanks to my fellow graduate students for the comic relief during the coursework. Furthermore, I would like to thank all members of the Department of Physics & Astronomy for making the University of Manitoba a welcoming and friendly place.

I would also like to acknowledge the financial support received from the Natural Sciences and Engineering Research Council (NSERC) of Canada.

This thesis made use of the National Aeronautics and Space Administration's (NASA's) Chandra X-ray Observatory, NASA's Astrophysics Data System (ADS),

and the High Energy Astrophysics Science Archive Research Center (HEASARC) operated at Goddard Space Flight Center (GSFC).

# ABSTRACT

The absence of a supernova remnant (SNR) shell surrounding the Crab and other plerions (pulsar wind nebulae) has been a mystery for three decades. G21.5-0.9 is a particularly intriguing SNR in which the central powering engine (PSR J1833-1034) has been recently detected. Early *Chandra* observations revealed a faint extended X-ray halo which was associated with the SNR shell; however its spectrum was non-thermal, unlike that expected from an SNR shell. On the other hand, a plerionic origin to the halo was problematic since the X-ray plerion would be larger than the radio plerion. This thesis presents the analysis of an integrated 278 ks of archival *Chandra* data acquired with the High-Resolution Camera (HRC) and 579 ks acquired with the Advanced CCD Imaging Spectrometer (ACIS). This study presents the deepest and highest resolution images of any plerionic SNR to date. The resulting images reveal for the first time: (1) a limb-brightened morphology in the eastern section of the halo, (2) a rich structure in the inner (40'' radius) bright plerion including wisps and a double-lobed morphology with an axis of symmetry running in the northwest-southeast direction, and (3) the dynamic nature of the plerion with knots appearing, moving, and disappearing with time. The spatially resolved spectroscopic study indicates that the photon index steepens with increasing distance from the central point source out to a radius of 40'' then becomes constant at  $\sim 2.6$  in the X-ray halo (for a column density of  $N_{\text{H}} = 2.33 \times 10^{22}$  atoms  $\text{cm}^{-2}$ ). Evidence of line emission due to Mg, Si, and S was found in the halo's northern knots, indicating that these features

are shock-heated ejecta from the SN explosion. The limb lacked the evidence for heavy elements, indicating that it is the SNR shell (shock-heated ISM). This study illustrates the need for deep *Chandra* observations to reveal the missing SNR material in Crab-like plerions.

# CONTENTS

<b>Acknowledgements</b>	<b>ii</b>
<b>Abstract</b>	<b>iv</b>
<b>Contents</b>	<b>vi</b>
<b>List of Tables</b>	<b>xi</b>
<b>List of Figures</b>	<b>xii</b>
<b>Preface</b>	<b>xv</b>
<b>1 General Properties of Supernova Remnants</b>	<b>1</b>
1.1 The Life Cycle of a Massive Star . . . . .	2
1.2 Types of Supernovae . . . . .	4
1.2.1 Type II Explosions . . . . .	4
1.2.2 Type Ia Explosions . . . . .	6
1.2.3 Type Ib/Ic Explosions . . . . .	6
1.3 Evolution of a Supernova Remnant . . . . .	7
1.4 Remnants Containing Neutron Stars . . . . .	12
1.4.1 Characteristics of Pulsars . . . . .	17
1.4.2 Characteristics of Pulsar Wind Nebulae . . . . .	19
<b>2 An X-ray View of Supernova Remnants</b>	<b>22</b>

2.1	Thermal Emission From a Hot Gas . . . . .	22
2.2	Synchrotron Radiation From Relativistic Electrons . . . . .	25
2.3	Blackbody Radiation From Star-like Objects . . . . .	27
2.4	Magnetospheric Emission From Neutron Stars . . . . .	27
<b>3</b>	<b>The Chandra X-ray Observatory</b>	<b>29</b>
3.1	Catching the X-rays . . . . .	29
3.2	Recording the X-rays . . . . .	30
3.2.1	Advanced CCD Imaging Spectrometer . . . . .	30
3.2.2	High Resolution Camera . . . . .	34
3.3	Dithering . . . . .	36
3.4	Grades . . . . .	37
3.5	Charge Transfer Inefficiency . . . . .	39
3.6	Hot Pixels . . . . .	39
3.7	Effective Area . . . . .	40
3.8	Point Spread Function & % Encircled Energy . . . . .	42
3.9	Pileup . . . . .	42
3.10	On-orbit Background . . . . .	45
3.11	Data Products . . . . .	45
<b>4</b>	<b>A History of the Supernova Remnant G21.5-0.9</b>	<b>46</b>
4.1	Radio and X-ray Discoveries . . . . .	46
4.2	Modern X-ray Observations . . . . .	51
4.3	PSR J1833-1034 Discovery . . . . .	54

4.4	Distance Estimate to G21.5-0.9 . . . . .	55
4.5	Motivation for Chandra Study of G21.5-0.9 . . . . .	55
<b>5</b>	<b>Chandra Observations and Data Preparation</b>	<b>57</b>
5.1	Observations . . . . .	57
5.2	ACIS Data Filtering . . . . .	61
5.2.1	Removing Bad Pixels . . . . .	61
5.2.2	Correction for Charge Transfer Inefficiency . . . . .	62
5.2.3	Gain . . . . .	63
5.2.4	Grades & Status . . . . .	63
5.2.5	Merging Multiple Observations . . . . .	64
5.3	HRC . . . . .	64
<b>6</b>	<b>A Chandra Study of G21.5-0.9: Imaging</b>	<b>65</b>
6.1	Combined Image . . . . .	65
6.2	Energy Image . . . . .	66
6.3	Morphology . . . . .	73
6.4	Radial Profile . . . . .	75
6.5	Search for Variability in G21.5-0.9 . . . . .	78
<b>7</b>	<b>A Chandra Study of G21.5-0.9: Spectroscopy</b>	<b>84</b>
7.1	Spectra Creation . . . . .	85
7.2	PSR J1833-1034 . . . . .	88
7.3	Plerion ( $r = 0'' - 40''$ ) . . . . .	90

7.4	X-ray Halo ( $r = 40'' - 150''$ ) . . . . .	92
7.5	Northern Knots . . . . .	93
7.6	Eastern Limb . . . . .	96
7.7	SS 397 . . . . .	96
7.8	Radial Variations . . . . .	97
<b>8</b>	<b>Summary, Conclusions &amp; Future</b>	<b>105</b>
<b>A</b>	<b>Scripts Used in Data Preparation</b>	<b>108</b>
A.1	Creating a cleaned event file for <i>Chandra</i> data using the CIAO CTI corrector . . . . .	108
A.2	Creating a cleaned event file for <i>Chandra</i> data using the Penn State CTI corrector . . . . .	110
A.3	Creating a spectrum from data corrected for CTI with the CIAO CTI corrector . . . . .	113
A.4	Creating a spectrum from data corrected for CTI with the Penn State CTI corrector . . . . .	116
<b>B</b>	<b>XSPEC Spectral Models</b>	<b>119</b>
B.1	const . . . . .	119
B.2	wabs . . . . .	119
B.3	power . . . . .	120
B.4	tbody . . . . .	120
B.5	pshock . . . . .	120

B.6 mekal . . . . .	121
B.7 gauss . . . . .	121
<b>C Data Tables for Radial Profiles</b>	<b>122</b>
<b>Glossary</b>	<b>124</b>
<b>Bibliography</b>	<b>126</b>

# LIST OF TABLES

1.1	Properties of Crab-like Supernova Remnants. . . . .	21
5.1	<i>Chandra</i> ACIS observations of the supernova remnant G21.5-0.9. . . . .	59
5.2	<i>Chandra</i> HRC-I observations of the supernova remnant G21.5-0.9. . . . .	61
7.1	Regions studied. . . . .	87
7.2	Spectral fitting results for the plerion of G21.5-0.9. . . . .	100
7.3	Spectral fitting results for the X-ray halo of G21.5-0.9. . . . .	101
C.1	Spectral fitting ( <i>const*wabs*power</i> ) results for radial profiles. . . . .	123
C.2	Spectral fitting ( <i>const*wabs*power</i> ) results for radial profiles when $N_{\text{H}} = 2.33 \times 10^{22}$ atoms $\text{cm}^{-2}$ . . . . .	123

# LIST OF FIGURES

1.1	Layers in an old massive star. . . . .	3
1.2	The location of ejecta and shocks in a supernova remnant. . . . .	10
1.3	The evolution of a supernova remnant. . . . .	11
1.4	The geometry of a neutron star. . . . .	14
1.5	The Crab Nebula in X-ray. . . . .	15
1.6	The Vela remnant in X-ray. . . . .	17
2.1	Bremsstrahlung spectrum with a temperature of $T = 2 \times 10^8$ K. . . . .	24
2.2	Synchrotron spectrum with a photon index of $\Gamma = 2.0$ . . . . .	26
2.3	Blackbody spectrum of a star with a temperature of $T = 2 \times 10^6$ K. . . . .	28
3.1	The <i>Chandra</i> X-ray Observatory. . . . .	30
3.2	The HRMA on <i>Chandra</i> . . . . .	31
3.3	The ACIS focal plane. . . . .	32
3.4	The HRC focal plane. . . . .	34
3.5	Schematic of the HRC Micro-channel-Plate detector. . . . .	35
3.6	A Lissajous figure. . . . .	37
3.7	Pixel patterns and their assigned ASCA grades. . . . .	38
3.8	ACIS energy resolution. . . . .	40
3.9	Effective area vs. X-ray energy. . . . .	41

3.10	Fractional encircled energy as a function of angular radius for an on-axis point source. . . . .	43
3.11	Encircled energy as a function of source off-axis angle for the combined HRMA/HRC-I. . . . .	44
6.1	ACIS combined image. . . . .	67
6.2	HRC-I combined image. . . . .	68
6.3	ACIS combined image of the plerion only. . . . .	69
6.4	HRC-I combined image of the plerion only. . . . .	70
6.5	ACIS energy band images. . . . .	71
6.6	ACIS colour image of G21.5-0.9. . . . .	72
6.7	G21.5-0.9 in Galactic coordinates. . . . .	74
6.8	Surface brightness of G21.5-0.9 as a function of radius. . . . .	76
6.9	Surface brightness of G21.5-0.9 as a function of radius in each quadrant. . . . .	77
6.10	Variability in remnants containing pulsars. . . . .	79
6.11	Variability in G21.5-0.9 as seen with the ACIS. . . . .	80
6.12	Variability in G21.5-0.9 as seen with the HRC-I. . . . .	81
6.13	Motion of knots in G21.5-0.9. . . . .	83
7.1	Regions used in spectral analysis. . . . .	88
7.2	Sample spectrum of the pulsar PSR J1833-1034. . . . .	89
7.3	Sample spectrum of the plerion ( $r = 0'' - 40''$ ). . . . .	91
7.4	Sample spectrum of the plerion ( $r = 4'' - 40''$ ). . . . .	91
7.5	Sample spectrum of the X-ray halo ( $r = 40'' - 150''$ ). . . . .	93

7.6	Sample spectrum of the northern knots. . . . .	94
7.7	Sample spectrum of the eastern limb. . . . .	97
7.8	Radial variations in the spectrum of G21.5-0.9 ( $N_{\text{H}}$ ). . . . .	98
7.9	Radial variations in the spectrum of G21.5-0.9 ( $\Gamma$ with $N_{\text{H}}$ free). . . . .	99
7.10	Radial variations in the spectrum of G21.5-0.9 ( $\Gamma$ with $N_{\text{H}}$ fixed). . . . .	99
8.1	Summary of G21.5-0.9. . . . .	107

# PREFACE

Supernova remnants powered by neutron stars appear with a filled-centre (plerionic) morphology and lack a surrounding shell. The lack of shells surrounding these remnants has been a mystery for decades. This thesis presents the results of a deep search for a shell surrounding one of these “plerionic” remnants, using NASA’s *Chandra* X-ray Observatory. The first evidence of a shell surrounding a plerionic remnant is presented. This thesis demonstrates the importance of deep searches for the missing shells.

Chapter 1 describes some general properties of supernova remnants, concentrating on the properties of remnants powered by rotation-powered neutron stars. Chapter 2 describes X-ray emission mechanisms that occur in supernova remnants. Chapter 3 discusses the *Chandra* X-ray Observatory. Chapter 4 summarizes the work that has been previously done on the supernova remnant G21.5-0.9. Chapter 5 describes the data and techniques used to prepare the data for analysis used in this thesis. Chapter 6 presents the imaging results of the *Chandra* study of G21.5-0.9. Chapter 7 presents the spectroscopic results of the *Chandra* study of G21.5-0.9. Chapter 8 is a summary and a look to the future.

Appendix A consists of four scripts used during data analysis. Appendix B describes the X-ray models used in the spectroscopic analysis. Appendix C is composed of data tables used to create the radial profiles in Section 7.8. A glossary with a list of abbreviations used throughout the thesis follows the appendices.

Preliminary work, including a spectroscopic analysis of the ACIS-I,  $-120^{\circ}\text{C}$  data, was published in Matheson & Safi-Harb, 2005 [32]. The colour energy image presented in Chapter 6 was the focus of a *Chandra* press release in April 2005 [37]. A publication involving the results presented here is in preparation.

# CHAPTER 1

## GENERAL PROPERTIES OF SUPERNOVA REMNANTS

Supernova explosions are extremely energetic stellar events, depositing  $\sim 10^{51}$  ergs of energy into their surroundings. Most of this energy appears as kinetic energy in the outer layers of the star, which are thrown into space with initial velocities of  $\sim 10,000 - 20,000 \text{ km s}^{-1}$ . An abundance of X-rays are emitted as the remnant expands and the ejected and surrounding material is heated to over a million degrees.

Since supernova remnants (SNRs) are the remains of massive stars (lower mass stars end their lives as white dwarfs), this chapter concentrates only on the properties of massive stars. Section 1.1 describes the life cycle of massive stars. Section 1.2 describes the types of supernova (SN) explosions. Section 1.3 describes the evolution of supernova remnants. Section 1.4 discusses remnants containing neutron stars, which are the focus of this thesis. Most of the information in this chapter is based on Charles & Seward, 1995 [17].

## 1.1 The Life Cycle of a Massive Star

The life of a star can be described in three phases: prior to the main sequence, during the main sequence, and after the main sequence.

The first phase begins with a molecular cloud collapsing to form a star and includes the life of the star during gravitational contraction and heating to the point when hydrogen burning begins, which is, by definition, the beginning of the main sequence.

A star spends most of its life on the main sequence (the second phase). On the main sequence there is an ongoing struggle by the force of gravity to cause the star to collapse. The star temporarily halts the collapse during its life by nuclear burning, which provides high internal temperature and pressure gradients that support the star [12, 15].

The third phase is a rapid evolution prior to the star's death that begins when hydrogen burning has been exhausted in the core of the star. In massive stars, collapse continues after a fuel supply is exhausted until the temperature in the core increases enough to ignite higher mass nuclei. A layer of material from the previous burning stage, which has not yet ignited, surrounds the core. Surrounding both of these regions is a shell where the previous burning stage continues, surrounded by unignited material. The pattern continues out to the hydrogen envelope (see Figure 1.1). The star's total mass determines the maximum temperature the star can attain, and therefore the highest nuclear burning stage [12].

Stars with  $M < 1.44M_{\odot}$  (Chandrasekhar limit) will become white dwarfs. Stars with  $1.44M_{\odot} < M \lesssim 4M_{\odot}$  will have to lose enough matter to have a final mass under

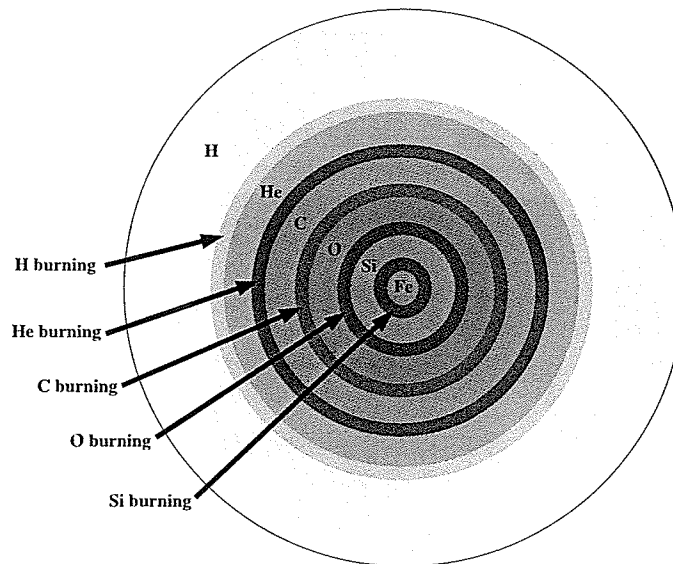


Figure 1.1 - Layers in an old massive star, showing the main constituents in each layer. Layers of different compositions are separated by active layers where fusion occurs.

the Chandrasekhar limit in order to become white dwarfs. Stars with a mass  $4M_{\odot} < M \lesssim 8M_{\odot}$  are possible supernova progenitors, although their fate is uncertain [12]. Stars with a mass over  $8M_{\odot}$  are massive enough to reach advanced nuclear burning stages and form presupernova cores.

A supernova explosion completely reorganizes the matter in a star. Some supernovae (SNe) completely disrupt the star and send enriched elements into the interstellar medium (ISM). Others eject only the outer envelope of the star and the core implodes to form a hot neutron star (if the compact remnant mass is under  $\sim 2.5M_{\odot}$ ) or black hole (if the compact remnant mass is  $> 2.5M_{\odot}$ ) [12]. The ejected mass will eventually merge with the ISM. However, an expanding nebula can exist for  $10^6$  or more years after the explosion.

Even though the material surrounding a SNR is referred to as interstellar, a lot

of it likely originated as the outermost layer (hydrogen) of the progenitor star. After a few million years the star's stellar wind would have surrounded the star with a low-density hydrogen bubble and the original ISM (and its inhomogeneities) would have been pushed away. The total mass loss by the star can be several  $M_{\odot}$  and the total energy loss in the wind can be comparable to the kinetic energy of the debris from the SN explosion.

## 1.2 Types of Supernovae

Supernovae (SNe) were historically divided into classes based on their optical spectra near maximum brightness [15]. Type II SNe display hydrogen emission lines, whereas Type I SNe do not. Type I SNe were further divided into subclasses based on the presence of other emission lines. Type I SNe displaying a Si II line are classified as Type Ia. Other Type I SNe are classified as Type Ib or Type Ic. Type Ib spectra show strong He lines, whereas Type Ic have weak He lines or none at all.

### 1.2.1 Type II Explosions

Type II events are observed in the arms of distant spiral galaxies known to contain bright young massive stars and dense clouds of gas and dust (indicating recent star formation). They rarely occur in elliptical galaxies with an older stellar population, suggesting the Type II progenitors are massive Population I stars.

Stars with an initial mass over  $8M_{\odot}$  burn nuclear fuel very rapidly. After  $\sim 10$  million years, the star is composed of onion-like layers (as shown in Figure 1.1). At

this point, the fuel is exhausted, and a Type II SN explosion ends the life of the star.

The core of the star has the density of a white dwarf ( $\sim 10^6 \text{ g cm}^{-3}$ ) and is surrounded by a shell of hydrogen. The iron core no longer generates energy (the binding energy per nucleus is a maximum for  $\text{Fe}^{56}$ , meaning that the creation of higher elements requires energy to be absorbed [12]), is stabilized by electron pressure, and is at the Chandrasekhar limit. However, the mass of the core continues to increase as the neighbouring layer of silicon is fused to iron. The core is further compressed and the temperature increases, causing some of the iron nuclei to decompose into lighter nuclei and absorb energy, lowering the pressure and causing the core to shrink. Free protons are created which react with electrons to form neutrons and neutrinos. The pressure in the core drops further when these electrons, which have been supporting the core, disappear. The process becomes runaway and gravity overwhelms the electron pressure. In seconds, the core collapses until nuclear density ( $\sim 10^{15} \text{ g cm}^{-3}$ ) is reached ( $1M_{\odot}$  within a 10 km radius). The neutrinos released in this process were detected on February 23, 1987 as the first signal from SN 1987A. A shock wave is created by energy that is explosively released by the infalling matter. This shock propagates outward through the infalling layers until it reaches the outermost regions of the star, which are ejected outward by the shock.

A rapidly cooling hot neutron star is left at the centre of the explosion, which may later be observable as a pulsar if it is spinning rapidly. The total energy generated by the explosion is over  $10^{53}$  ergs, with approximately 99% of this energy carried off by neutrinos which escape easily from the star and are difficult to detect due to their low reaction cross section (a measure of the probability of a reaction occurring). The

light from the SN carries away only  $10^{49}$  ergs, the kinetic energy of the expanding debris is  $\sim 10^{51}$  ergs, and the rotational energy of the neutron star is  $\sim 10^{49}$  ergs.

### 1.2.2 Type Ia Explosions

Type Ia events occur in all regions of all types of galaxies (no preference for spiral arms), suggesting the progenitors of Type Ia SN are billions of years old and not very massive (i.e. Population II stars). A lack of hydrogen lines in the spectra of Type Ia SNe suggests that the progenitors have lost their hydrogen envelopes.

Type Ia SNe all exhibit similar optical characteristics, and therefore similar progenitors are expected. The accepted constant starting points are white dwarfs at the Chandrasekhar limit. However, these stars are stable and mass must be added in order to produce an explosion. Therefore, white dwarfs in binary systems with mass transfer are the most likely Type Ia progenitors. Material is transferred from the companion star to the white dwarf until gravity overcomes the electron pressure. A collapse results and the temperature rises until oxygen and carbon begin to fuse in the core, creating an explosive wave that propagates through the core in a matter of seconds. Type Ia explosions completely disrupt the star and no compact remnant remains [49].

### 1.2.3 Type Ib/Ic Explosions

Types Ib and Ic SNe are observed only in spiral galaxies near HII regions (regions of star formation), indicating the progenitors are short-lived massive stars [15]. Since

Type I SNe lack H lines, these progenitors are believed to have lost their hydrogen envelope through stellar winds or mass transfer in a binary system [15]. These SNe are thought to occur by core-collapse, similar to Type II SNe.

### 1.3 Evolution of a Supernova Remnant

In addition to a possible compact remnant, a SN explosion creates a rapidly expanding shell of hot gas. Initially the shell contains the ejected stellar envelope (and possibly some mantle of the star), ejected at velocities of  $10^3 - 10^4 \text{ km s}^{-1}$ . The shell has a total mass of  $0.1 - 0.2M_{\odot}$  for Type I SNe and more than several  $M_{\odot}$  for Type II supernovae. The shell's expansion slows as interstellar matter is swept up by the expanding shell. These expanding shells can persist for up to  $10^6$  years and provide an estimate of the explosion date and the amount of energy released.

Assumptions usually made when describing expanding supernova shells are: (1) the supernova explodes and releases energy and a shock wave that travel into the ISM, (2) the energy release is instantaneous, (3) the shock wave is spherically symmetric (reasonable for non-rotating and non-magnetic stars, however, neutron stars do rotate and have strong magnetic fields), (4) the ISM is uniform and homogeneous in the region of the SN (this is likely not realistic, especially in disks of spiral galaxies) [13].

Most observed SNRs are approximately circular and are limb-brightened, as if looking at emission from a large hollow shell that is transparent to its own radiation. A circular shape is expected for the expanding debris of a SN since the simplest model is material ejected uniformly in all directions and a progenitor that was embedded

in a uniform medium. The shell of ejected matter rapidly expands, sweeping up the surrounding medium and leaving a low-density region in the interior. Soon the shell expands sufficiently to become of low enough density to be considered thin and transparent. In this first phase (*“free expansion phase”*) in the life of a supernova remnant, the mass of the swept-up material is negligible compared to the mass of the ejecta and the expansion occurs with uniform velocity. This phase will last until the swept-up mass equals the mass of the ejecta ( $\sim 300 - 1000$  years).

The speed of sound in the ISM is much less than the velocity of the stellar ejecta. As a result, a shock wave forms at the leading edge of the ejecta and travels slightly ahead of the ejecta into the surrounding material (which could be (1) material blown off of the progenitor by the stellar wind or (2) ISM). As the shock passes through material, a pressure increase is accompanied by a temperature increase to  $10^7 - 10^8$  K, and electrons separate from atoms (mainly hydrogen atoms if the shock is passing through ISM).

Over time the expansion slows and the remnant enters the second phase, adiabatic expansion (also known as the *“Sedov-Taylor phase”*). At this point, the mass of the swept-up material is large compared to the original mass of the ejecta. The energy radiated by the shell material remains small compared to its internal energy. The rate of expansion is determined by the initial energy deposited by the explosion and the density of the ISM. As the remnant expands the temperature decreases and it sweeps up interstellar material.

The stellar ejecta would freely expand at a velocity of  $10,000 - 20,000 \text{ km s}^{-1}$  if there were no surrounding material. However, interstellar gas forms a barrier that

becomes harder for the ejecta to expand into as the remnant size increases. As the fast-moving ejecta plough into the surrounding medium some of its kinetic energy is transferred to this interstellar gas, which is swept up and begins moving outward with the ejecta (known as the snowplough effect). Two shock waves are created, one propagating into the gas ahead of the ejecta (the “forward shock”), and one propagating back into the ejected gas (the “reverse shock”). To an outside observer, both shocks initially travel outward with the radii of the two shocks differing by  $\sim 25\%$ . As the swept-up mass increases, the reverse shock slows and once the accumulated mass becomes greater than the ejected mass, the reverse shock propagates back toward the centre of the remnant.

The material between the two shock waves is interstellar gas that has been heated and compressed by the expanding ejecta. The ejected material has been slowed and compressed by the pressure of the interstellar gas. At large distances, the interstellar gas is cool and unaffected by the expanding debris from the stellar explosion. In the central region the material is freely expanding, cool, and not yet affected by the resistance ahead. The shocked material is the only material hot enough to emit X-rays, forming the bright shells of young remnants. Features of supernova remnants which are visible in X-ray are shown in Figure 1.2.

The geometry of the remnants is complicated by irregularities in the ejecta and the surrounding medium. Supernova shock fronts are not exactly spherical and the ejected material pushing into interstellar gas is compressed, unstable, and expected to break into clumps.

An average remnant between 100 and 1000 years old accretes mass rapidly as it

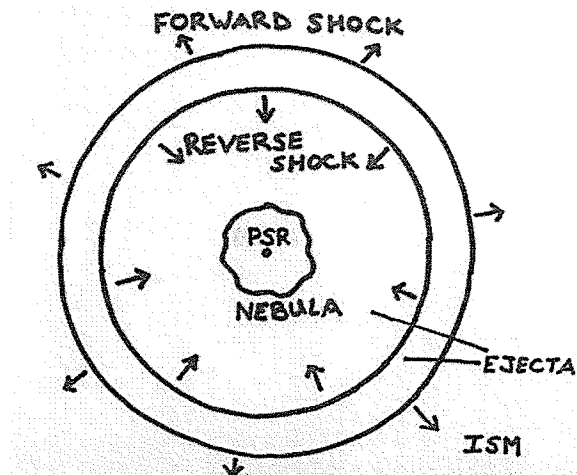


Figure 1.2 - The location of ejecta and shocks in a supernova remnant. Material outside the forward shock and inside the reverse shock is relatively cool. Material between the shocks and inside the pulsar wind nebula is hot and visible in X-ray.

expands, although the loss of energy through radiation is small. As the remnant size increases, this material is collected in a shell just behind the shock. The temperature of this material decreases with time. The behaviour of the remnant with time depends only on the initial energy released ( $E_0$ ) and the density of the surrounding medium ( $n$ ). If the distance to the remnant is known, the age ( $t$ ) and  $E_0$  can be found from the measured X-ray flux and spectrum (which gives the X-ray luminosity,  $L_X$ , and temperature,  $T$ ). The radius ( $R$ ) of the blast wave is

$$R = 14 \left( \frac{E_0}{n} \right)^{1/5} t^{2/5} \text{ pc}, \quad (1.1)$$

and the shock temperature ( $T$ ) is

$$T = 1.0 \times 10^{10} \left( \frac{E_0}{n} \right) R^{-3} \text{ K}, \quad (1.2)$$

where  $E_0$ ,  $n$ , and  $t$  have units of  $10^{51}$  ergs,  $\text{cm}^{-3}$ , and  $10^4$  years, respectively [17]. After a few hundred years of expansion most of the material in the remnant is swept-up

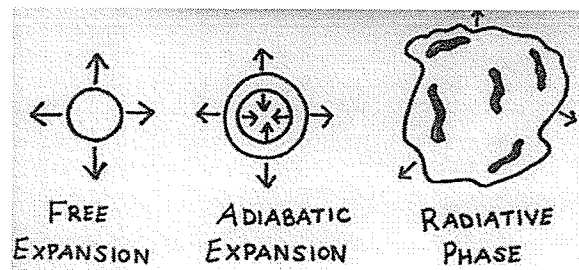


Figure 1.3 - The evolution of a supernova remnant. Not to scale. In the free expansion phase the mass of the swept-up material is negligible compared to the mass of the ejecta. In the adiabatic phase the mass of swept-up material is large compared to the mass of the ejecta and two shock waves are formed. The radiative phase is characterized by optical filaments.

ISM. The morphology and spectrum of the SNR are determined by the surrounding material rather than the explosion characteristics.

The rate of energy radiation increases as the material behind the shock cools due to the fact that after the temperature drops to  $\sim 2 \times 10^5$  K some electrons have recombined with carbon and oxygen ions and the gas radiates by ultraviolet line emission. The remnant is now in the third phase, the “*radiative phase*”. This phase lasts  $\sim 10^5$  years and during this time most of the internal energy is radiated away. During the radiative phase, the shell moves through interstellar space and becomes fainter and fainter until it can no longer be distinguished from the surrounding medium. Most remnants are detectable to the end of the radiative phase (30,000 - 100,000 years).

The X-ray morphology of SNRs can be similar to the radio structure in some cases, and different in other cases. The gas that is at high enough temperature to emit X-rays is too hot to have the bound electrons responsible for optical emission. A shell visible in both energy bands must therefore be composed of many interacting

regions of gas at different temperatures.

Old remnants usually appear as large radio shells containing optical filaments. The gas inside a large remnant is in pressure equilibrium, which is critical to filament formation. The force at the boundary of a high density cool gas cloud can be balanced by the force of a hot low-density cloud. A hot gas cloud cools slowly to the point where protons capture electrons and form hydrogen atoms. At this time, energy is radiated as UV lines and the rate of cooling increases due to the energy loss. This is the beginning of the radiative phase. The pressure decreases inside the cooling cloud and the cloud is compressed by the external pressure of surrounding hot material. The compression causes an increase in density, which increases the rate of radiation and causes the cloud to cool even more rapidly until a dense elongated cloud (the optical filament) remains. Any magnetic field that was present in the cloud has now been compressed and frozen into the ionized material. These filaments are also observed in the radio since radio emission is expected from regions of high magnetic field.

Since these old SNRs are so large (centred on our Sun they would surround thousands of stars), the diameter can be a sizeable fraction of the thickness of the Galactic disc. Therefore, older remnants will show large scale density fluctuations of the Milky Way in addition to the density structure of the local ISM.

## 1.4 Remnants Containing Neutron Stars

A neutron star (NS) has a mass of  $\sim 1.4M_{\odot}$  and a diameter of about 10 - 30 km. It is composed almost entirely of neutrons at the density of an atomic nucleus,  $10^{14}$  -

$10^{15} \text{ g cm}^{-3}$ .

Neutron stars have powerful dipole magnetic fields which are generally not aligned with the axes of rotation (Figure 1.4). These fields were created by the compression of fields of the progenitor stars when the stellar interior collapsed. As the neutron star rotates, electrons are torn from the surface and accelerated by magnetic fields. In these fields, the electrons move outward and are swept around by the rotation. Far from the surface of the star, the particles must stop co-rotating with the star since they cannot move faster than the speed of light. At this point the particles radiate some of their energy and a pulse of radiation is observed if a magnetic pole rotates through the observer's line of sight. Radio and higher frequencies are produced by the synchrotron process (see Section 2.2) as electrons move across magnetic field lines. The width of this radiation beam is uncertain. If it is narrow, most pulsars will be unobservable since the Earth is not illuminated by the rotating beam.

The discovery of pulsars confirmed the existence of neutron stars and their relation to supernova remnants. The signal observed from a pulsar is broadband noise with a maximum intensity occurring exactly periodically [12].

Observed pulsations of pulsars are extremely regular (the period can be measured very precisely), indicating that the pulsars are associated with a massive rapidly-rotating solid body. Rotation-powered pulsars slow down over time (pulsars in binary systems can spin-up, however, these pulsars are not studied in this thesis) and this loss of rotational energy powers a nebula surrounding the pulsar. Due to the energy being centrally injected by the pulsar, the nebula has a filled-in appearance. The term 'plerion' (from the Greek '*pleres*', meaning 'full') is used to describe these supernova

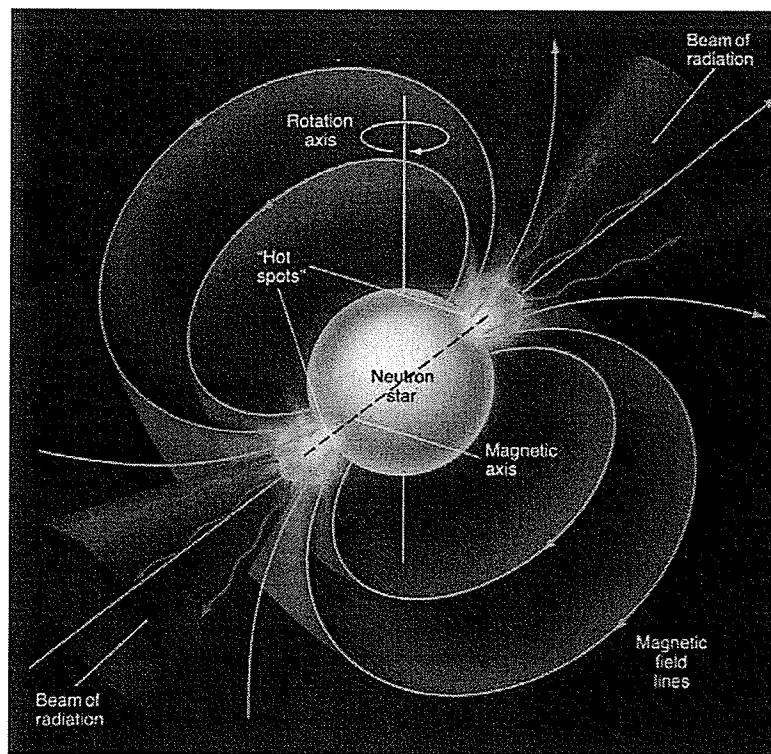


Figure 1.4 - The geometry of a neutron star. The magnetic and rotation axes are shown, along with the configuration of the magnetic field surrounding the neutron star. Available from: <http://www.tqny.com/NYCO40808/Homepage.html>

remnants.

The intense low frequency EM radiation of the pulsar has a braking effect which slows the rotation over time ( $\dot{P} \sim 10^{-15}$ ). A large fraction of the energy in the low-frequency radiation is quickly transferred to high energy electrons and the magnetic field. These electrons form a relativistic wind flowing outward from the pulsar. The energy density in this cloud of relativistic particles surrounding the pulsar is high. When the relativistic electrons cross magnetic field lines they radiate synchrotron radiation (radio through to gamma-rays), forming a bright diffuse nebula. This 'synchrotron nebula' dominates the appearance of plerions at X-ray wavelengths. Radiation from this nebula is separate from the pulsed emission originating close to

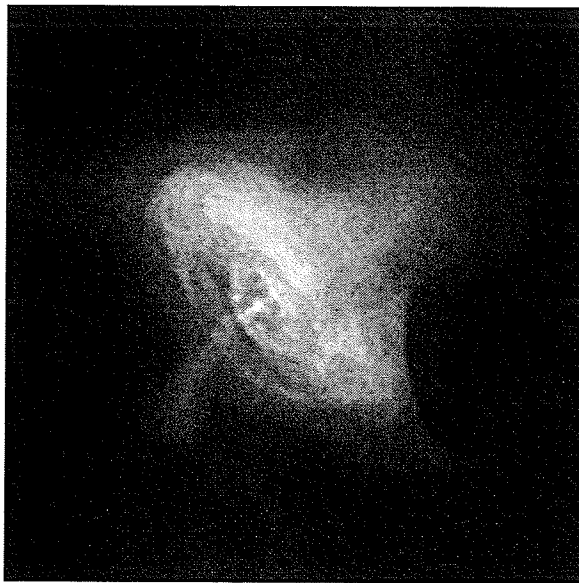


Figure 1.5 - The Crab Nebula in X-ray. The neutron star is visible at the centre of the remnant. *Credit: NASA/CXC/SAO. Available at: <http://chandra.harvard.edu/photo/1999/0052/index.html>*

the neutron star, which appears as a point source.

The Crab Nebula (Figure 1.5) is the most well-studied example of a SNR containing a neutron star (plerions are also referred to as ‘Crab-like’ SNRs). The Crab Nebula contains the first discovery of a NS formed in a supernova explosion. Observing the expansion of the remnant and propagating back in time gives an explosion in 1054, the date of the observed SN. The pulsar is located exactly in the centre of the remnant and the characteristic age of the pulsar is close to the age of the remnant. The energy lost by the pulsar is high enough to support the high luminosity of the Crab at all wavelengths.

In the case of the Crab Nebula, the brightest portion of the synchrotron nebula is centred  $10''$  northwest of the pulsar. One explanation [17] is that the bright region is a shock in the relativistic wind from the pulsar. Particles and magnetic field flow from

the pulsar at a velocity close to the speed of light. They are stopped by a network of filaments at the boundary of the nebula, indicating an abrupt transition in velocity at some point inside. The energy dissipation associated with such a shock would be a possible source of electron acceleration, which is necessary to maintain the nebula as we see it. The lifetime of electrons responsible for the diffuse X-ray nebula is only a few years, implying a constant internal source of energetic electrons (the neutron star) is needed in order for the plerion to remain visible for hundreds of years. The off-centre X-ray nebula implies that electron acceleration does not occur close to the pulsar and that the process is not symmetrical. One idea is that the pulsar is moving and compressing the magnetic field in the direction of motion.

The Vela Remnant (Figure 1.6) is another SNR containing a pulsar. It is much older than the Crab and is filled with optical filaments. Since it is only  $\sim 300$  pc away [36] there is little absorption of X-rays in the ISM. The interior of the remnant is filled with wisps of X-ray emitting plasma at two million degrees. The pulsar is approximately  $1^\circ$  from the apparent centre of the remnant. The pulsar is surrounded by a diffuse nebula only  $4''$  in diameter, with an X-ray luminosity of 0.0002 times that of the Crab. The Vela remnant has been shown by Pavlov et al. [36] to have a structure similar to the Crab. Jets have been observed and the PWN is observed to have a dynamic structure, with regions of compact emission showing displacement on a scale of weeks. In comparison, G21.5-0.9, the subject of this thesis, is at a distance of  $\sim 5000$  pc and the diameter of the nebula is  $\sim 80''$ .

After considering beaming effects, fewer pulsars than expected have been detected in SNRs which are thought to have originated in gravitational collapse. One explana-



Figure 1.6 - The Vela remnant in X-ray. *Credit: NASA/PSU/G. Pavlov et al. Available at: <http://chandra.harvard.edu/photo/2000/vela/>*

tion is that in some cases pulsar emission is easier to see above background in X-ray than radio.

### 1.4.1 Characteristics of Pulsars

There are two types of pulsars, rotation-powered pulsars and accretion-powered pulsars. Since this study involves a rotation-powered pulsar, this section concentrates on properties of these pulsars.

A rotating neutron star with a magnetic field must radiate (EM) energy at the rotation frequency. There is a torque associated with this radiation that slows the rotation. Over time rotational energy is converted to radiation and the star slows down.

Periods of pulsars vary from 1.6 ms to several seconds. Typical period derivatives are  $\dot{P} \sim 10^{-15}$  [43]. Period irregularities, known as 'glitches', exist in pulsars. A

glitch is a sudden decrease in period, accompanied by an increase in period derivative ( $\Delta\dot{P}/\dot{P} \sim 0.01$ ) which decays away in a few days [43].

If the field is a dipole field the torque is at a maximum. By observing the rotational period ( $P$ ) and the spin-down rate ( $\dot{P}$ ), several quantities can be found. The rotational moment of inertia ( $I$ ), assuming a rigid rotating sphere, is

$$I = \frac{2MR^2}{5} = 10^{45} \text{ g cm}^2 \quad (1.3)$$

for a  $1M_{\odot}$  neutron star with a radius

$$R = 10 \text{ km}. \quad (1.4)$$

The rotational energy of the pulsar is

$$E = \frac{2\pi^2 I}{P^2} \text{ erg} \quad (1.5)$$

and the rate of rotational energy loss (negative since the pulsar is losing energy) is

$$\dot{E} = -\frac{4\pi^2 I \dot{P}}{P^3} \text{ erg s}^{-1}. \quad (1.6)$$

If the rotation frequency of the neutron star is denoted by  $\Omega = 2\pi/P$ , the rotational energy can be written as

$$E = \frac{I\Omega^2}{2} \quad (1.7)$$

and the rate of energy loss can be written as

$$\dot{E} = I\Omega\dot{\Omega}. \quad (1.8)$$

Assuming a power-law deceleration model,

$$\dot{\Omega} = -k\Omega^n, \quad (1.9)$$

where  $k$  is a constant and  $n$  is the braking index (for a magnetic dipole model,  $n = 3$ ).

In general the braking index can be found from

$$n \equiv -\frac{\Omega\ddot{\Omega}}{\dot{\Omega}^2}. \quad (1.10)$$

If the period of the pulsar is larger than the period at birth, the age of the pulsar should be close to the characteristic age,

$$\tau = \frac{P}{(n-1)\dot{P}} = \frac{P}{2\dot{P}}. \quad (1.11)$$

The field at the magnetic pole (field is strongest at pole) is

$$B = \left( \frac{3c^3 I P \dot{P}}{8\pi^2 R^6 \sin^2 \alpha} \right)^{1/2} \text{ Gauss} \simeq 3.2 \times 10^{19} (P \dot{P})^{1/2} \text{ G}, \quad (1.12)$$

where  $\alpha$  is the angle between the rotation axis and the magnetic axis (numerical estimate assumed  $I = 10^{45} \text{ g cm}^2$ ,  $R = 10 \text{ km}$ , and  $\sin^2 \alpha = 1$ ).

Even if radiation from the pulsar itself is beamed and not directed towards us, emission from the surrounding nebula will be observed for an active rotation-powered pulsar. Therefore, the presence of a pulsar can be detected. Similarly, the absence of an energetic pulsar is normally detectable by the lack of a synchrotron nebula.

### 1.4.2 Characteristics of Pulsar Wind Nebulae

The pressure in a PWN is

$$P_n = \frac{B_n^2}{8\pi}, \quad (1.13)$$

where  $B_n$  is the equipartition magnetic field strength (the magnetic field when the energy in the relativistic particles equals the energy in the magnetic field). [14, 38]

Young pulsars in high-pressure SNR interiors often move at speeds slow enough to create termination shocks surrounding the central pulsars where the pulsar wind meets the slowly expanding nebula. The characteristic scale of the wind termination shock around a pulsar is determined by a balance of ram pressure and pressure in the nebula, and is given by

$$r_t \approx \left( \frac{\dot{E}}{4\pi c P_n} \right)^{1/2}, \quad (1.14)$$

where  $\dot{E}$  is the spin-down power,  $P_n$  is the pressure in the nebula, and  $c$  is the speed of light [34]. This structure is expected to be azimuthally symmetric about the pulsar spin axis if

$$P_n \geq P_{ram} = 6 \times 10^{-24} n v^2 \text{ g cm}^{-1} \text{ s}^{-2}, \quad (1.15)$$

where the pulsar is moving at subsonic speed  $v$  (e.g. the Crab nebula), and  $n$  is the density of the medium [34]. In the case where the pulsar is moving at high speed, a “bow shock” nebula is formed (e.g. CTB 80).

The spectra of PWNe are dominated by non-thermal synchrotron radiation (Section 2.2) which can be described with a power-law,

$$S_\nu \sim \nu^{-\alpha}, \quad (1.16)$$

where  $\alpha$  is the “spectral index” in the radio.

G21.5-0.9, the subject of this thesis, is one of approximately 11 Crab-like remnants. A list of known Crab-like remnants and their properties is given in Table 1.1.

Table 1.1. Properties of Crab-like Supernova Remnants.<sup>a</sup>

name (Galactic coordinates)	distance (kpc)	radio size (arcmin)	radio flux (1 GHz flux in Jy)	spectral index (radio)	spectral break	X-ray size (arcmin)	X-ray flux ( $10^{-12}$ erg cm <sup>-2</sup> s <sup>-1</sup> )	photon index (X-ray)	pulsar period (ms)
6.1+1.2 <sup>b,c</sup>		30×26	4.0	0.3					
20.0-0.2 <sup>b,c</sup>	5.4	10	10	0.0					
21.5-0.9	4.6	1.5	6	-0.01	~100 GHz	5	58 (0.5-8 keV)	1.8	61.86
27.8+0.6 <sup>b</sup>	2.1	50×30	30	0.3 (<5 GHz), 1.0 (>5 GHz)	~5 GHz				
54.1+0.3	5	2.0×1.2	0.5	0.1	7×10 <sup>25</sup> Hz	1.5×1.2	6.8 (0.7-10 keV)	1.9	136.8
63.7+1.1 <sup>b,c</sup>	3.8	8	1.8	0.28					
65.7+1.2 <sup>c</sup> (DA 495)	1.5	20	5.1	0.6		10	1.3 (0.7-10 keV)	1.7	
74.9+1.2 <sup>c</sup> (CTB 87)	6.1	9×6	8.7	0.24	~20 GHz	5	0.83 (0.15-3 keV)	2.48	
130.7+3.1 (3C 58, SN1181)	3.2	10×6	33	0.10	~50 GHz	7×5	13 (0.5 - 10 keV)	1.9	65.68
184.6-5.8 (Crab, SN1054)	1.9	7×5	1040	0.30	~10 <sup>13</sup> Hz	2.5	22830 (2-10 keV)	2.1	33.51
328.4+0.2 <sup>c</sup>	17.4	5	14.8	0.12	~3×10 <sup>14</sup> Hz	unresolved	0.60 (2-10 keV)	2.9	

<sup>a</sup>Compiled from Green's Supernova Remnant Catalogue [22] and references therein.

<sup>b</sup>X-ray studies on these remnants have not yet been published.

<sup>c</sup>Pulsars have not yet been observed in these remnants.

# CHAPTER 2

## AN X-RAY VIEW OF SUPERNOVA

### REMNANTS

Two main physical processes are expected to produce X-rays in supernova remnants. Thermal emission is discussed in Section 2.1 and non-thermal emission is discussed in Section 2.2. In addition, blackbody (thermal) radiation occurs in the X-ray emission from hot stars (Section 2.3), and magnetospheric (non-thermal) emission originates near neutron stars (Section 2.4). Unless otherwise mentioned, the information in this chapter is based on the text of Charles & Seward, 1995 [17].

#### 2.1 Thermal Emission From a Hot Gas

At X-ray frequencies it is easy to achieve a hot gas of low enough density to be described as “thin” and transparent to its own radiation. Above  $10^5$  K, atoms are ionized and a gas consists of positive ions and negative electrons. Thermal energy is shared among these particles through collisions which rapidly transfer energy from one particle to another. Thermal equilibrium occurs when all of the particles in the gas have the same average energy (temperature). Strong forces cause the trajectory of an electron to be altered when the electron passes close to a positive ion. This

acceleration of the electron causes it to radiate energy, known as bremsstrahlung (meaning “braking radiation”) radiation.

Electrons in thermal equilibrium have a well defined Maxwellian distribution of velocities. The radiation from electron-ion collisions is a continuum with a characteristic shape dependent only on temperature. This radiation is “thermal bremsstrahlung”. Higher temperatures result in faster motion of electrons and therefore radiation of higher energy photons. Temperatures over one million degrees produce mainly X-rays.

The thermal bremsstrahlung spectrum (Figure 2.1) is characterized by the temperature ( $T$ ) and falls off exponentially at high energies. The intensity ( $I$ ) of the radiation at energy  $E$  is

$$I(E, T) = AG(E, T)Z^2n_en_i(kT)^{-1/2}e^{-E/kT}, \quad (2.1)$$

where  $A$  is a constant,  $Z$  is the charge of the positive ions,  $n_e$  is the electron density,  $n_i$  is the positive ion density,  $k$  is Boltzmann’s constant and  $G$  is the Gaunt factor, a slowly varying function that increases as  $E$  decreases.

X-ray line emission is also an important source of radiation in a hot gas. Elements heavier than hydrogen are not completely ionized unless they are at very high temperatures. When a fast electron collides with an ion it can transfer energy to that ion and cause an electron to transition to a higher energy level, leaving the ion in a brief excited state. The ion decays rapidly to its ground state by radiating photons with energy characteristic to the spacing of the energy levels through which the excited electron passes. This radiation will appear as spectral lines with energies dependent

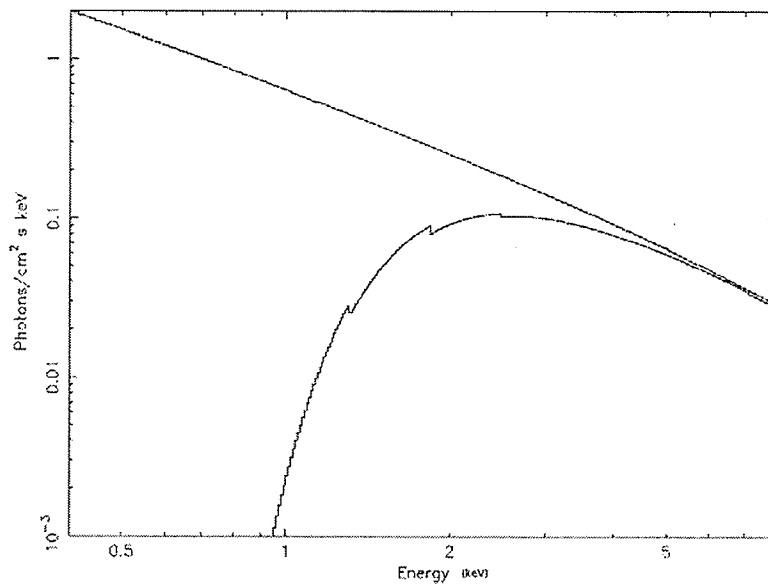


Figure 2.1 - Bremsstrahlung spectrum with a temperature of  $T = 2 \times 10^8$  K. Top curve is unabsorbed model, bottom curve is absorbed with  $N_{\text{H}} = 2.33 \times 10^{22}$  atoms  $\text{cm}^{-2}$ .

on the type of ion present.

Thermal radiation from a gas is therefore a blend of thermal bremsstrahlung and line radiation (*XSPEC mekal* model, Appendix B.6). Assuming a gas of cosmic composition (for every 10000 atoms of H, there are 800 atoms of He and 16 atoms of heavier elements) we expect: (1) below  $1 \times 10^6$  K most of the energy is radiated as UV lines, (2) at  $2 \times 10^6$  K half of the energy is radiated as soft X-rays, (3) at  $1 \times 10^7$  K all the energy is radiated as X-rays, half as thermal bremsstrahlung and half as lines, and (4) at  $5 \times 10^7$  K almost all of the ions have been stripped of their bound electrons and nearly all the energy is radiated in the X-ray continuum.

By measuring the X-ray spectrum, the temperature of the gas can be determined from the lines present and the shape of the high energy end of the bremsstrahlung continuum. The composition of the gas is also revealed by the energies of the lines. Once the temperature and composition are known, we can use the observed X-ray

luminosity to derive the mass of material.

## 2.2 Synchrotron Radiation From Relativistic Electrons

A high energy electron passing through a region containing a magnetic field will change direction as a result of the force exerted by the field perpendicular to the direction of motion. The electron is accelerated and therefore emits EM radiation, known as “synchrotron radiation”. The frequency of the radiation depends on the electron energy, the strength of the magnetic field, and the direction of motion relative to the field.

In astrophysical settings, magnetic fields tend to be aligned and particle velocities are expected to be uniform. Therefore, the observed spectrum depends only on the magnetic field strength,  $B$ , and the energy spectrum of the electrons. A power-law distribution is usually assumed for the electrons, meaning that the spectrum of the resulting synchrotron radiation will also be a power-law. When an observed spectrum is a power-law over a large energy range, it therefore indicates the source is emitting synchrotron radiation. If the magnetic field is aligned, the radiation will be polarized. Polarization is therefore proof of synchrotron emission.

The power-law has the form

$$I(E) = AE^{-\alpha}, \quad (2.2)$$

where  $A$  is a constant and  $\alpha$  is the spectral index in the radio. A larger value for  $\alpha$

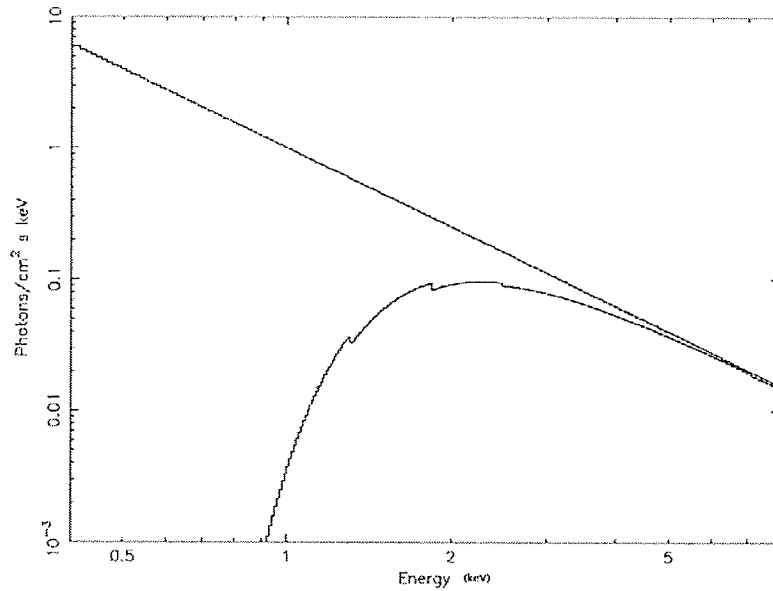


Figure 2.2 - Synchrotron spectrum with a photon index of  $\Gamma = 2.0$ . Top curve is unabsorbed model, bottom curve is absorbed with  $N_{\text{H}} = 2.33 \times 10^{22}$  atoms  $\text{cm}^{-2}$ .

indicates a softer (steeper) spectrum.

We can also write the power-law in the form

$$\frac{dN}{dE} \sim E^{-\gamma}, \quad (2.3)$$

where  $\gamma$  and  $\alpha$  are related as

$$\alpha = \frac{\gamma - 1}{2}. \quad (2.4)$$

A synchrotron spectrum in X-ray is shown in Figure 2.2.

Pulsar wind nebulae are observed to have a “spectral break” between radio and X-ray frequencies. A typical spectral index at radio frequencies is  $\alpha = 0.5$ , while at X-ray frequencies the power-law steepens to  $\alpha = 1.0$  (due to synchrotron cooling). When discussing a power-law distribution in X-ray, the photon index,  $\Gamma = \alpha + 1$  is usually reported. Therefore a typical photon index for PWNe is  $\Gamma = 2$ .

The power radiated as synchrotron radiation is  $\propto B^2 E^2$  and the average photon

energy is  $\propto BE^2$ . Radiation is emitted over most of the EM spectrum. The electrons which produce synchrotron X-rays have energies of  $\sim 10^4$  GeV, or a few erg, each. Synchrotron X-rays therefore indicate the presence of very energetic (TeV) electrons.

## 2.3 Blackbody Radiation From Star-like Objects

A “black” surface is defined as one that completely absorbs all incident radiation. The spectrum radiated is a well-defined continuum with the energy of the peak emission dependent only on the temperature,  $T$ . A higher temperature produces more energetic photons. The spectrum has the form

$$I(E, T) = 2E^3 [h^2 c^2 (e^{E/kT} - 1)]^{-1}, \quad (2.5)$$

where  $h$  is Planck’s constant,  $c$  is the speed of light, and  $k$  is Boltzmann’s constant.

Stars radiate as blackbodies with temperatures from 2500 K (red dwarf) to 40000 K (O star). Spectra are strongly modified by the stellar atmosphere but retain the overall shape from the blackbody emission process. A young neutron star is expected to have a hot surface and if the surface temperature is one million degrees or higher it will emit blackbody radiation with photons in the X-ray range.

## 2.4 Magnetospheric Emission From Neutron Stars

Non-thermal emission also occurs from neutron stars. A neutron star can be thought of as a rapidly rotating, highly magnetized, superconducting sphere. The region surrounding the neutron star, filled with plasma and dominated by the magnetic field,

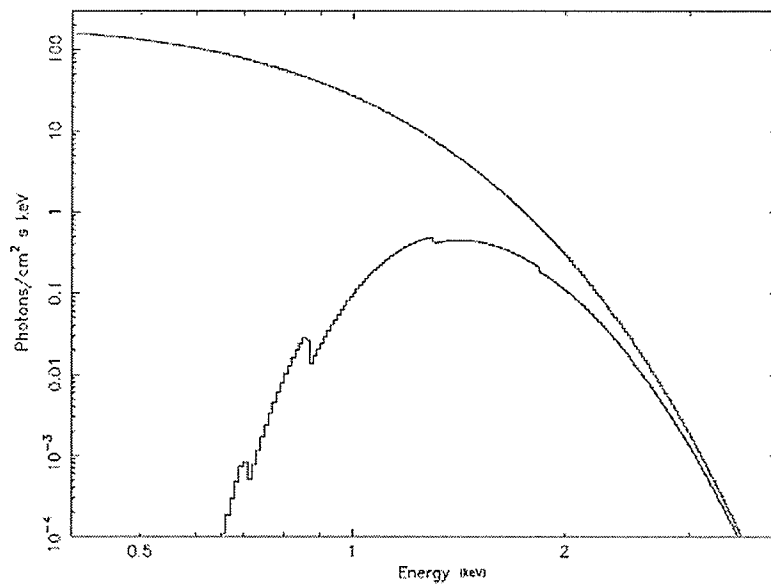


Figure 2.3 - Blackbody spectrum of a star with a temperature of  $T = 2 \times 10^6$  K. Top curve is unabsorbed model, bottom curve is absorbed with  $N_{\text{H}} = 2.33 \times 10^{22}$  atoms  $\text{cm}^{-2}$ .

is the pulsar magnetosphere [31]. Neutron stars with short periods and strong magnetic fields (for example, the Crab Pulsar) develop strong electric potentials within the magnetosphere. Relativistic particles in the electromagnetic field are continually accelerated to high energies, emitting radiation [30]. These particles are expected to have a spectrum characterized by a power-law distribution [7].

One example of magnetospheric emission from a neutron star is from PSR B0531+21, the neutron star powering the Crab Nebula. It has a power-law spectrum characterized by a photon index of  $1.72 \pm 0.05$  [28].

# CHAPTER 3

## THE CHANDRA X-RAY OBSERVATORY

The *Chandra* X-ray Observatory (*CXO*) was launched on July 23, 1999 from the Space Shuttle Columbia, and combines a high resolution ( $\leq 0.5''$ ) X-ray telescope with advanced imaging and spectroscopic ( $\leq 0.1$  to 10 keV) instruments. Figure 3.1 shows the main components of *Chandra*, whose operation will be described in the following chapter. Most of the material presented in this chapter was obtained from the *Chandra* Proposers' Observatory Guide [16], which describes the operation of *Chandra* in much more detail than the overview presented here.

This thesis made use of data obtained with two instruments aboard *Chandra*, the Advanced CCD Imaging Spectrometer (ACIS) and the High Resolution Camera (HRC).

### 3.1 Catching the X-rays

The orbit of the *CXO* is elliptical (as of Dec. 2005 the apogee height was 120,300 km and the perigee height was 28,600 km) with an orbital period of 63.5 hours.

The High Resolution Mirror Assembly (HRMA, Figure 3.2) is composed of a nested set of four concentric paraboloid-hyperboloid grazing-incidence X-ray mirror pairs (the largest having a diameter of 1.2 m) with a focal length of 10 m.

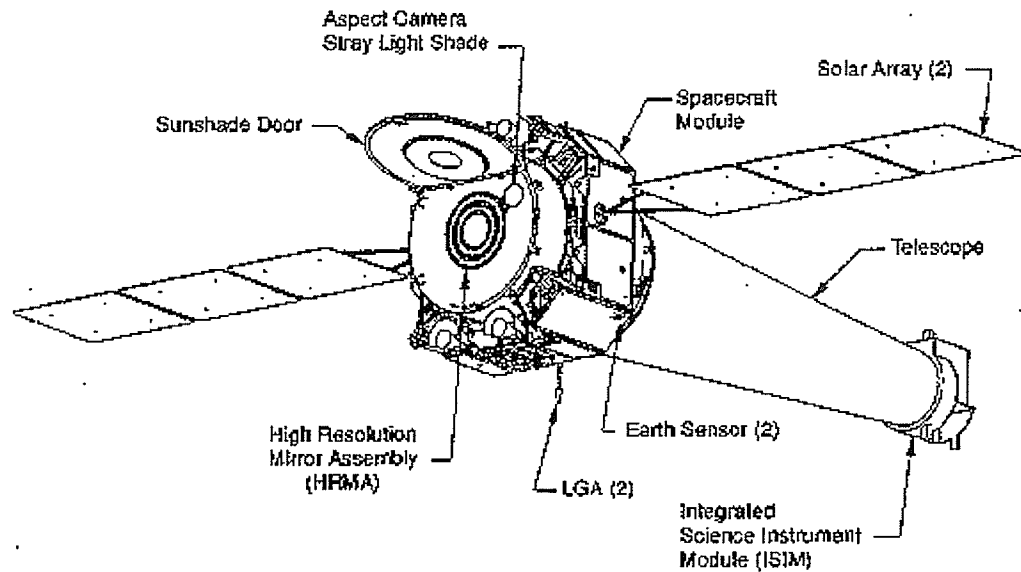


Figure 3.1 - The *Chandra* X-ray Observatory. Credit: CXC/NASA. Available at <http://cxc.harvard.edu/proposer/ogplots/sc-config.eps>

The HRMA focuses the incident X-rays onto the focal plane. The following section describes two methods used to record the X-rays, with Charge Coupled Devices (CCDs) for the ACIS, and with Microchannel Plates (MCPs) for the HRC.

## 3.2 Recording the X-rays

### 3.2.1 Advanced CCD Imaging Spectrometer

The ACIS is composed of ten  $1024 \times 1024$  pixel CCDs, arranged in two arrays ( $2 \times 2$  ACIS-I and  $1 \times 6$  ACIS-S, as shown in Figure 3.3). Each CCD is flat and the chips are tilted to approximate the focal surface.

The ACIS pixel size is  $0.4920'' \pm 0.0001''$ , resulting in an array size of  $16.9' \times 16.9'$  for ACIS-I and  $8.3' \times 50.6'$  for ACIS-S. Two CCDs are back-illuminated (BI) and eight

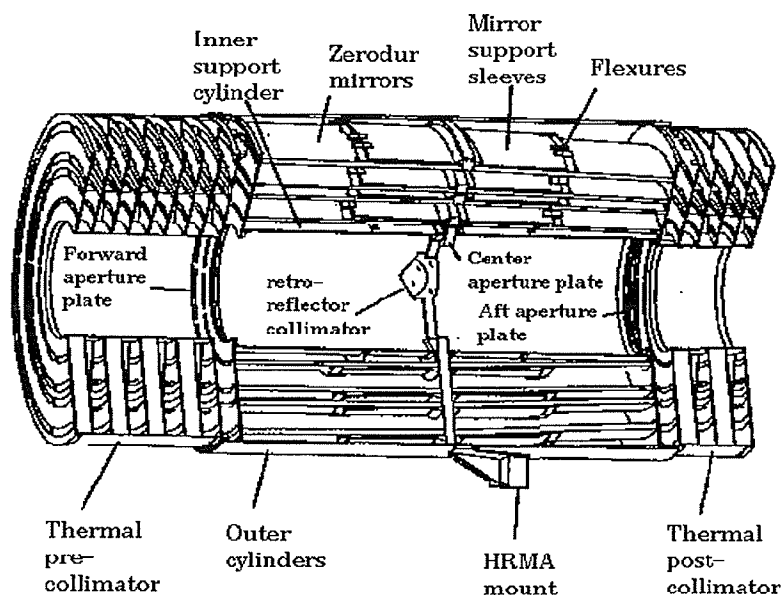


Figure 3.2 - The HRMA on *Chandra*. Credit: CXC/NASA. Available at <http://cxc.harvard.edu/proposer/ogplots/hrma-config.eps>

CCDs are front-illuminated (FI). The BI devices (S1 and S3) have a response that extends to lower energies than the FI devices. As well, the BI devices have a better energy resolution when averaged over the chip.

The CCDs are sensitive to optical photons, as well as X-ray photons. Incident radiation therefore passes through optical blocking filters (OBFs), positioned slightly above the CCDs, after passing through the HRMA.

A CCD is a solid-state electronic device made of silicon. Pixel boundaries are defined on the surface by alternating voltages on three electrodes spanning the pixel. The silicon in the active region has an applied electric field that moves charge quickly to the gate surface. The gates allow confined charge to be passed down a buried channel of pixels in parallel to a serial readout at one edge by varying the voltages in the gates.

## ACIS FLIGHT FOCAL PLANE

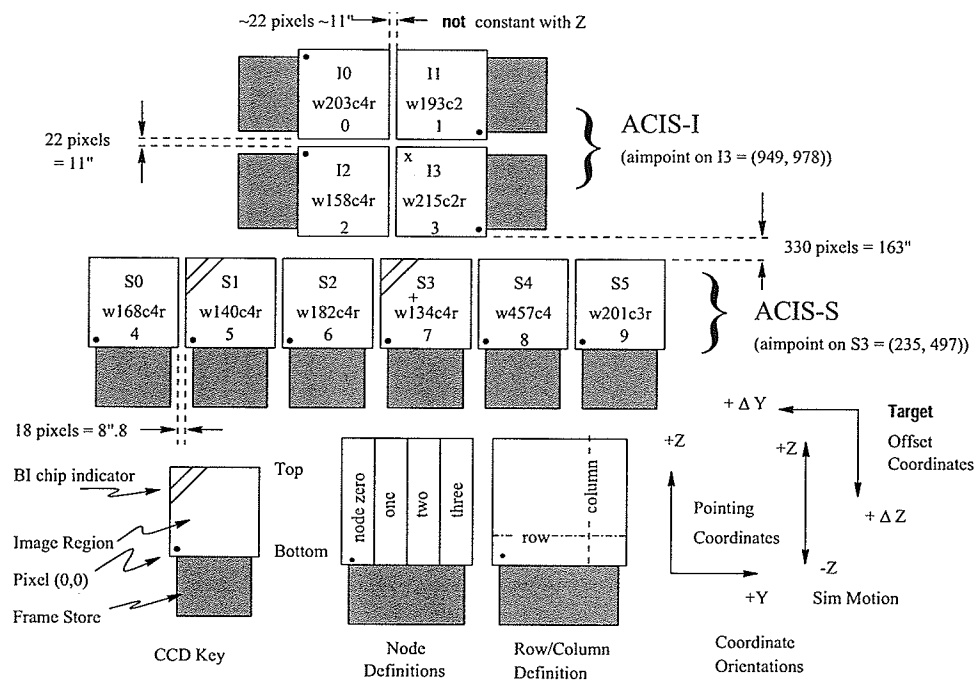


Figure 3.3 - The ACIS focal plane. Credit: CXC/NASA. Available at [http://cxc.harvard.edu/proposer/ogplots/acis\\_flight\\_focal\\_plane.eps](http://cxc.harvard.edu/proposer/ogplots/acis_flight_focal_plane.eps)

The FI CCDs have the gate structures facing the incoming X-ray beam. Chips S1 and S3 had treatments applied to the back of the chips, exposing the photo-sensitive region. These BI chips have the back side facing the incoming X-rays.

The photoelectric absorption of an X-ray in the silicon creates an average of one electron-hole pair for each 3.7 eV absorbed from the photon. After the photoelectric interaction, the charge is confined by electric fields to a small volume near the interaction site. The charge may be spread over two or more pixels.

Good spectral resolution depends on accurately determining the total charge deposited by a photon, which depends on the fraction of charge collected, the fraction of charge lost in transfer from pixel to pixel during read-out, and the ability of the

readout amplifiers to measure the charge.

As shown in Figure 3.3 (lower left), the CCDs have an active (imaging) section that is exposed to the incident radiation and a shielded frame store region. The observations used in this study were all obtained in Timed Exposure mode, which is a typical mode of operation. Timed Exposure mode is described as follows: (1) the active region is exposed for a fixed amount of time ( $\sim 3.2$  s for a full frame); (2) at the end of the exposure the charge in the active region is quickly ( $\sim 41$  ms) transferred into the frame store; (3) the next exposure begins; (4) at the same time, the data in the frame store region is passed to a local processor which identifies the position and amplitude of any events. The position, amount of charge, and similar data for a limited region containing and surrounding the pixel are graded (see Section 3.4) and then passed into the telemetry stream.

Since it takes  $41 \mu\text{sec}$  during readout to transfer one row to another, the process of moving the active region to the framestore region causes each CCD pixel to be exposed to every region of the sky along the column in which the pixel resides for  $41 \mu\text{sec}$ . If there are bright features present in the image, a “trailed” image will therefore appear in the data.

One common requirement to identify the position and amplitude of events is a local maximum in the charge distribution above the event threshold. CCD bias maps are applied during processing to remove the amplitude of the charge that is present in each pixel in the absence of radiation (“bias”). The charge recorded from a pixel must therefore be above the bias value in order for an event to be retained.

The spatial resolution of on-axis imaging with ACIS is limited by the physical size



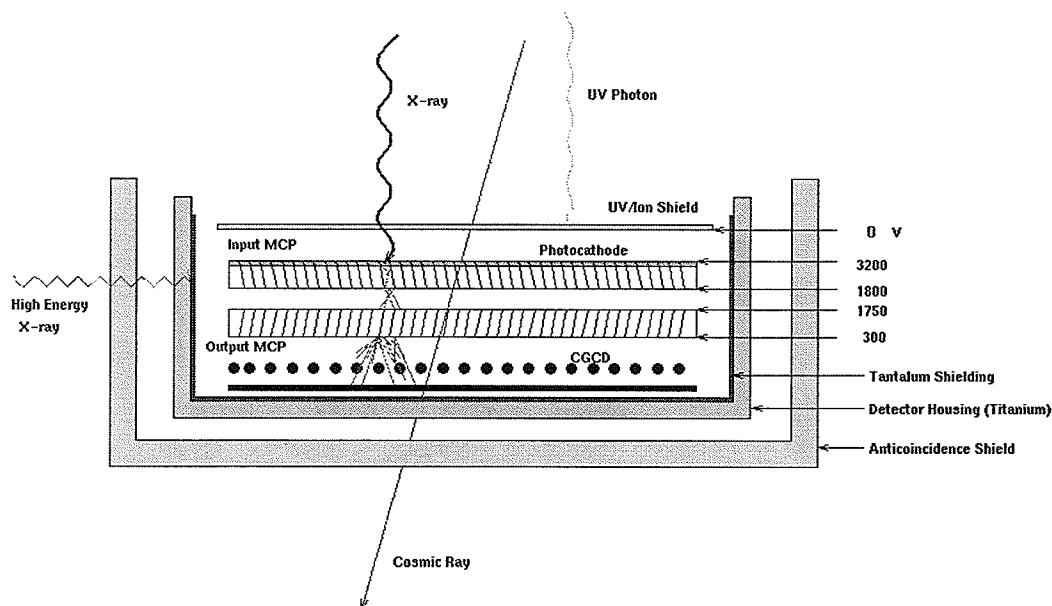


Figure 3.5 - Schematic of the HRC Micro-channel-Plate detector. *Credit: CXC/NASA. Available at <http://cxc.harvard.edu/proposer/ogplots/snap.ps>*

X-rays enter the HRC MCPs (Figure 3.5) through an UV/Ion shield, which reduces signals from UV light, ions, and low energy electrons. Most X-rays entering the input MCP are absorbed in the CsI-coated walls. The MCPs are composed of millions of tubes that are tilted at an angle of  $6^\circ$  from the optical axis, improving the interaction probability. The CsI coating enhances the photoemission compared to a bare MCP. The resulting photoelectrons are accelerated by an applied electric field. The next interaction with the walls releases several secondary electrons, which each produce more electrons, resulting in a cascade of electrons.

The output MCP provides additional gain and is tilted at the reverse angle with respect to the input MCP, thereby removing a clear path for positive ions. This reduces the chance of positive ion feedback that occurs when an accelerated ion moving

in the opposite direction to the electrons causes the release of electrons and starts the process again.

The electron cloud ( $\sim 2 \times 10^7$  electrons per photon) emerging from the output MCP is accelerated towards a position-sensitive charge detector. The X-ray position is determined by calculating the centroid of the charge cloud exiting the output MCP. A coarse position is determined from the amplifier with the maximum detected charge. The three amplifiers centred on the coarse position are then telemetered to the ground and used off-line to calculate the event position.

The HRC-I has a lower background than HRC-S and a larger field of view, producing the best imaging. The HRC pixel size is determined by the electronic readout and is  $0.13175''$ . However, the intrinsic PSF of the HRC is well modelled by a Gaussian distribution with a FWHM of  $\sim 0.4''$  and limits the resolution of the HRC (see Section 3.8).

The intrinsic energy resolution of the HRC is poor and even though the pulse-height amplitude (PHA) of each event is telemetered, spectral fitting cannot be usefully carried out for sources observed with the HRC.

### 3.3 Dithering

Most *Chandra* observations are performed with dither selected. Dithering (moving the *Chandra* line of sight through a Lissajous pattern) distributes photons over many CCD pixels and is used to spread an instantaneous image over many pixels on the detector, provide some exposure in the gaps between CCDs, and smooth out pixel to

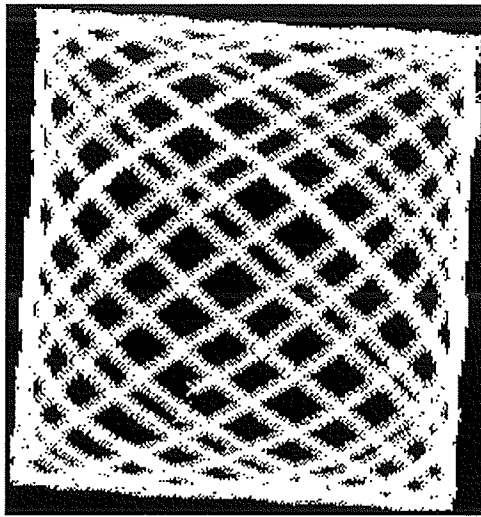


Figure 3.6 - A Lissajous figure. *Credit: CXC/NASA. Adapted from: [http://cxc.harvard.edu/ciao/why/imgs/dither\\_1.gif](http://cxc.harvard.edu/ciao/why/imgs/dither_1.gif)*

pixel variations in the response.

The spacecraft is usually dithered with a Lissajous figure (see Figure 3.6) that spans 16" from peak-to-peak in the pattern for the ACIS observations, and 40" peak-to-peak for the HRC observations. The dither is removed during ground processing. The exposure time in the gaps between the CCDs will be less than for the rest of the field due to dithering. In this thesis, spectra were created from only one CCD per observation so this difference in exposure time was not a concern.

### 3.4 Grades

To detect X-ray events from ACIS, each pixel is examined and only pixels with bias-subtracted values above the event threshold and above all adjacent pixels are retained. The surrounding pixels that are above the bias-subtracted split event threshold form the pixel pattern. This pattern determines the assigned grade, as shown in Figure 3.7.

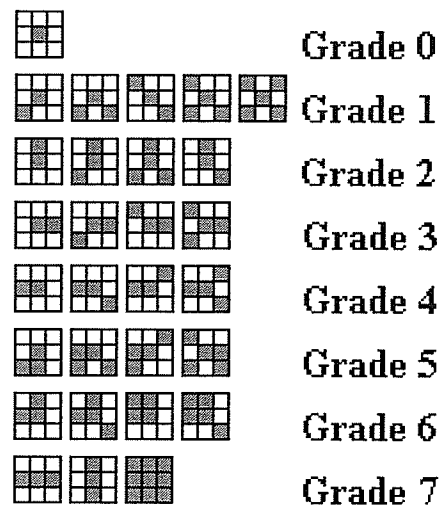


Figure 3.7 - Pixel patterns and their assigned ASCA grades. 0 - Single Pixel Events, 1 - Diagonal Split, 2 - Vertical Split, 3 - Horizontal Split Left, 4 - Horizontal Split Right, 5 - "L"-Shaped Split with Corners, 6 - "L" & Quad, 7 - 3-pixel Split/All Pixels/All Other

The "standard" grades retained during data processing (Section 5.2.4) are the ASCA grades 0,2,3,4,6, which optimize the signal-to-background ratio.

Two telemetry formats were used in the ACIS observations used in this study, Faint format and Very Faint format. Both formats record the event position in detector coordinates, the event amplitude, and the arrival time. Faint format also records the contents of the 3×3 island determining the grade, whereas Very Faint format records a 5×5 pixel island. The Very Faint format events are graded according to the central 3×3 pixels, however, this format offers a reduced background after processing.

### 3.5 Charge Transfer Inefficiency

After attaining final orbit and a few passages through the Earth's radiation belts, the FI ACIS CCDs showed signs of decreased energy resolution and increased charge transfer inefficiency (CTI), indicating radiation damage. The BI CCDs were unaffected. There are two methods available for correcting for CTI (described in Section 5.2.2) which must be applied to data before a reliable spectral analysis can be performed.

Since this damage was detected, observations cease when the *CXO* nears perigee, and the instruments are protected while in regions of high radiation. The result is that 25% of the *Chandra* orbit is presently unused.

The pre-launch energy resolution of ACIS is shown in Figure 3.8. Due to increased CTI, the energy resolution of the FI CCDs has become a function of the row number. The resolution is near pre-launch values close to the frame store region and is substantially degraded in the farthest row.

### 3.6 Hot Pixels

Hot pixels are pixels that produce a high (incorrect) or saturated pulse-height for many consecutive frames of data. These pixels depend on operating conditions such as temperature, and must be removed from data prior to analysis (see Section 5.2.1).

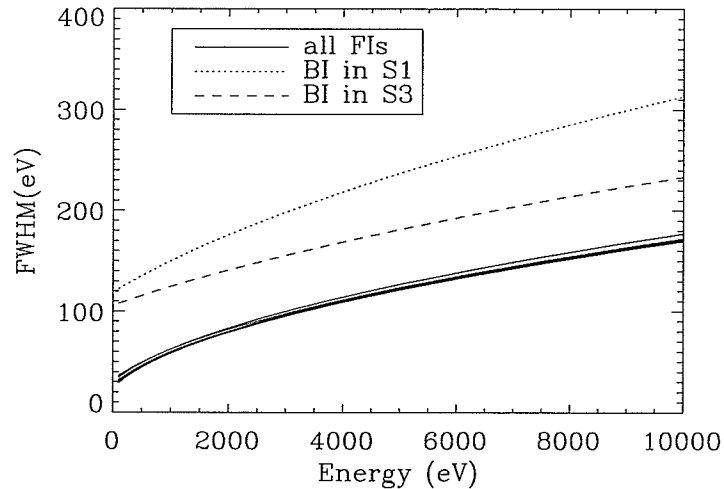


Figure 3.8 - ACIS energy resolution. *Credit: CXC/NASA. Available at [http://cxc.harvard.edu/proposer/ogplots/acis\\_en\\_res\\_FWHM.ps](http://cxc.harvard.edu/proposer/ogplots/acis_en_res_FWHM.ps)*

### 3.7 Effective Area

The effective areas of the imaging instruments are shown in Figure 3.9. There has been a slow decline in the ACIS effective area since launch. The cause is believed to be the build-up of a thin layer of molecular material on the outward-facing side of the Optical Blocking Filters (OBFs). This contaminant has also affected the low energy response of the ACIS. The HRC does not show any signs of contamination.

The effective area is affected most at low energies (above 1 keV, the effective area has decreased by <10%). The molecular coating appears to be thicker at the edges of the OBFs, where the filter is coldest. The contaminant has been found to be composed mainly of carbon, with traces of oxygen and fluorine.

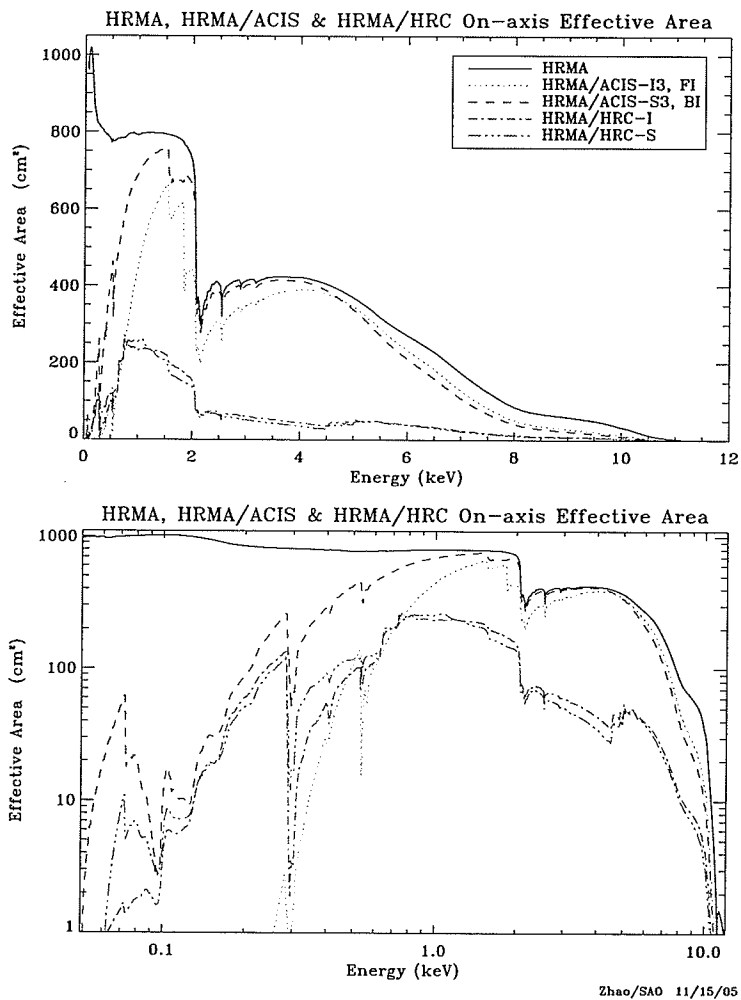


Figure 3.9 - Effective area versus X-ray energy in linear (top) and log (bottom) scale. Credit: CXC/NASA. Available at [http://cxc.harvard.edu/proposer/ogplots/hrma\\_ea\\_onaxis\\_qe.ps](http://cxc.harvard.edu/proposer/ogplots/hrma_ea_onaxis_qe.ps)

### 3.8 Point Spread Function & % Encircled Energy

The point spread function (PSF) is the expected spatial distribution of photons from a point source at a particular location and energy, taking into account the response of the detector and the off-axis angle. Figure 3.10 shows the fractional encircled energy for an on-axis point source.

On-axis, 90% of the encircled energy of a point source is contained within a 2 pixel radius at 1.5 keV, and within a 4 pixel radius at 6.4 keV.

The imaging resolution degrades off-axis because the HRMA PSF increases with increasing off-axis angle (Figure 3.11), and because the deviation between the flat HRC-I detection surface and the curved HRMA focal surface increases off-axis. For these reasons, data with a high ( $>10'$ ) off-axis angle were not used in this thesis (as described in Section 5.1).

Aimpoints (shown in Figure 3.3) are the positions where the flux from a point source with no target offset falls. The aimpoint is not the same as the on-axis position, which is defined as the position of the narrowest PSF and is  $\sim 20''$  from the aimpoints.

### 3.9 Pileup

Pileup occurs when two or more photons are detected as a single event. Pileup causes the energy spectrum to be distorted (spectral hardening occurs because the apparent energy is the sum of two or more energies) and causes the count rate to be underestimated (since two or more events are counted as a single event). Pileup can also cause a change of grade (known as "grade migration") and can cause the

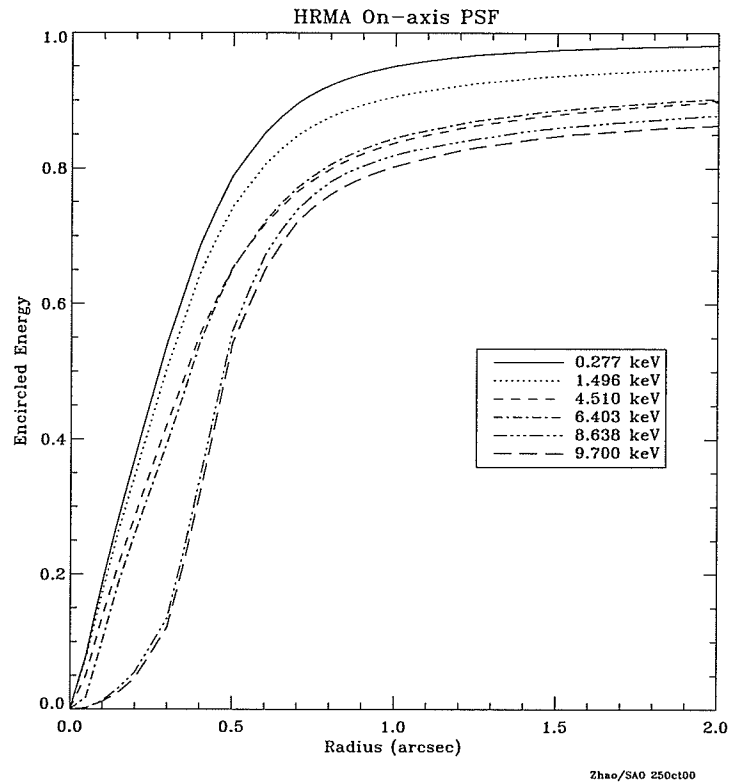


Figure 3.10 - Fractional encircled energy as a function of angular radius, calculated for an on-axis point source. Credit: CXC/NASA. Available at [http://cxc.harvard.edu/proposer/ogplots/hrma\\_psf\\_guide\\_fp.ps](http://cxc.harvard.edu/proposer/ogplots/hrma_psf_guide_fp.ps)

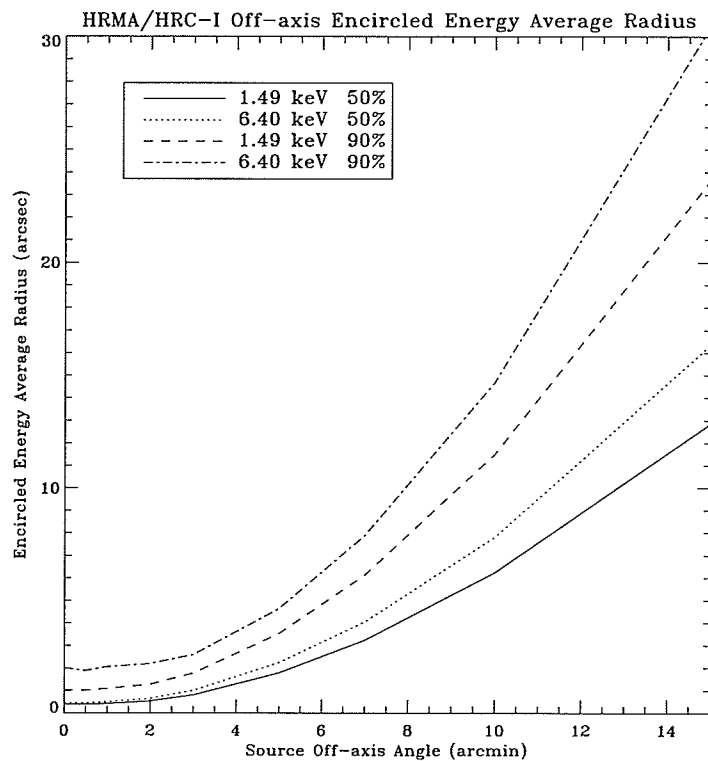


Figure 3.11 - Encircled energy as a function of source off-axis angle for the combined HRMA/HRC-I. Credit: CXC/NASA. Available at [http://cxc.harvard.edu/proposer/ogplots/hrma\\_ee\\_offaxis\\_hrci.ps](http://cxc.harvard.edu/proposer/ogplots/hrma_ee_offaxis_hrci.ps)

total amplitude of the event to be larger than the on-board threshold, causing the event to be rejected altogether and creating a hole in the image. There are methods available to reduce pileup. However, due to low count rates, pileup did not affect the observations used in this thesis, and therefore the details are omitted.

### 3.10 On-orbit Background

The on-orbit background has three components: the cosmic X-ray background, the charged particle background, and the “readout artifact”. The first is due to the cosmic X-ray background and a large portion of it resolves into discrete sources during a *Chandra* observation. The second is due to charged particles, photons, and other neutral particle interactions that deposit energy in the instrument. The third is a consequence of the trailing of the target image. There is also a non-X-ray contribution to the background due to charged particles. A spectrum estimating the background must be subtracted from the data prior to any spectral fitting (Section 7.1).

### 3.11 Data Products

The event file contains information on each photon recorded, including the location, energy, and time of arrival of the photon. The location of the photons can be plotted to create high resolution images in X-ray (Chapter 6). Alternatively, the energy of the photons can be plotted to create spectra (Chapter 7).

# CHAPTER 4

## A HISTORY OF THE SUPERNOVA

### REMNANT G21.5-0.9

G21.5-0.9 was considered a possible supernova remnant (SNR) when it was observed to be a non-thermal source and observers failed to detect hydrogen recombination line emission from it. There have been many studies performed with G21.5-0.9 as the target. This chapter overviews the last 30 years of observations.

#### 4.1 Radio and X-ray Discoveries

In 1976, Becker and Kundu [5] used the National Radio Astronomy Observatory (NRAO) three-element interferometer to map total intensity and linear polarization at 3.7 cm and 11.1 cm to determine the nature of the non-thermal radio source G21.5-0.9. G21.5-0.9 was previously only tentatively considered a SNR due to its small diameter. This was the first high resolution observation to reveal the radio structure of G21.5-0.9 and show an elliptical brightness distribution similar to the Crab Nebula and 3C 58. G21.5-0.9 was found to be well represented by a single Gaussian ellipsoid centred at  $\alpha(1950) = 18^{\text{h}}30^{\text{m}}47^{\text{s}}.33 \pm 0^{\text{s}}.10$ ,  $\delta(1950) = -10^{\circ}36'24''.7 \pm 0''.5$  with a major axis of  $51''.5 \pm 1''.0$  (FWHM) and a minor axis of  $35''.0 \pm 3''.0$  (FWHM), oriented at a

position angle of  $48^\circ \pm 3^\circ$  measured north to east. They did not find any evidence of spectral index variation across G21.5-0.9.

Wilson and Weiler [50] also studied G21.5-0.9 in 1976. They mapped the total intensity and linear polarization of G21.5-0.9 using the Westerbork Synthesis Radio Telescope. The total intensity distribution was found to be relatively smooth with the peak brightness near the geometric centre of the remnant. The spectrum of the integrated emission was found to be represented by a flat power-law ( $S \propto \nu^{-\alpha}$ ) with spectral index  $\alpha = -0.01 \pm 0.04$ . The linear polarization at 6 cm was found to be fairly uniform over the central regions of the source with 10 - 15% being typical values. Wilson and Weiler stated that G21.5-0.9 was most likely a SNR since it is a Galactic object and highly polarized. Further, they claimed that G21.5-0.9 was a filled centre remnant, similar to the Crab Nebula.

In 1978, Altenhoff et al. [1] published a survey of the Galactic plane with the Effelsberg 100-m telescope at 4.875 GHz. G21.5-0.9 was identified with a diameter of  $2.7'$  and a peak flux of 6.38 Jy.

G21.5-0.9 was imaged at 6 cm with the Very Large Array (VLA) and between 0.1 - 4 keV with the Einstein Observatory in 1981 [6]. Both the radio and X-ray images showed a centrally peaked distribution with no indication of a pointlike component. The linearly polarized radio emission was observed to be distributed in a ring with a central minimum. The electric vectors of the polarized radio emission were oriented circumferentially. This data supports the idea that G21.5-0.9 is Crab-like, however, the percentage of the radiated flux emitted as X-rays is lower than the Crab.

Davelaar et al. [18] studied G21.5-0.9 in X-rays using the medium energy (2 -

10 keV) instrument on EXOSAT. They found that G21.5-0.9 was well described by a power-law spectrum with a spectral index of  $0.72 \pm 0.12$ . They found an X-ray column density of  $(1.45 \pm 0.37) \times 10^{22} \text{ cm}^{-2}$ , which is consistent with the VLA 21 cm absorption measurements of G21.5-0.9 that indicate a distance of 5.5 - 9.3 kpc.

In 1987, Morsi and Reich [33] created a map of G21.5-0.9 at 32 GHz with the Effelsberg 100-m telescope. They found that the spectrum of G21.5-0.9 showed no deviation from a low-frequency extrapolation, implying that the spectral break (Section 2.2) must lie at higher frequencies.

Fürst et al. [20] performed 22.3 GHz observations of G21.5-0.9 with the NRO Millimeter-wave Array in 1987. G21.5-0.9 showed axisymmetric filaments as well as a diffuse centrally peaked component. They suggested that the properties of the diffuse component and the morphology of the filaments indicated that they resulted from a two-sided collimated outflow of particles in precession from a central “pulsar”. The geometrical structure of the filaments produced an estimate of the location of the “pulsar” of  $\alpha(1950) = 18^{\text{h}}45^{\text{m}}5$ ,  $\delta(1950) = -10^{\circ}36'25''$ . They also found that the X-ray maximum was located in a minimum in the small-scale radio emission, suggesting the two types of emission originate from the pulsar in a different way.

Salter et al. [40] studied G21.5-0.9 at 84 GHz with the NRAO 12 m telescope. The size ( $50'' \pm 10''$ ) of G21.5-0.9 was found to be consistent with previous estimates.

Salter et al. [39] also studied G21.5-0.9 at 90 GHz and 142 GHz (resolutions of  $28''$  and  $20''$ , respectively). They confirmed the presence of a spectral break (Section 2.2) near 40 GHz.

Asaoka and Koyama [3] studied Crab-like SNRs and speculated that all Crab-like

remnants have a spectrum described by a power-law with a photon index near 2 in the energy range 2 - 20 keV. Slight differences from the value 2 were suggested to be due to differences in the boundary conditions of pulsar shock winds. The observed X-ray spectrum of G21.5-0.9 suggested the emission is mainly non-thermal emission from a synchrotron nebula. Earlier Davelaar et al. [18] found a photon index of less than 2 and stated that the X-ray spectrum was too hard to originate from shock-accelerated electrons. Asaoka and Koyama state that this is the case if pulsar wind shocks are non-relativistic. However, they claim that relativistic shocks are more realistic and give harder power-laws of electrons.

Kassim [25] states that low frequency measurements can assist in distinguishing between steeper (softer) spectrum shell-type emission and flatter (harder) spectrum plerionic emission. Kassim provides evidence that the spectrum of G21.5-0.9 becomes steeper at lower frequencies. He speculates that there may be a weak component with a steeper spectrum due to shell-type emission that has been missed in high frequency observations. He suggests a search is needed at 330 MHz for the shell and to see if G21.5-0.9 should be reclassified as a composite type remnant (Section 1.3).

One theory for the lack of visible shells surrounding plerionic remnants is that the supernova occurred in regions of the interstellar medium having lower than average densities. These regions could have been caused by previous SNe, stellar winds from nearby stars, or a strong wind from the SNR's own progenitor. Wallace et al. [47] searched for HI voids around plerionic remnants. While they found evidence of bubbles around the Crab Nebula, 3C 58, and G74.9+1.2 (CTB 87), their results were inconclusive for G21.5-0.9. There was no noticeable bubble surrounding G21.5-0.9,

however, the distance to G21.5-0.9 is large enough that a bubble comparable in size to those around the Crab and 3C 58 would be undetectable in the low resolution data used in this study.

Wallace et al. [47] provided a possible evolutionary scenario for remnants of massive SNe in 1994, assuming the hypotheses that all plerionic remnants exist in low-density surroundings and, that all plerionic remnants are surrounded by an invisible halo of ejecta, are valid. When massive stars explode they are believed to leave behind a neutron star (pulsar), which creates a pulsar wind nebula that is observed as a plerion. The stellar ejecta expands into the low density bubble that was evacuated by the SN progenitor. In this phase the SN shell will not be visible because the amount of material swept-up is small. When the SN ejecta expands and reaches the shell blown out by the progenitor, it will become visible. If the plerion is still visible, a composite remnant is then observed. If the plerion disappears on a time scale shorter than the shell (this could happen if the pulsar moves out of the region where the SN occurred), a shell remnant is observed. Therefore, the evolutionary sequence could be plerion, composite, shell.

In 1996, Biggs and Lyne [8] performed a search for radio pulsars in SNRs. They did not find a pulsar in G21.5-0.9 but placed an upper limit on the pulsed emission of 4 mJy at 400 MHz.

## 4.2 Modern X-ray Observations

G21.5-0.9 was a calibration target for the *Chandra* X-ray Observatory, resulting in the public availability of data soon after observation. Two groups used early *Chandra* observations of G21.5-0.9 to look at the newly observed compact remnant and the X-ray halo.

Slane et al. [44] used a HRC-I observation, and two ACIS-S3 observations, while Safi-Harb et al. [38] used 6 early *Chandra* observations to study G21.5-0.9. Both groups used timing data from the central compact region to search for pulsations. Neither found evidence for pulsations. Slane et al. placed an upper limit of  $\sim 40\%$  on the pulsed fraction in 0.1-10 keV while Safi-Harb et al. derived an upper limit of 16% for the pulsed fraction. The plerion was observed to have a radius of  $30''$  with a distinct indentation in the northwest, and a faint X-ray halo was observed out to a radius of  $150''$ . The plerion was found to have a non-thermal spectrum, indicating the presence of a central pulsar.

Both groups [44, 38] found the spectral index increases with radius in the plerion. This spectral softening had also been observed for 3C 58 and can be explained by synchrotron burn-off of electrons accelerated in the central regions (due to the short synchrotron lifetime for higher energy electrons, only the lower energy component is able to survive to the outer regions of the plerion). Safi-Harb et al. found that the halo is hardest in the north, where knots and filaments extend from the core to the outer halo. Slane et al. found the spectrum of the halo could be fit by either a power-law or an optically thin thermal spectrum. Safi-Harb et al. found that

the spectrum of the entire remnant was dominated by non-thermal emission. This suggested that all of the emission could be due to synchrotron radiation from high energy electrons originating from the pulsar as a wind or jets interacting with the surrounding medium. They also noted that since G21.5-0.9 is bright and heavily absorbed a significant portion of the emitted X-rays could interact with dust and be scattered, forming a halo around the bright core.

Safi-Harb et al. used the formula

$$\log L_X = 1.39 \log \dot{E} - 16.6 \quad (4.1)$$

by Seward & Wang [42] to estimate the period of the undiscovered pulsar (the discovery is discussed in Section 4.3) as

$$P = 0.144 \left( \frac{I_{45}}{\dot{E}_{37} \tau_3} \right)^{1/2} \text{ s}, \quad (4.2)$$

where  $I = 10^{45} I_{45} \text{ g cm}^2$  is the moment of inertia,  $\dot{E} = 10^{37} \dot{E}_{37} \text{ erg s}^{-1}$  is the spin-down energy loss, a braking index of  $n = 3$  is assumed, and  $\tau = \tau_3 \times (3\text{kyr})$  is the characteristic age of the pulsar. They also estimated  $\dot{E}_{37} \sim 3 - 6$  and  $B = 3.2 \times 10^{13} I_{45}^{3/2} \dot{E}_{37}^{-1/2} \tau_3^{-1} R_{10}^{-3} \text{ G}$ , where  $R = 10 R_{10} \text{ km}$  is the neutron star radius.

Bock et al. [11] were unable to detect the X-ray halo at 94 GHz and set a brightness limit of 20 - 200 mJy arcmin<sup>-1</sup> on the halo. Since G21.5-0.9 was found to have a similar structure at millimeter and longer radio wavelengths, there is no indication of a change in the radio spectral index with radius. Since radial variations in the spectrum were observed in X-ray, Bock et al. proposed that the break frequency is higher than  $\sim 100 \text{ GHz}$ .

Warwick et al. [48] studied G21.5-0.9 using 30 ks of XMM-Newton data. As with the early *Chandra* data, an indentation is observed in the northwest of the plerion, a “spur” appears to track north from the core and then turn at  $100''$  and arc to the northeast, and a nearly circular low surface brightness halo is observed to  $150''$ . The spectral index steadily increases with an increase in radius across G21.5-0.9. The point source in the southwest of the remnant is found to have a hard spectrum ( $\Gamma = 1.61 \pm 0.34$  or  $kT \sim 7$  keV) with a column density of  $1.03 \pm 0.22 \times 10^{22}$   $\text{cm}^{-2}$ , implying it is a foreground object, and is found to coincide with the emission-line star SS 397. The spectrum of the halo was found to lack any significant line features, implying that if the emission is thermal the plasma is far from equilibrium. The temperature for the continuum emission was found to be 4 - 5 keV, and Warwick et al. concluded that the halo was non-thermal. This, along with the lack of observed limb-brightening, led Warwick et al. to conclude that the halo was an extension of the synchrotron nebula.

Palombara and Mereghetti [35] used four XMM-Newton observations ( $\sim 30$  ks each) to perform a deep search for pulsations in the core of G21.5-0.9. No pulsations were detected (although, the search was limited to periods longer than 146 ms) and an upper limit of 7.5% - 40% was placed on the pulsed fraction, depending on frequency and energy range.

Bright and heavily absorbed sources have a large fraction of the emitted X-rays scattered due to interactions with dust. Bandiera and Bocchino [4] investigated the idea that the X-ray halo of G21.5-0.9 is an effect of dust scattering in the foreground medium. Dust scattering cannot explain the knots in the north of the remnant.

However, a good fit to the remainder of the halo was found by modelling the halo as a uniform sphere with  $200''$  radius and a surface brightness of  $10^{-4}$  times that of the inner component. They note that this is not a unique solution.

Bocchino [9] detected a soft thermal X-ray component in the northern knots of G21.5-0.9. A collisional ionization equilibrium model for a hot optically thin plasma was used to calculate a temperature of  $kT = 0.12 - 0.24$  keV, a mass of  $0.3M_{\odot} - 1.0M_{\odot}$ , and a density of  $1.6 - 6$   $\text{cm}^{-3}$ . Bocchino also suggested there is an overabundance of silicon with respect to solar, which implies the knot is a clump of shocked ejecta.

Bocchino et al. [10] used *XMM* and *Chandra* data to study the halo of G21.5-0.9. They propose that the halo is composed of: (1) diffuse extended emission due to dust scattering of X-rays from the plerion, (2) a bright limb tracing particle acceleration in the forward shock of the remnant, and (3) a knot of ejecta in adiabatic expansion (northern knots). They also claim that the remnant is young (200 - 1000 yr.).

### 4.3 PSR J1833-1034 Discovery

Gupta et al. [23] and Camilo et al. [14] independently discovered the pulsar associated with G21.5-0.9 in 2005. Gupta et al. used the Giant Meterwave Radio Telescope (GMRT) while Camilo et al. used the Parkes telescope. Both groups found that the pulsar (PSR J1833-1034) has a period of  $P = 61.86$  ms and a period derivative of  $\dot{P} = 2.0 \times 10^{-13}$ , which is typical for young pulsars in SNRs. They then calculated a characteristic age of  $\tau \sim 4900$  years, a surface magnetic field of  $B = 3.6 \times 10^{12}$  G, and a spin-down luminosity of  $\dot{E} = 3.3 \times 10^{37}$  erg  $\text{s}^{-1}$ , which makes PSR J1833-1034

the second most energetic Galactic pulsar. Using X-ray and radio observations of the pulsar wind nebula, Camilo et al. argue that the age of G21.5-0.9 and PSR J1833-1034 is  $\lesssim 1000$  yr and therefore the initial spin period of PSR J1833-1034 was  $\gtrsim 55$  ms.

Note that Equation 4.2 is satisfied by the above values of  $\dot{E}$ ,  $\tau$ , and  $P$ .

## 4.4 Distance Estimate to G21.5-0.9

Safi-Harb et al. [38] and Camilo et al. [14] used a compilation of the above work on G21.5-0.9 to conclude that the best estimate of the distance to G21.5-0.9 was 5 kpc and scaled the results of their work to a distance of 5 kpc. CO and HI absorption surveys yield a kinematic distance to G21.5-0.9 of  $4.7 \pm 0.4$  kpc [14]. X-ray spectra of G21.5-0.9 imply a large amount of molecular material in the direction of the remnant which contributes to a high foreground absorbing column of  $N_{\text{H}} \sim 2 \times 10^{22}$  atoms  $\text{cm}^{-2}$  [14]. Using X-ray derived  $N_{\text{H}}$  values, Safi-Harb et al. [38] estimate the distance to G21.5-0.9 as  $4.1 \text{ kpc} < d < 5.2 \text{ kpc}$ . In this thesis, 5 kpc is accepted as the distance to G21.5-0.9 and used in any calculations requiring a distance estimate.

## 4.5 Motivation for Chandra Study of G21.5-0.9

Since there is a large number of archived observations of G21.5-0.9, these observations are available to be combined to produce a large effective exposure. A shell surrounding a Crab-like nebula has been searched for for decades. The amount of *Chandra* data

available on G21.5-0.9 made it a good candidate for conducting a deep search for a shell.

An early *Chandra* observation of G21.5-0.9 showed a “halo” of X-ray emission surrounding the previously known plerion. The source of this X-ray emission is investigated in the following chapters.

This thesis presents the longest exposure of a plerionic remnant to date and shows the first image of a shell surrounding a PWN. Images of G21.5-0.9 in various energy bands and with two *Chandra* instruments show an X-ray halo surrounding the plerion and bright knots of X-ray emission in the halo (Sections 6.1-6.4). These long exposures also reveal a complicated structure in the PWN itself. Other plerionic remnants (most notably the Crab and Vela nebulae) have been observed to vary in morphology over time, with knots moving at  $\sim 0.5c$ , where  $c$  is the speed of light (Hester et al., 2002 [24], Pavlov et al., 2003 [36]). The results of a search for similar variability in G21.5-0.9 are presented in Section 6.5.

The observation of limb-brightening at the boundary of the X-ray halo led to a spectroscopic study in order to determine if the X-ray emission was thermal (due to the SNR shell) or non-thermal (due to an extension of the plerion or dust scattering). The results of spectroscopy on data from the limb, as well as data from the plerion, knots and halo, are presented in Chapter 7.

# CHAPTER 5

## CHANDRA OBSERVATIONS AND DATA

### PREPARATION

G21.5-0.9 was chosen as a calibration target for the *Chandra* X-ray Observatory since it was thought to be a textbook example of a plerionic remnant. As a result, G21.5-0.9 has been frequently observed using the Advanced CCD Imaging Spectrometer (ACIS) and the High Resolution Camera (HRC). *Chandra* calibration observations are archived shortly after being acquired. This thesis makes use of the many available observations to conduct the deepest study of G21.5-0.9, and of any plerion, to date.

Section 5.1 describes the *Chandra* observations used in this study. Section 5.2 describes the process of ‘cleaning’ the ACIS data to prepare it for use in scientific analysis. Section 5.3 describes the preparation of the HRC data.

#### 5.1 Observations

Observations performed with *Chandra* are assigned an observation identifier (obsID) which is used to uniquely refer to a dataset.

In this study, 78 available ACIS observations of G21.5-0.9 between launch (July 23, 1999) and Feb. 2006 were considered. 11 of these observations (obsID 163, 164,

166, 167, 1267, 1432, 1841, 1842, 1843, 4354, 4355) were found to have an off-axis angle greater than  $10'$  (Section 3.8) and were therefore not used in the imaging or spectroscopic analysis. In addition, two observations (2865, 2866) were performed with incorrect coordinates and missed the target. 7 observations (obsID 158, 159, 160, 161, 162, 165, 1230) were taken at  $-100^{\circ}\text{C}$  and were used in the imaging but not in the spectroscopy since there is no CTI correction available for data at this temperature (see Section 5.2.2). In total, 65 observations were used in the imaging analysis for **a total integrated exposure time of 578.6 ks** and 56 ACIS observations<sup>1</sup> were used in the spectroscopic analysis (exposure of **480.2 ks**).

All 15 available HRC-I observations between launch and Feb. 2006 were also used in the imaging analysis, for **an additional exposure of 278.4 ks**.

The observations used in the analysis, described in Chapters 6 and 7, are listed in Tables 5.1 and 5.2.

---

<sup>1</sup>Observations 6740 and 6741 were performed late in this analysis and were therefore not included in the spectroscopy.

Table 5.1. *Chandra* ACIS observations of the supernova remnant G21.5-0.9.

obsID <sup>a</sup>	Detector	Observation Date (yyyy-mm-dd)	Temperature (°C)	Exposure (ks)	Off-axis angle (')
158	ACIS-I1	1999-08-25	-100	9.6	5.86
159	ACIS-S3	1999-08-23	-100	14.8	0.32
160	ACIS-I0	1999-08-25	-100	9.6	6.75
161	ACIS-I2	1999-08-25	-100	9.6	5.96
162	ACIS-I3	1999-08-27	-100	13.0	1.74
165	ACIS-S2	1999-08-23	-100	9.6	6.23
1230	ACIS-S3	1999-08-23	-100	12.4	0.32
1233	ACIS-I3	1999-11-05	-110	14.0	1.73
1433	ACIS-S3	1999-11-15	-110	15.0	1.29
1434	ACIS-S2	1999-11-16	-110	9.6	6.22
1441	ACIS-I0	1999-11-15	-110	9.1	9.30
1442	ACIS-I1	1999-11-15	-110	9.6	5.87
1443	ACIS-I2	1999-11-15	-110	9.7	5.95
1551	ACIS-I3	2001-03-08	-120	8.7	2.56
1552	ACIS-I3	2001-07-13	-120	9.9	2.51
1553	ACIS-S3	2001-03-18	-120	9.7	1.33
1554	ACIS-S3	2001-07-21	-120	9.0	1.24
1716	ACIS-S3	2000-05-23	-120	7.7	1.32
1717	ACIS-S3	2000-05-23	-120	7.5	1.33
1718	ACIS-S3	2000-05-23	-120	7.6	1.34
1719	ACIS-I1	2000-05-23	-120	7.6	7.34
1720	ACIS-I1	2000-05-23	-120	7.5	5.84
1721	ACIS-I1	2000-05-23	-120	7.6	4.34
1722	ACIS-I1	2000-05-23	-120	7.6	2.59
1723	ACIS-I1	2000-05-23	-120	7.6	0.83
1724	ACIS-I3	2000-05-24	-120	7.6	5.83
1725	ACIS-I3	2000-05-24	-120	7.6	4.33
1726	ACIS-I3	2000-05-24	-120	7.6	2.59
1727	ACIS-S2	2000-05-24	-120	7.7	4.70
1728	ACIS-S2	2000-05-24	-120	7.5	4.69
1729	ACIS-S2	2000-05-24	-120	7.6	4.68
1769	ACIS-S3	2000-07-05	-110	7.4	1.30
1770	ACIS-S3	2000-07-05	-110	7.2	1.31
1771	ACIS-S3	2000-07-05	-110	7.2	1.31
1772	ACIS-I1	2000-07-05	-110	7.4	7.32
1773	ACIS-I1	2000-07-05	-110	7.2	5.81
1774	ACIS-I1	2000-07-05	-110	7.2	4.31
1775	ACIS-I1	2000-07-05	-110	7.2	2.56
1776	ACIS-I1	2000-07-06	-110	7.2	0.82
1777	ACIS-I3	2000-07-06	-110	7.2	5.80
1778	ACIS-I3	2000-07-06	-110	7.2	4.30
1779	ACIS-I3	2000-07-06	-110	7.2	2.55
1780	ACIS-S2	2000-07-05	-110	7.2	4.72
1781	ACIS-S2	2000-07-05	-110	7.2	4.73

Table 5.1—Continued

obsID <sup>a</sup>	Detector	Observation Date (yyyy-mm-dd)	Temperature (°C)	Exposure (ks)	Off-axis angle (')
1782	ACIS-S2	2000-07-05	-110	7.2	4.71
1838	ACIS-S3	2000-09-02	-120	7.9	1.28
1839	ACIS-S3	2000-09-02	-120	7.7	2.49
1840	ACIS-S3	2000-09-02	-120	7.7	5.30
2872	ACIS-I3	2002-09-13	-120	9.8	3.79
2873	ACIS-S3	2002-09-14	-120	9.8	1.22
3473	ACIS-I3	2002-05-16	-120	9.3	7.08
3474	ACIS-S3	2002-05-16	-120	9.3	7.04
3692	ACIS-I3	2003-05-16	-120	9.2	2.52
3693	ACIS-S3	2003-05-16	-120	9.8	1.26
3699	ACIS-I3	2003-11-09	-120	10.1	3.79
3700	ACIS-S3	2003-11-09	-120	9.5	1.23
4353	ACIS-S3	2003-05-15	-120	9.4	5.25
5158 <sup>b</sup>	ACIS-I3	2005-02-26	-120	10.0	3.78
5159 <sup>b</sup>	ACIS-S3	2004-10-27	-120	9.8	1.22
5165	ACIS-I3	2004-03-26	-120	9.6	3.81
5166	ACIS-S3	2004-03-14	-120	10.0	1.26
6070 <sup>b</sup>	ACIS-I3	2005-02-26	-120	9.4	3.78
6071 <sup>b</sup>	ACIS-S3	2005-02-26	-120	9.6	1.27
6740 <sup>b,c</sup>	ACIS-I3	2006-02-21	-120	9.8	3.80
6741 <sup>b,c</sup>	ACIS-S3	2006-02-22	-120	9.8	1.27

<sup>a</sup>Additional observations of G21.5-0.9 (163, 164, 166, 167, 1267, 1432, 1841, 1842, 1843, 4354, 4355) with *Chandra* had an off-axis angle  $> 10'$  (Section 3.8) and were not used in the imaging or spectroscopic analysis.

<sup>b</sup>Observations 5158, 5159, 6070, 6071, 6740, and 6741 were performed subsequent to the construction of the energy (“true colour”) image and were therefore not included in that portion of the analysis.

<sup>c</sup>Observations 6740 and 6741 were performed late in this analysis and were therefore not included in the spectroscopy or the true colour image.

The data processing was performed using the CIAO<sup>2</sup> software package, version 3.2.1, with CALDB version 3.0.1, which was designed for use with data from *Chandra*. Each observation was processed individually to create a ‘cleaned’ event file (a listing of photons striking the detectors during the observation), as described in the following sections. The scripts written to assist in the data processing are provided in Appendices A.1 and A.2.

<sup>2</sup>Chandra Interactive Analysis of Observations (CIAO), <http://cxc.harvard.edu/ciao/>

Table 5.2. *Chandra* HRC-I observations of the supernova remnant G21.5-0.9.

obsID	Observation Date (yyyy-mm-dd)	Exposure (ks)	Off-axis angle (')
142	2000-02-16	30.3	0.29
143	1999-09-04	15.0	0.30
144	2000-09-01	30.0	0.29
1242	1999-09-04	14.5	0.36
1298	1999-09-04	7.2	0.33
1406	1999-10-25	29.9	0.28
1555	2001-03-09	9.0	0.28
1556	2001-07-13	10.1	0.27
2867	2002-03-12	19.1	0.28
2874	2002-07-15	19.9	0.28
3694	2003-05-15	18.4	0.27
3701	2003-11-09	19.1	0.25
5167	2004-03-25	19.1	0.25
6072	2005-02-26	19.0	0.27
6742	2006-02-21	20.0	0.27

## 5.2 ACIS Data Filtering

### 5.2.1 Removing Bad Pixels

Each observation had an associated bad pixel file which listed the pixels on the CCDs that could not be trusted to give valid results during the observation. These bad pixels could be hot pixels, which are pixels that produce an artificially high or saturated pulse-height for a large number of consecutive data frames. Any photons which fell on bad pixels during the observation were ignored in the data cleaning process (*acis\_process\_events*, Section 5.2.3) and excluded from the cleaned files that were used in the analysis.

### 5.2.2 Correction for Charge Transfer Inefficiency

Charge transfer inefficiency (CTI) is the term used to describe the loss of charge in a CCD as data is transferred from one pixel to the next during readout. Early in the *Chandra* mission, damage was suffered by the ACIS chips, which greatly increased the amount of CTI (see Section 3.5). The effect of CTI on the data is that the grade given to events can be altered, with the result that some good grade events will be rejected.

CTI affects the observed spectral distribution of sources by shifting the pulse-height distribution of a source to lower pulse-heights, thus producing a gain shift (Section 5.2.3). CTI also causes a loss in the energy resolution of the CCDs, by broadening the pulse-height distribution of a monoenergetic feature.

To compensate for the effects of cosmic radiation damage, a charge transfer inefficiency correction was applied to the ACIS data (CIAO CTI correction<sup>3</sup> for ACIS-I, -120°C data, Penn State CTI correction<sup>4</sup> [46] for ACIS-I, -110°C and ACIS-S, -110°C and -120°C data). The -100°C data, from ACIS-I or ACIS-S, cannot currently be corrected and therefore spectra were not obtained from the -100°C observations performed of G21.5-0.9.

The ACIS-I -120°C data was corrected with a CTI corrector available in the CIAO tool *acis\_process\_events* (which can correct only ACIS-I -120°C or S2 -120°C data).

The ACIS-S data and the ACIS-I -110°C data was corrected for CTI with a CTI corrector (*correctit*) produced by Penn State (which can correct ACIS-I, S2 or S3, and

---

<sup>3</sup><http://cxc.harvard.edu/ciao/why/cti.html>

<sup>4</sup><http://www.astro.psu.edu/users/townsley/cti/>

-110°C or -120°C data). The Penn State corrector is designed to work only with data from chips 0, 1, 2, 3, 6, or 7 (I0, I1, I2, I3, S2, S3, see layout in Figure 3.3). As a result, the CIAO tool *dmcoppy* was used to filter the *evt1* (unfiltered list of photon events) file provided with the observation. Only data from chips which the corrector could handle were kept.

### 5.2.3 Gain

After correcting for CTI, a gain table was applied to the data using the CIAO tool *acis\_process\_events*. This tool computes the energy and the pulse invariant (PI) of each event from the pulse height amplitude (PHA) value, which is present in the raw data from *Chandra*. The PI values are used during spectral analysis to separate the observed counts into energy bins.

### 5.2.4 Grades & Status

After correcting for CTI and gain, the data was filtered for bad grades (using ASCA grading, grade = 0,2,3,4,6 were kept) and good status (status = 0) using *dmcoppy*.

A filter was also applied to the data to filter for good time intervals (GTIs) using *dmcoppy*. This removes periods during the observation with high background rates or with unstable aspect.

The data is now fully reduced and there is one *evt2* (cleaned event list) file per observation.

### 5.2.5 Merging Multiple Observations

For use in the imaging analysis, all observations were merged to form one combined dataset. First, all observations were reprojected so that they were aligned using the CIAO tool *reproject\_events*. That is, the image coordinates of each observation were recalculated so that all of the images lined up and the images could then be overlaid. The observations were merged using the tool *dmmerge* to combine the individual observation files into one file listing all events (photons) observed during the observations.

## 5.3 HRC

The procedure for cleaning HRC data is much the same as that for the ACIS. The bad pixel file is used by *hrc\_process\_events*, which also applies a gain table to the data. The HRC has poor energy resolution and since it is not used for spectroscopy there is no CTI correction needed. Data from the HRC is not assigned grades, as a result the data is filtered by status only (using *dmcoppy*). The filtering for GTIs is also performed with *dmcoppy*. Multiple observations are merged using the same procedure as for the ACIS data.

# CHAPTER 6

## A CHANDRA STUDY OF G21.5-0.9: IMAGING

The data was prepared as described in Chapter 5. All observations with an off-axis angle  $< 10'$  were used in the imaging analysis of G21.5-0.9. The photons in each event file can be plotted according to the 'sky coordinates' (transformed version of the detector coordinates), giving a 2D image of the target object.

Section 6.1 shows the results of combining all the data to effectively create one long observation. Section 6.2 shows the ACIS data in various energy bands. Section 6.3 discusses the morphology of G21.5-0.9 revealed by these new images. Section 6.4 shows variations in surface brightness with radius, originating at the pulsar PSR J1833-1034. Section 6.5 describes a search for variability in G21.5-0.9.

### 6.1 Combined Image

The result of combining the ACIS observations (**effective exposure of 578.6 ks**) is shown in Figure 6.1(a), and the result of combining the HRC-I observations (**effective exposure of 278.4 ks**) is shown in Figure 6.2(a). Both images are  $350''$  on a side and the intensity (number of photons detected) is plotted on a log scale. Figures 6.1(b)

and 6.2(b) are the result of smoothing Figures 6.1(a) and 6.2(a) with Gaussians of  $\sigma = 1.5''$  and  $\sigma = 0.53''$ , respectively. Figures 6.3 and 6.4 are close-ups of the plerion (images are  $90''$  on a side). The images have not been exposure corrected. All images were created using *ximage*<sup>1</sup> and are centred on the pulsar at  $\alpha(2000) = 18^{\text{h}}33^{\text{m}}33^{\text{s}}.54$ ,  $\delta(2000) = -10^{\circ}34'07''.6$ . In all images, north is toward the top of the page and east is toward the left. The bright point source in the southwest of the X-ray halo is the foreground star SS 397.

## 6.2 Energy Image

The ACIS combined image of Figure 6.1 was divided into three energy bands, shown in Figure 6.5. Figure 6.5(a) is the soft energy band (0.2-1.5 keV), Figure 6.5(b) is the medium energy band (1.5-3.0 keV), and Figure 6.5(c) is the hard energy band (3.0-10.0 keV). We can see that the halo is most visible in the medium energy (green) image and least visible in the hard energy (blue) image.

Assigning the colour red to the soft image, green to the medium image, and blue to the hard image, an energy (“true colour”) image was created, as shown in Figure 6.6. The three colour images were added using the *GIMP*<sup>2</sup> and the contrast was adjusted to bring out the faint features of the X-ray halo, which appears to be nearly circular and centred on the pulsar PSR J1833-1034.

---

<sup>1</sup>*ximage*, version 4.1, <http://heasarc.gsfc.nasa.gov/docs/software/lheasoft/xanadu/ximage/ximage.html>.

<sup>2</sup>GNU Image Manipulation Program (GIMP), version 1.2.3, <http://www.gimp.org/>

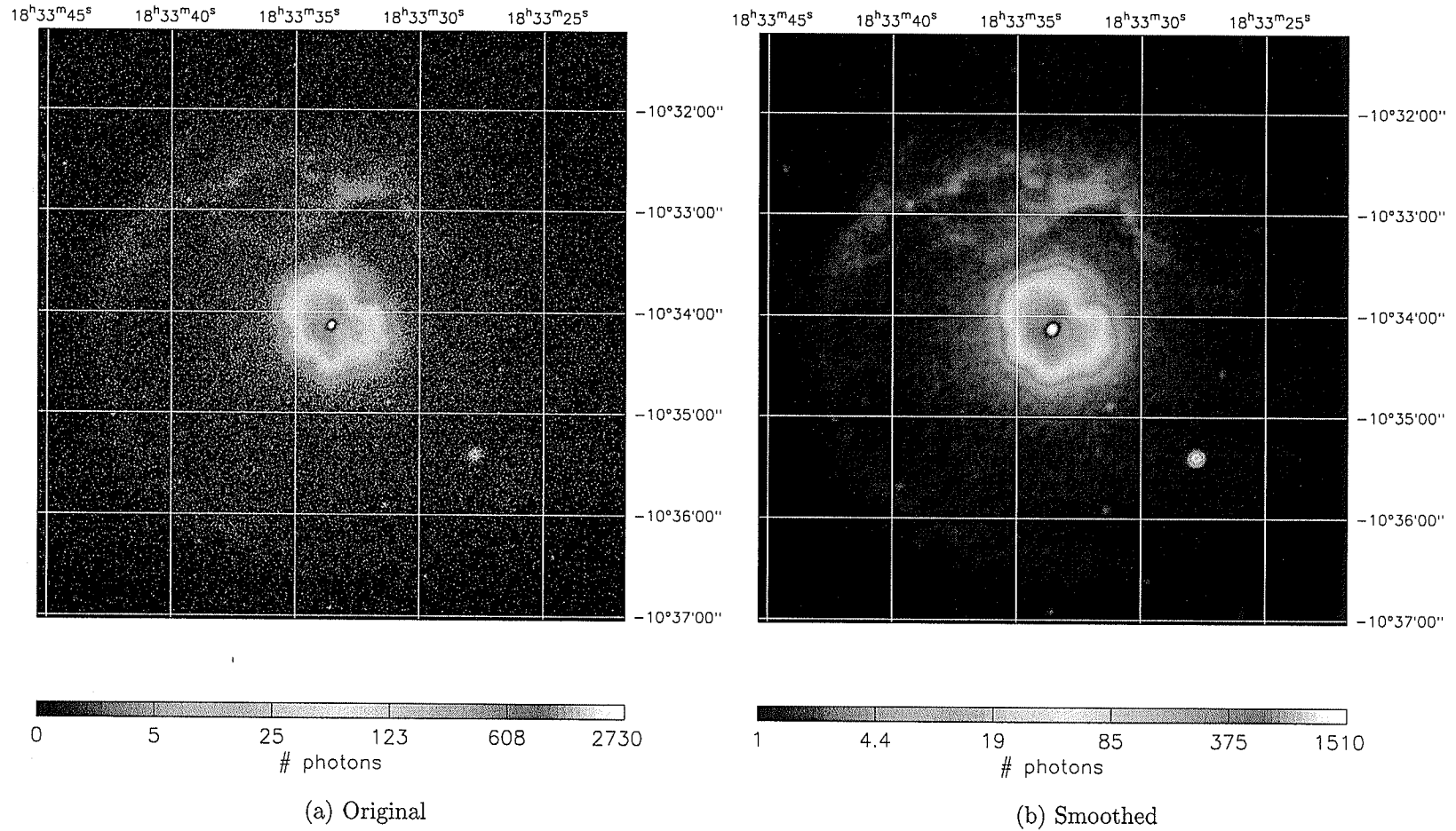


Figure 6.1 - ACIS combined data. The total exposure time is 578.6 ks and the image is  $350''$  on a side. (b) is the result of smoothing (a) with a Gaussian of  $\sigma = 1.5''$ . North is up and east is to the left. The point source in the southwest of the image is the foreground star SS 397.

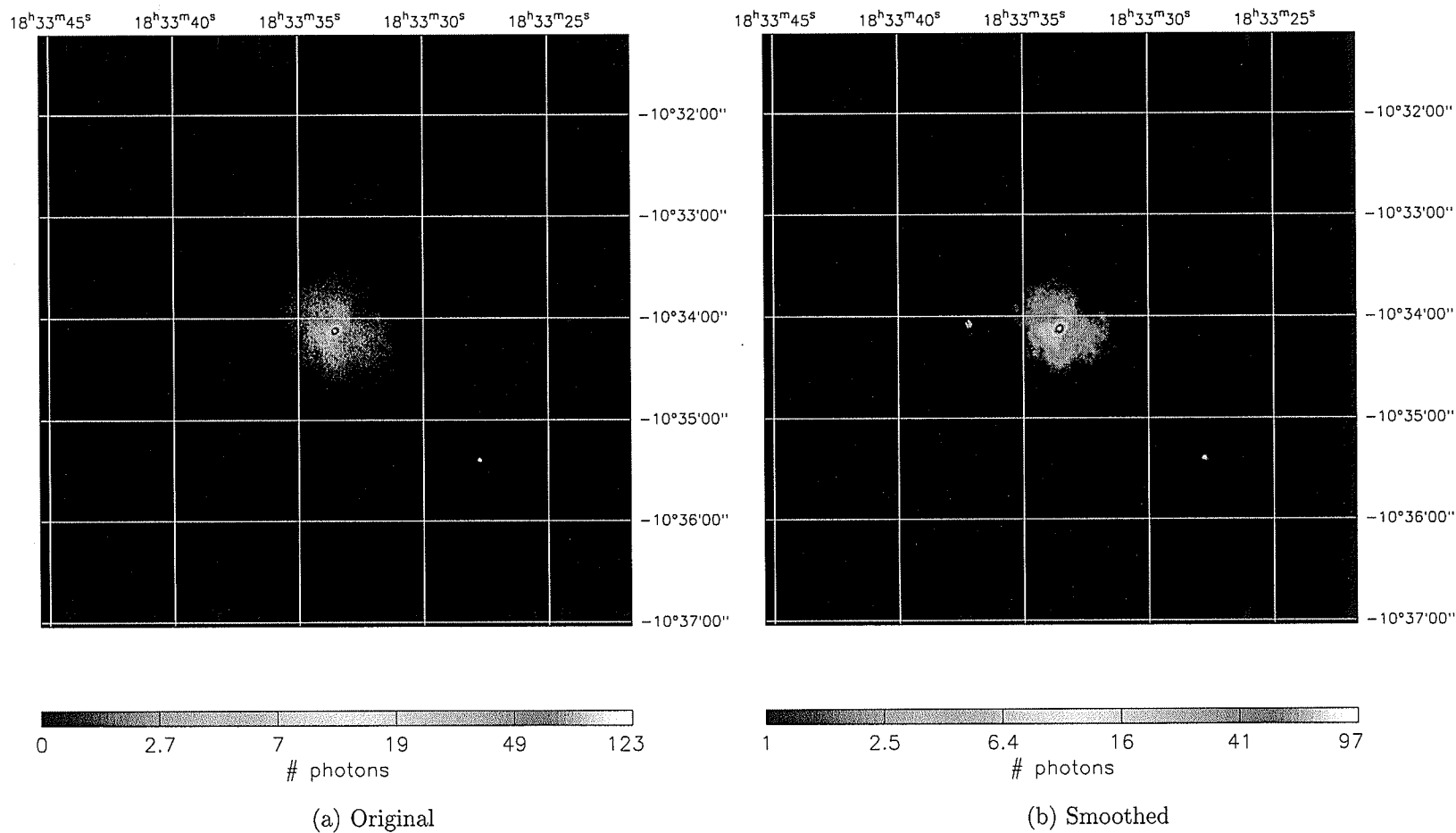


Figure 6.2 - HRC-I combined data. The total exposure time is 278.4 ks and the image is 350'' on a side (same scale as Figure 6.1). (b) is the result of smoothing (a) with a Gaussian of  $\sigma = 0.53''$ . North is up and east is to the left. The point source in the southwest of the image is the foreground star SS 397.

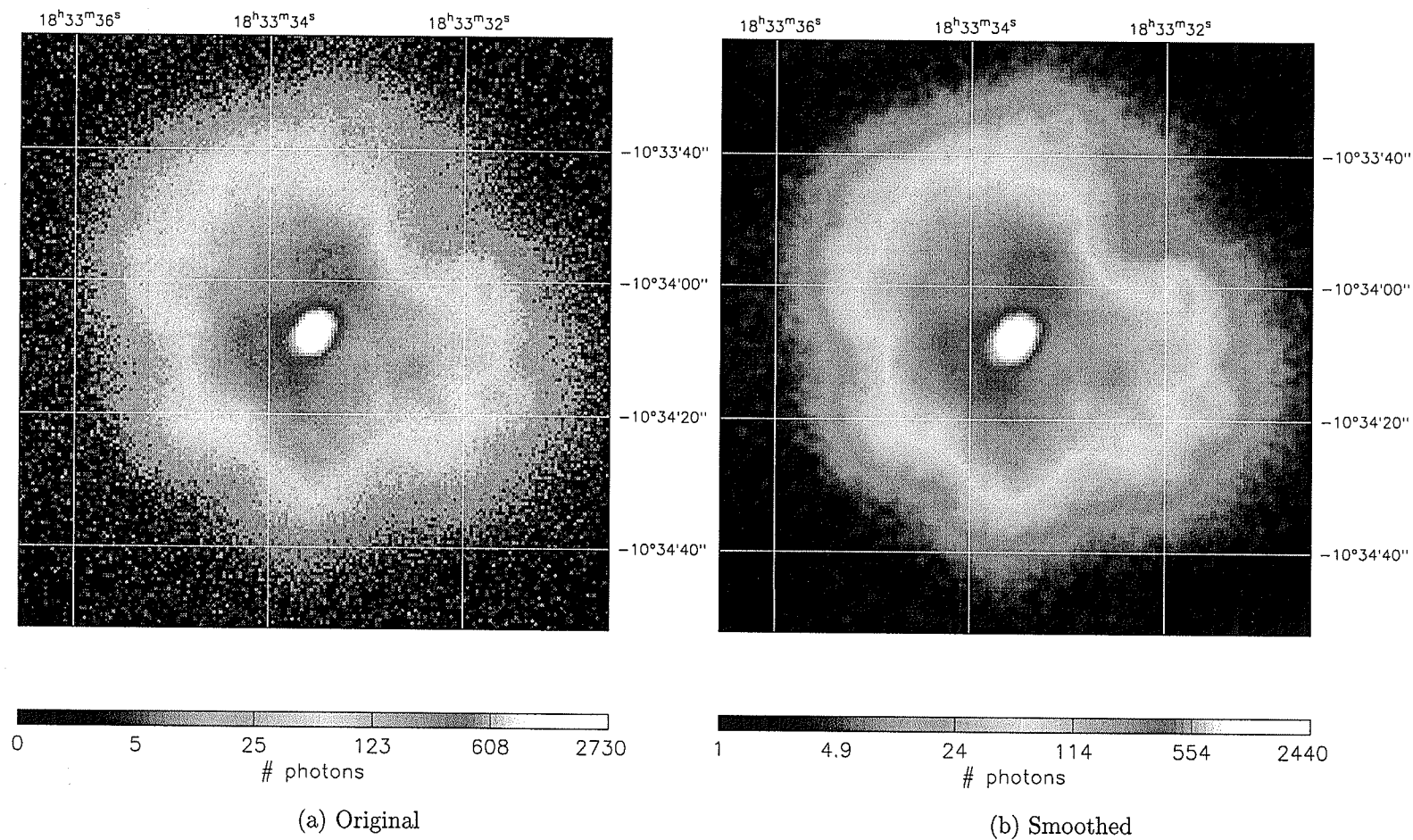


Figure 6.3 - ACIS combined data of the plerion only. The total exposure time is 578.6 ks and the image is  $90''$  on a side. (b) is the result of smoothing (a) with a Gaussian of  $\sigma = 0.5''$ . North is up and east is to the left.

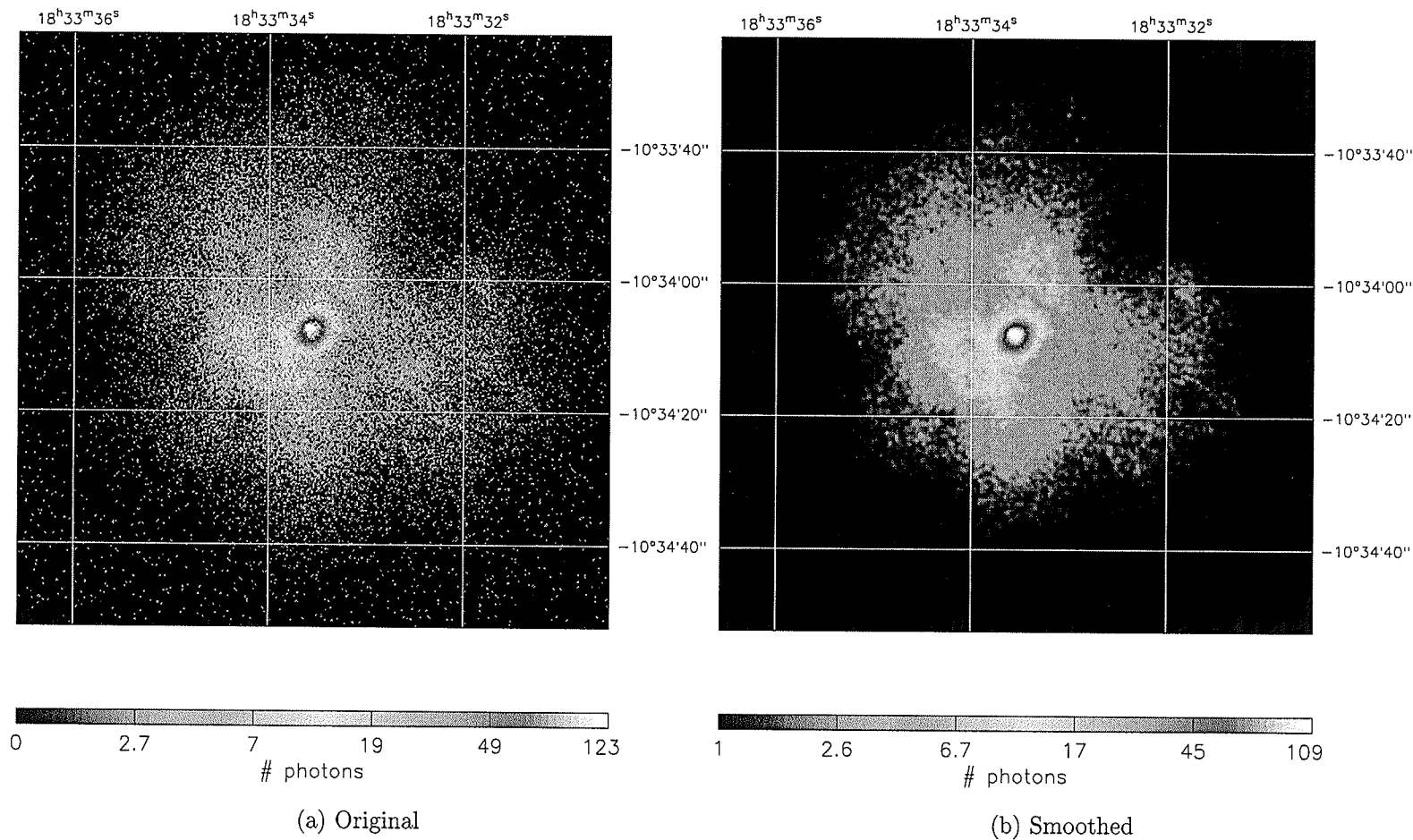


Figure 6.4 - HRC-I combined data of the plerion only. The total exposure time is 278.4 ks and the image is  $90''$  on a side. (same scale as Figure 6.3) (b) is the result of smoothing (a) with a Gaussian of  $\sigma = 0.26''$ . North is up and east is to the left.

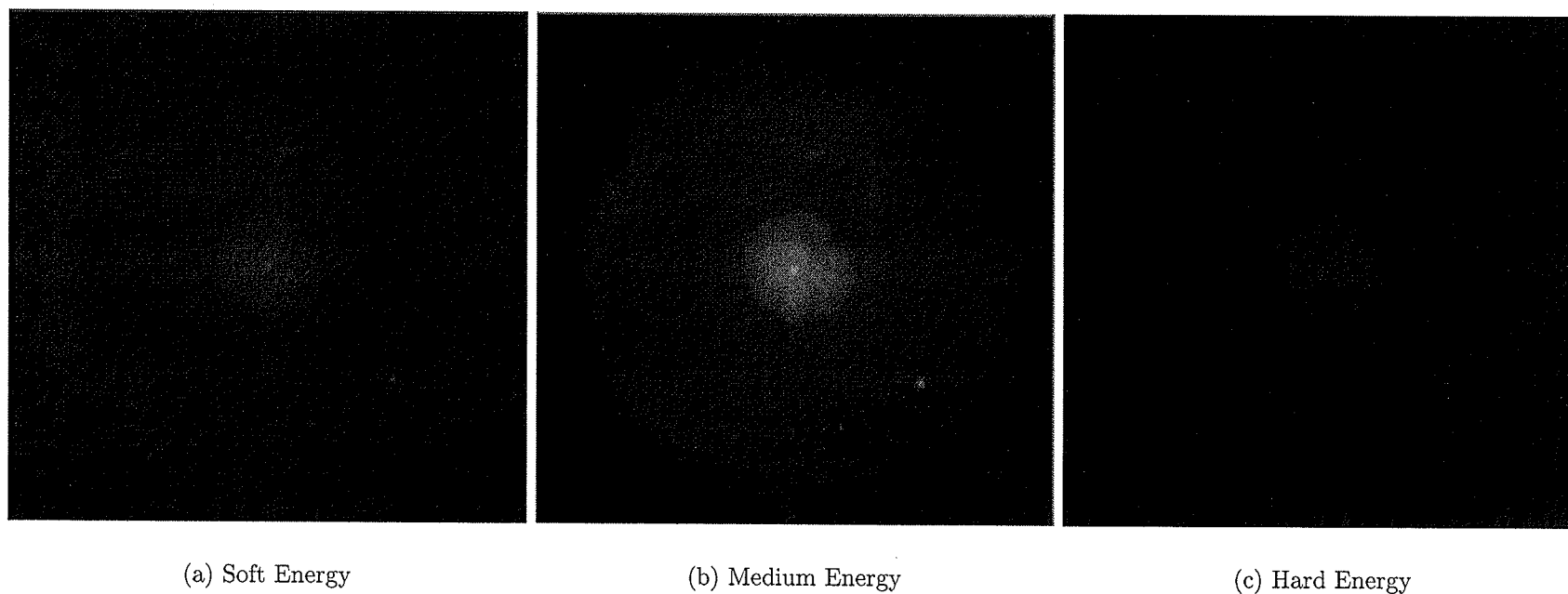


Figure 6.5 - ACIS energy bands. The total exposure time is 578.6 ks and the image is  $377''$  on a side, and smoothed with a Gaussian  $\sigma = 0.5'' - 2.5''$  and a signal-to-noise ratio of 2 - 3. (a) is the soft energy image (0.2-1.5 keV), (b) is the medium energy image (1.5-3.0 keV), and (c) is the hard energy image (3.0-10.0 keV). North is up and east is to the left. The point source in the southwest of the images is the foreground star SS 397.

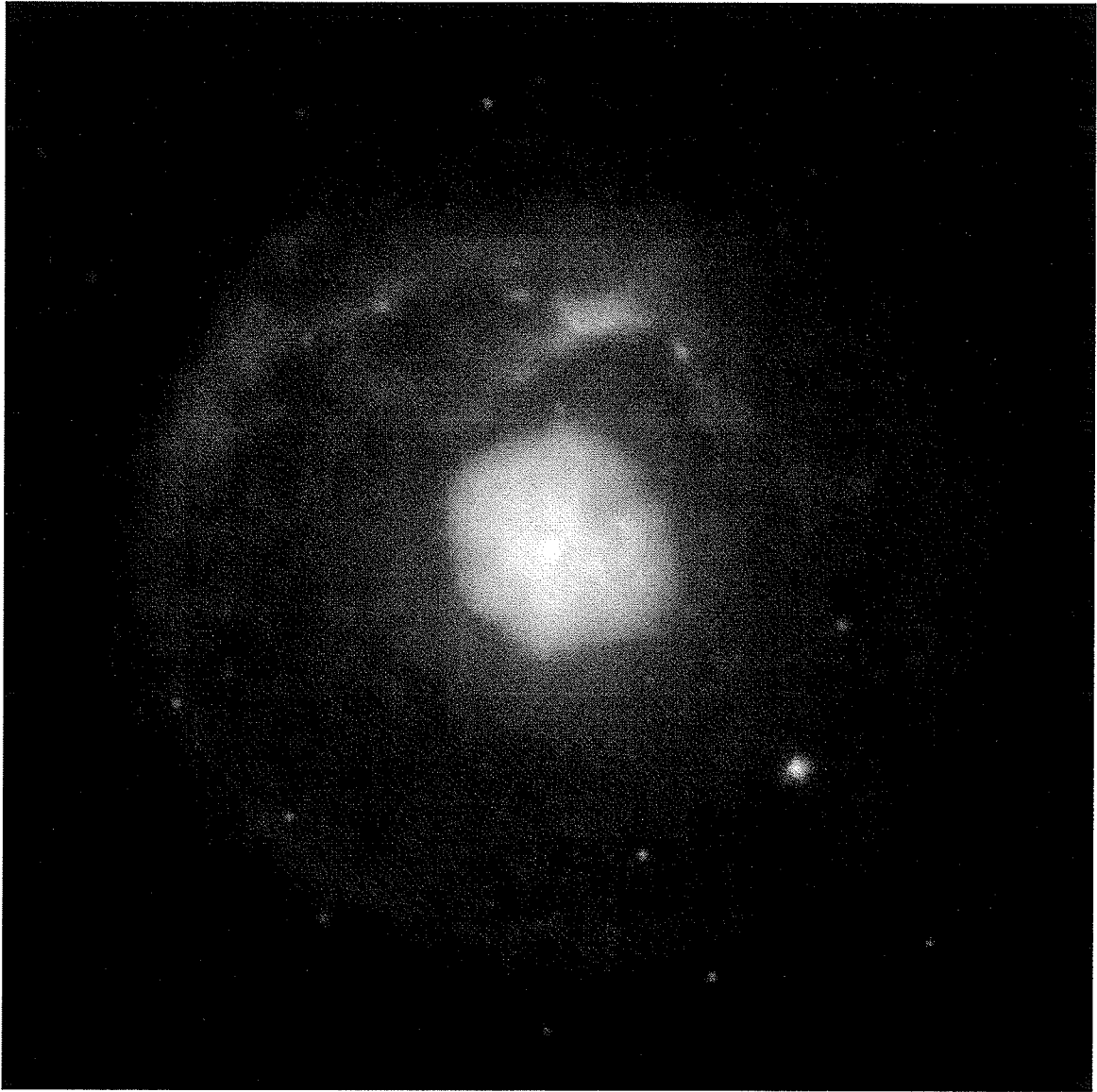


Figure 6.6 - ACIS colour image of G21.5-0.9. The total exposure time is 578.6 ks and the image is centred at  $\alpha(2000) = 18^{\text{h}}33^{\text{m}}33^{\text{s}}.54$ ,  $\delta(2000) = -10^{\circ}34'07''.6$ . Red corresponds to the soft energy image (0.2-1.5 keV), green to the medium energy image (1.5-3.0 keV), and blue to the hard energy image (3.0-10.0 keV). North is up and east is to the left. The point source in the southwest of the image is the foreground star SS 397.

### 6.3 Morphology

The location of the pulsar is  $\alpha(2000) = 18^{\text{h}}33^{\text{m}}33^{\text{s}}.54$ ,  $\delta(2000) = -10^{\circ}34'07''.6$ . The compact region of emission centred on this location has an elliptical shape with a major axis of  $5.3''$  at  $43^{\circ}$  north of west and a minor axis of  $4.4''$ . This location for the pulsar is consistent (within one pixel) with the location of the radio pulsar detected by Camilo et al. ( $\alpha(2000) = 18^{\text{h}}33^{\text{m}}33^{\text{s}}.57$ ,  $\delta(2000) = -10^{\circ}34'07''.5$ ) [14].

The plerion is observed to be brightest to a radius of  $20''$  (orange region in Figure 6.3) and extends to  $\sim 40''$ . There is an obvious indentation in the northwest (north is up and east is to the left in all images) and a reduction in brightness in the southeast, showing the doubled-lobed morphology indicative of precessing jets from the pulsar. Many wisps are visible in the plerion, which may be transient structures and will be investigated in Section 6.5.

The X-ray halo is nearly circular, centred on the pulsar and extending to a radius of  $150''$ . Limb-brightening (the “limb”, blue curve in Figure 6.7) is observed along the east and south at the edge of the halo ( $\sim 125'' - 150''$ ). There are regions of enhanced emission in the north of the remnant (the “knots”). These knots can be looked at as three arcs (Figure 6.7), all originating  $80''$  due north of the pulsar (at  $\alpha(2000) = 18^{\text{h}}33^{\text{m}}34^{\text{s}}$ ,  $\delta(2000) = -10^{\circ}32'51''$ ). The first (red, Figure 6.7) arcs to the west, to the point  $\alpha(2000) = 18^{\text{h}}33^{\text{m}}29^{\text{s}}$ ,  $\delta(2000) = -10^{\circ}33'27''$ . The second (orange, Figure 6.7) and third (green, Figure 6.7) arc to the point  $\alpha(2000) = 18^{\text{h}}33^{\text{m}}42^{\text{s}}$ ,  $\delta(2000) = -10^{\circ}33'27''$  to the east, the second tracing northward through the point  $\alpha(2000) = 18^{\text{h}}33^{\text{m}}36^{\text{s}}$ ,  $\delta(2000) = -10^{\circ}32'32''$  and the third passing southward through

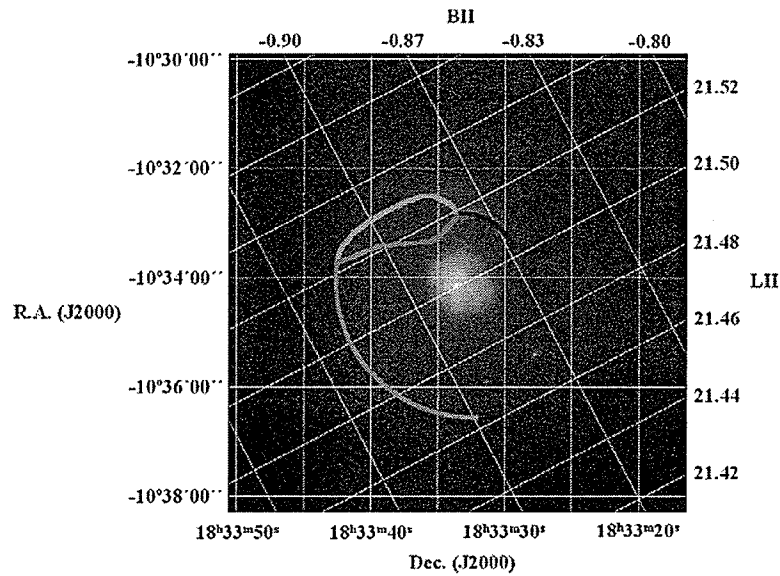


Figure 6.7 - G21.5-0.9 in Galactic coordinates. Equatorial (J2000) coordinates are along the left and bottom (yellow grid). Galactic coordinates are along the right and top (white grid). The northern knots can be viewed as three arcs (red, orange, and green curves). The limb is highlighted with the blue curve.

the point  $\alpha(2000) = 18^{\text{h}}33^{\text{m}}36^{\text{s}}$ ,  $\delta(2000) = -10^{\circ}33'23''$ . These arcs could indicate hindered expansion of the SN ejecta to the north. This could be due to a denser medium to the north of the remnant. Weiler & Sramek [49] note that several groups have described brightening on the side of SNRs closest to the Galactic Plane as controlled by the denser ISM that exists in the direction of the Galactic Plane (the line  $\text{BII} = 0.0$ , Figure 6.7). Since G21.5-0.9 is south of the Galactic Plane (the Galactic Plane is located to the northwest of G21.5-0.9 as plotted in the images in this chapter, perpendicular to a line running through the pulsar at an angle of  $28^{\circ}$  north of west), this is one possible explanation for a denser medium.

## 6.4 Radial Profile

A radial profile was extracted from the 0.2 - 10.0 keV ACIS data using the tools *dmcopy*, *dmextract*, and *dmtcalc*. The point source SS 397 was removed from the data prior to the construction of the radial profile.

A profile of the count rate per unit area, as a function of radius from the remnant centre, is shown in Figure 6.8 (red curve). The PSF (created using the tools *dmextract*, *dmcopy*, *dmstat*, *mkpsf*, and *dmimgcalc*) for a point source at the location of the pulsar is also plotted. The green curve in Figure 6.8 is the profile of a point source, normalized by count rate to match the G21.5-0.9 profile at 0". We can see that the emission at the location of the pulsar is extended with respect to a point source. Using Equations 1.13 and 1.14, we can compute the characteristic scale of the wind termination shock around the pulsar. Using  $B_n \sim 0.3$  mG and  $\dot{E} = 3.37 \times 10^{37}$  erg s<sup>-1</sup> for G21.5-0.9, from Camilo et al. [14], we find  $r_t = 1.58 \times 10^{17}$  cm. Assuming a distance of 5 kpc to G21.5-0.9 (Section 4.4), this corresponds to a radius of 2.1". This agrees with the size of the compact emission observed at the centre of G21.5-0.9. Therefore, we cannot distinguish the wind termination shock from the pulsar emission.

The plerion is observed out to a radius of  $\sim 40''$ , the northern knots are observed at a radius of 70" - 90", and the limb is seen at a radius of 125" - 145". Beyond the limb the surface brightness of the remnant decreases exponentially.

A profile of the surface brightness in each quadrant of the remnant is shown in Figure 6.9. All four profiles show emission from the pulsar to  $\sim 5''$ . The southwest

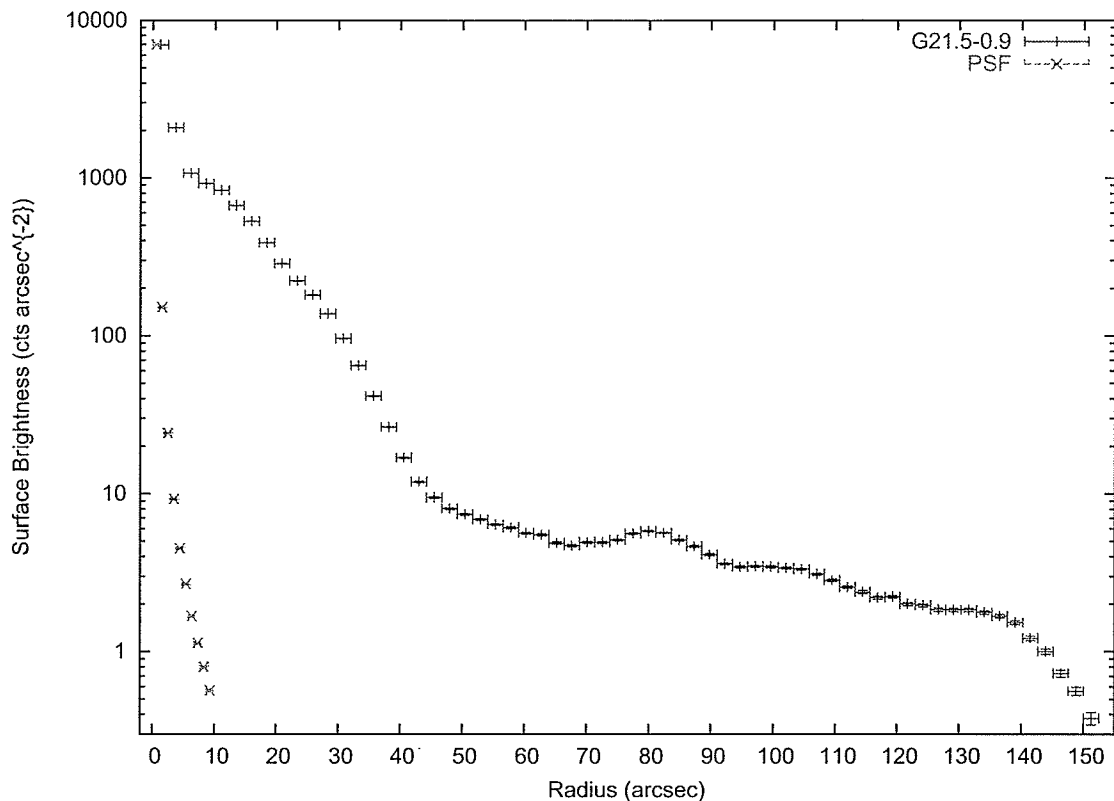


Figure 6.8 - Surface brightness of G21.5-0.9 as a function of radius. The red curve is the observed brightness of the remnant and the green curve is the expected brightness of a point source, normalized to the brightness at the centre of the remnant. The point source (the foreground star SS 397) in the southwest of G21.5-0.9 was removed prior to constructing the profile.

and northeast profiles show a smooth decline in brightness in the plerion from 5'' to 40''. The northwest and southeast profiles show a lower count rate near 20'', due to the indentations in the plerion (double-lobed structure, Figure 6.3). The northwest profile clearly shows the knots at 70'' - 90'', while the northeast profile shows an increased surface brightness over much of the halo due to the knots. The limb is most pronounced in the southeast profile, consistent with the images.

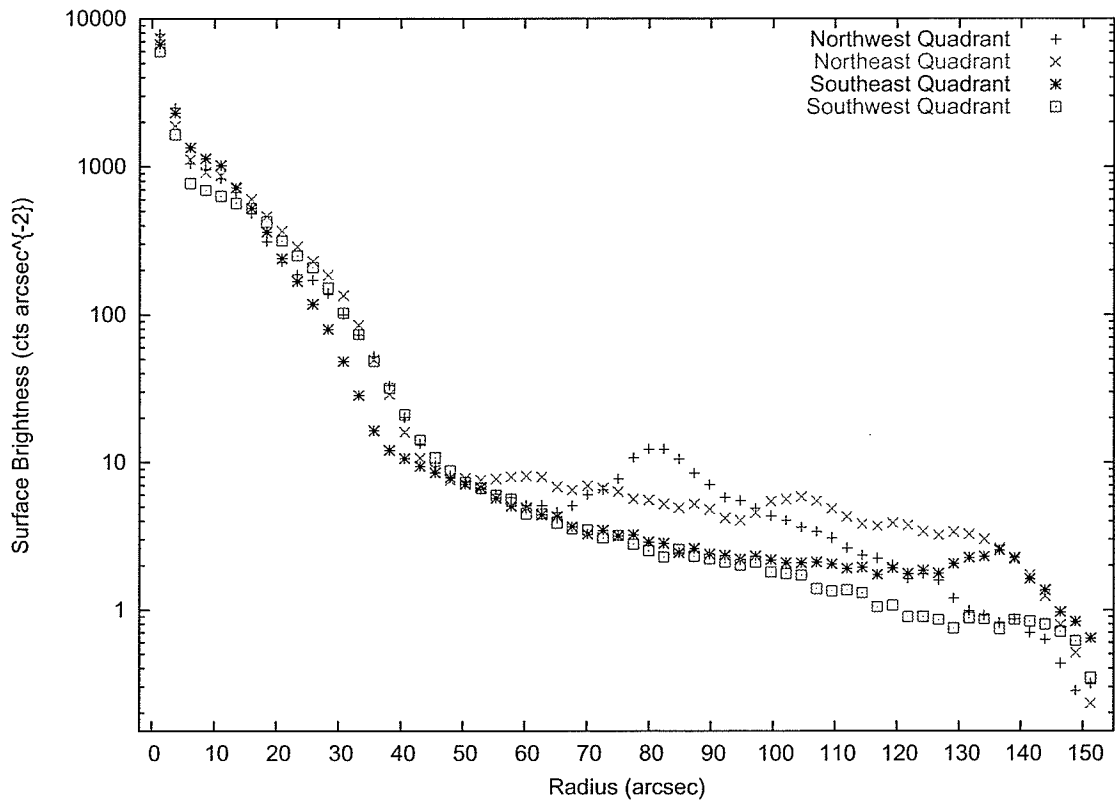


Figure 6.9 - Surface brightness of G21.5-0.9 as a function of radius in each quadrant. The red, green, blue, and magenta curves are the observed brightness of the remnant in the northwest, northeast, southeast, and southwest quadrants, respectively. (counter-clockwise from top right quadrant in Figure 6.1). The point source (the foreground star SS 397) in the southwest of G21.5-0.9 was removed prior to constructing the profiles.

## 6.5 Search for Variability in G21.5-0.9

Variability has been previously observed in the Crab Nebula (Figure 6.10(a)) and the Vela Remnant (Figure 6.10(b)). The Crab Nebula shows wisps moving outward with a velocity  $\sim 0.5c$  (Hester et al. [24]), while the Vela Nebula shows bright compact blobs moving at  $0.3c - 0.6c$  (Pavlov et al. [36]). These remnants are located at approximately 40% and 10%, respectively, of the distance to G21.5-0.9, making changes in their morphology easier to detect than for G21.5-0.9.

Using the distance estimate (adopted in Section 4.4) of  $D = 5 \text{ kpc}$  to G21.5-0.9, we can estimate the angle through which features moving at  $0.5c$  would be expected to travel. The linear distance a feature moving at  $0.5c$  would cover in  $t = 1 \text{ yr}$  (assuming a constant speed) is

$$d = vt = 0.153 \text{ pc}. \quad (6.1)$$

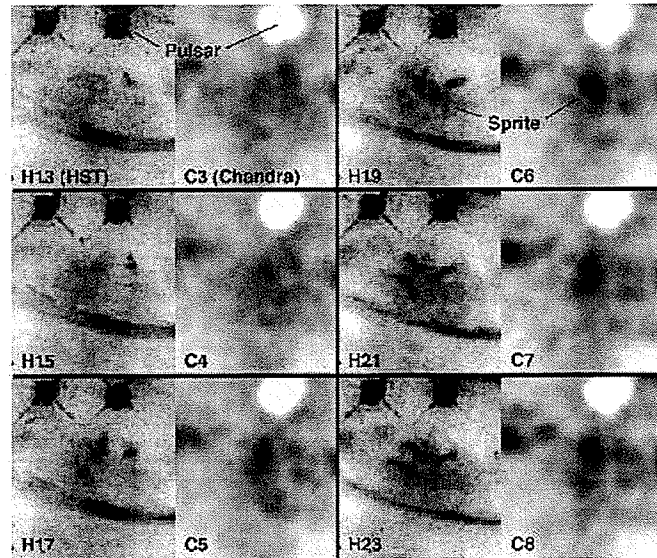
Using the small angle approximation, the feature would move

$$\theta \simeq \frac{d}{D} = 6.32'' \text{ yr}^{-1}. \quad (6.2)$$

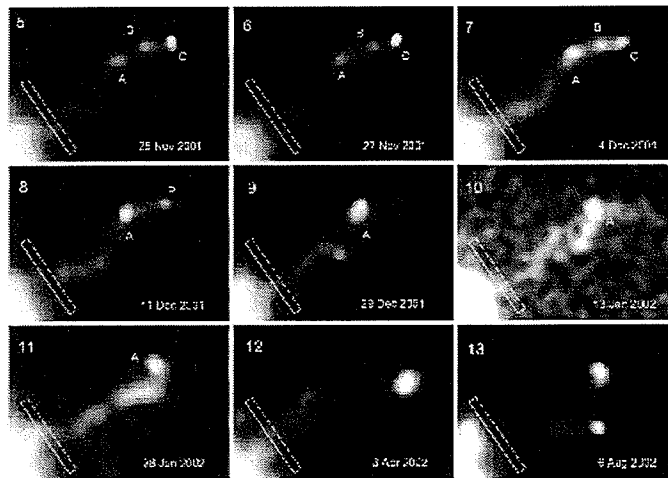
Since the spatial resolution of *Chandra* is  $0.5''$  (Section 3.2.1) and we have observations obtained over a period of 6 years, we can search for variability in G21.5-0.9.

Figures 6.11 (ACIS) and 6.12 (HRC-I) shows the evolution of G21.5-0.9 over the life of *Chandra* (from Aug 1999 to Feb 2006). Observations from each observing date were combined, smoothed with a Gaussian of  $\sigma = 1''$  and normalized to an effective exposure time of 20 ks.

By subtracting images in Figures 6.11 and 6.12, we can observe changes in the morphology of G21.5-0.9 between observing dates. One example is shown in Fig-



(a) Crab Nebula



(b) Vela Remnant

Figure 6.10 - Variability in remnants containing pulsars. (a) shows Hubble Space Telescope (labelled “H”) and *Chandra* (labelled “C”) images of the jet in the Crab Nebula, with 44 days between images. *Credit: Hester et al., 2002.* (b) shows *Chandra* images of the outer jet in the Vela Nebula, with moving bright knots A, B, and C labelled. *Credit: Pavlov et al., 2003.*

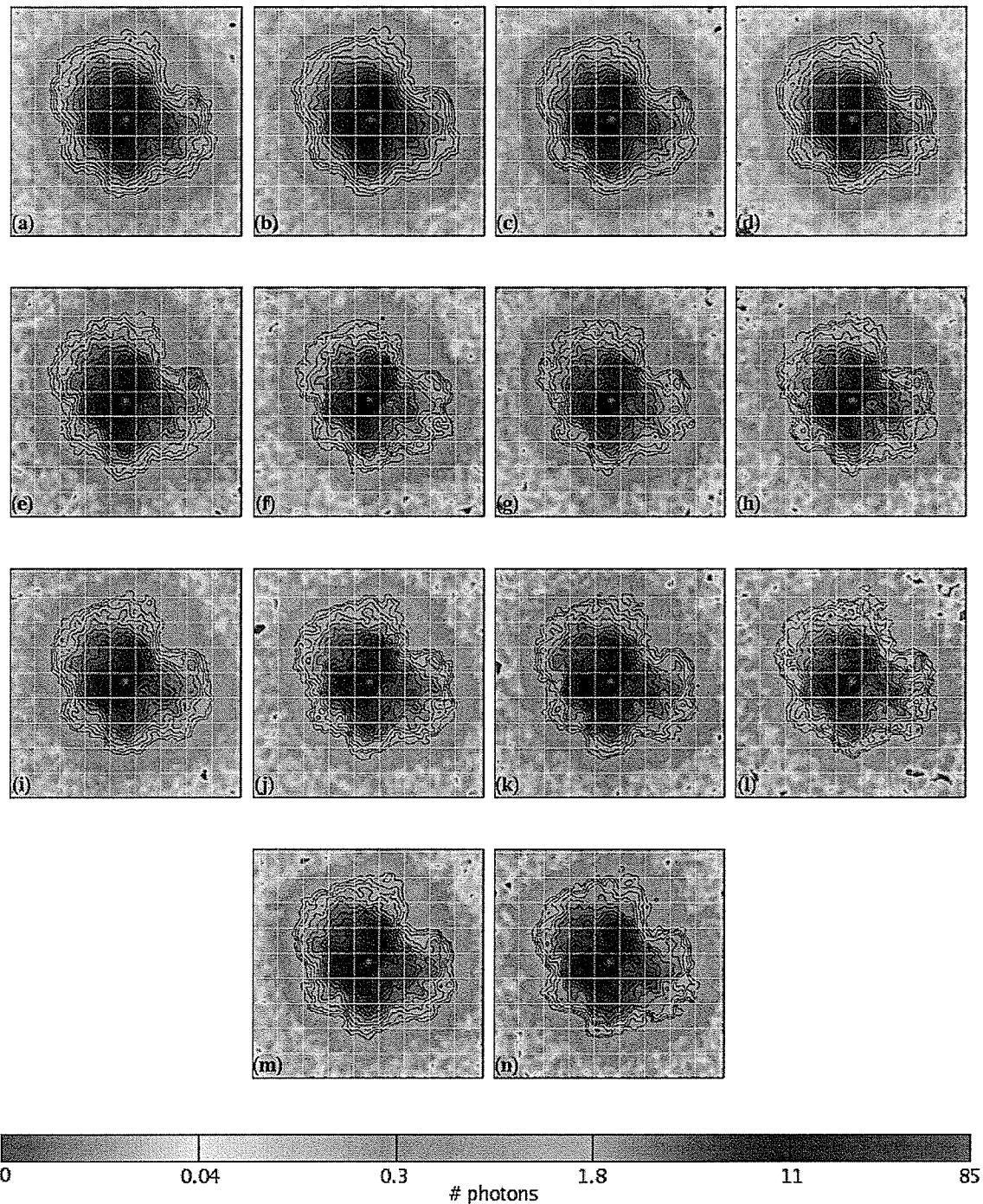


Figure 6.11 - Combined ACIS images of G21.5-0.9 for each observing date. All images are normalized to an effective exposure of 20 ks. The colourbar used is a logarithmic scale and identical in all images. Contours are at 1, 1.26, 1.60, 2.02, 2.55, 3.22, 4.07, 5.14, 6.49, 8.20, 10.36, 13.09, 16.54, 20.90, 26.40, 33.36, 42.15, 53.25, 67.28, and 85 photons. Each image is  $90''$  on a side. (a) 1999-08 (b) 1999-11 (c) 2000-05 (d) 2000-07 (e) 2000-09 (f) 2001-03 (g) 2001-07 (h) 2002-09 (i) 2003-05 (j) 2003-11 (k) 2004-03 (l) 2004-10 (m) 2005-02 (n) 2006-02

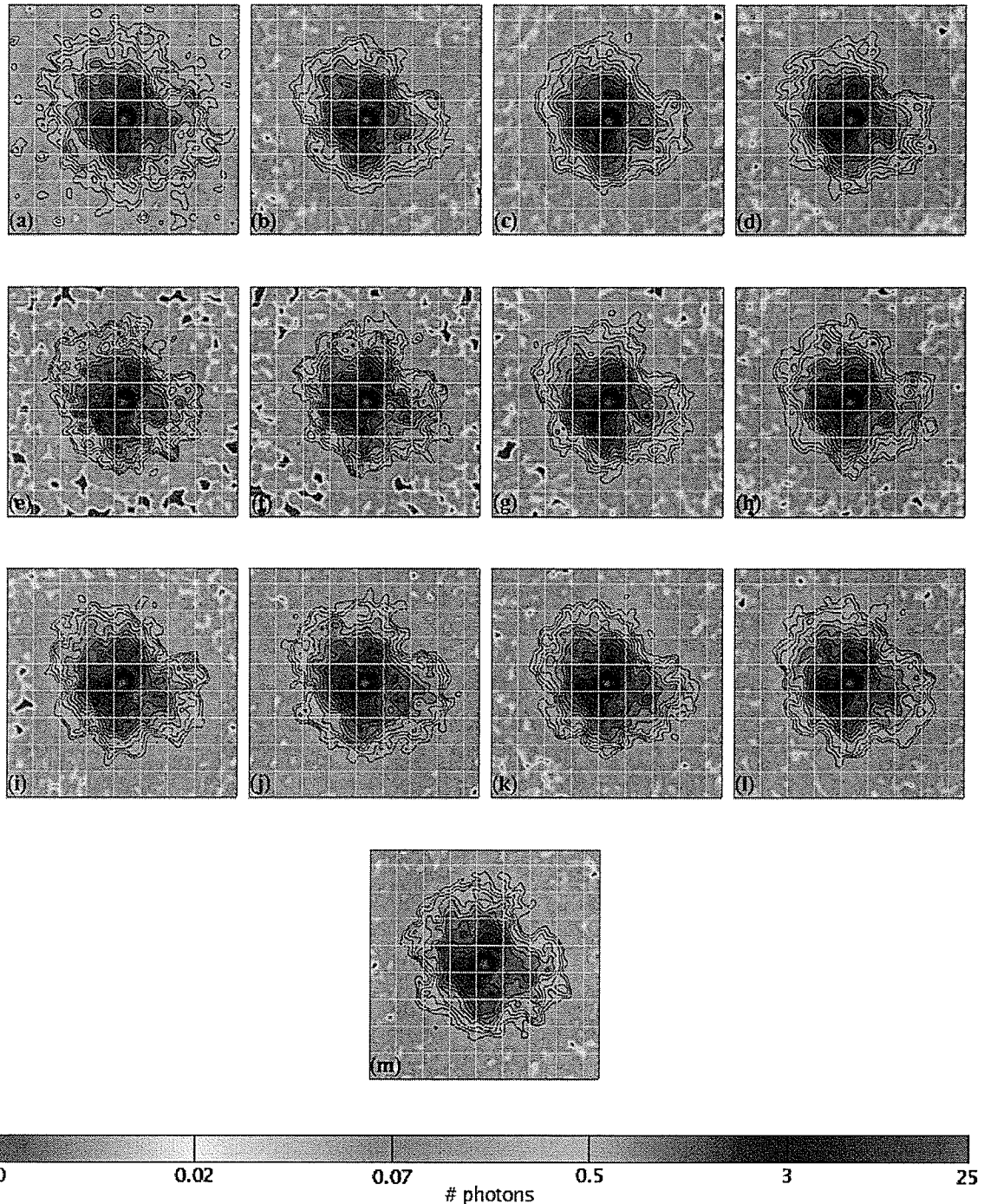


Figure 6.12 - Combined HRC-I images of G21.5-0.9 for each observing date. All images are normalized to an effective exposure of 20 ks. The colourbar used is a logarithmic scale and identical in all images. Contours are at 0.3, 0.38, 0.48, 0.60, 0.76, 0.96, 1.21, 1.53, 1.93, 2.43, 3.08, 3.88, 4.90, 6.19, 7.81, 9.85, 12.44, 15.69, 19.81, and 25 photons. Each image is  $90''$  on a side. (a) 1999-09 (b) 1999-10 (c) 2000-02 (d) 2000-09 (e) 2001-03 (f) 2001-07 (g) 2002-03 (h) 2002-07 (i) 2003-05 (j) 2003-11 (k) 2004-03 (l) 2005-02 (m) 2006-02

ure 6.13. The normalized ACIS image of Feb 2005 (Figure 6.11(m)) was subtracted from the normalized ACIS image of Feb 2006 (Figure 6.11(n)). The bright emission from the pulsar (magenta in Figure 6.11) was removed prior to the subtraction in order to enhance the features in the plerion. The colours in Figure 6.13 are on a linear scale (black = -1.9 cts/pixel, green = 0 cts/pixel, white = +2.1 cts/pixel). The blue and black regions are regions which had a lower count rate in Feb 2006 than in Feb 2005. The white and red regions are regions which had a higher count rate in Feb 2006 than in Feb 2005. A white-black pair is therefore a possible knot in motion. The most clearly defined pair lies to the north (top in Figure 6.13) of the pulsar location. A knot in motion that does not change in brightness between observations must leave a deficiency at its original location equal in magnitude to the excess observed at its final location. The white spot has a count rate of +2.1 counts per pixel and the black spot has a count rate of -1.9 counts per pixel. The knot has moved a distance of 12 pixels ( $\sim 0.14$  pc) in one year, corresponding to a speed of  $\sim 0.5c$ , where  $c$  is the speed of light. This is consistent with the results observed for the Crab and Vela Nebulae [24, 36].

Other possible knots in motion can be seen by comparing consecutive images in Figures 6.11 and 6.12. The highest degree of variability occurs within  $20''$  of the pulsar to the northwest and southeast, and between  $20''$  and  $40''$  in the southwest of the plerion. Figures 6.12(j), 6.12(k), and 6.12(l) show a knot travelling ( $\sim 3$  pixels between images) in the northwest direction, located  $\sim 20''$  west-southwest of the pulsar.

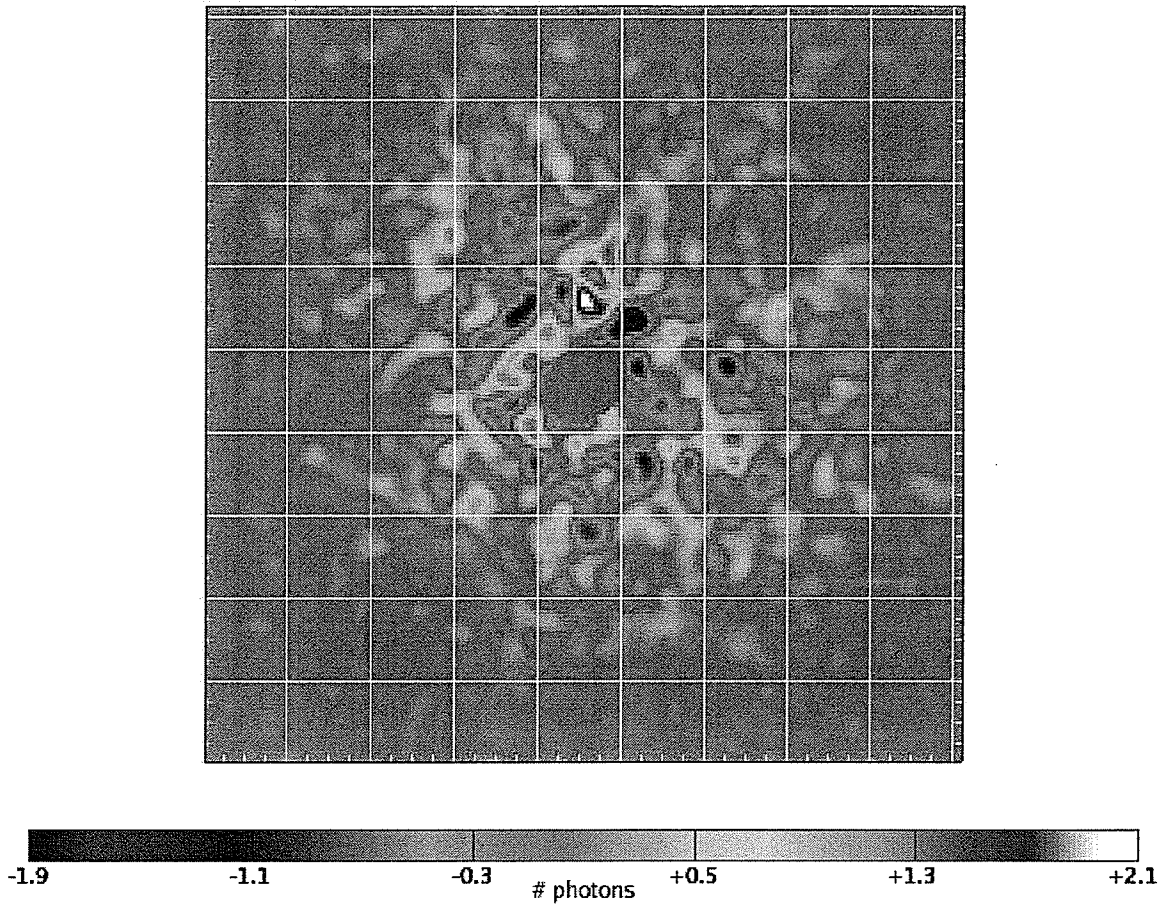


Figure 6.13 - An example of motion of knots in G21.5-0.9. Using the combined ACIS images (Figure 6.11), the Feb 2005 image was subtracted from the Feb 2006 image. A positive value indicates a pixel which had a higher count rate in Feb 2006 than in Feb 2005. A negative value indicates a pixel which had a lower count rate in Feb 2006 than in 2005.

# CHAPTER 7

## A CHANDRA STUDY OF G21.5-0.9: SPECTROSCOPY

A “cleaned” evt2 file was created for each observation, as described in Chapter 5. A merged event file does not contain all of the observation-specific data that is required for use in a spectroscopic analysis and therefore the individual evt2 files were the starting point for the spectroscopic analysis. The  $-100^{\circ}\text{C}$  data cannot be corrected for CTI (Section 5.2.2) and was therefore omitted from the spectral analysis. Using the cleaned event file for a single observation we can plot the energy associated with each photon in the list, filter for events in a particular region, and create a spectrum (number of photons detected at each energy) for a particular feature of the remnant.

Section 7.1 describes how the spectra were created using the CIAO software package. The scripts used to create the spectra are presented in Appendix A.3 (CIAO CTI correction) and A.4 (Penn State CTI correction). The following sections describe the results for the pulsar, the entire plerion, the entire X-ray halo, the northern knots, the eastern limb-brightening, and concentric annuli centred on the pulsar.

## 7.1 Spectra Creation

For each region, the first step in creating spectra was creating a region file using *SAOImage DS9*<sup>1</sup> to select the region of interest. Spectra were extracted from these regions using the procedure outlined below. As well, background regions were selected in *DS9*. Since the SNR G21.5-0.9 covers a large portion of the CCDs, the background regions were chosen to be small circles outside the remnant, on the same CCD as the data.

The CIAO tool *dmcopy* was used to produce an event file containing only events which fell into the selected region during the observation.

Spectra were extracted from the cleaned event file for each observation using the CIAO tool *dmextract*, which accepts an event file and creates a spectrum using the observed counts in that file. By inputting the event files created after filtering the data by region, spectra for individual regions were obtained.

Since the regions used were extended regions (as opposed to point sources), it was necessary to create weighted spectra. The CIAO tool *dmcopy* was used to create WMAPS for each region, which are files containing an image of the field in detector coordinates. The energy range provided to *dmcopy* determines the weighting type that will be used. The range 0.5 - 2.0 keV count-weights the averaging of the responses, whereas the range 2.0 - 10.0 keV uses area weighting since the background dominates at higher energies. Count-weighting was used for all spectral analysis performed here.

The WMAPs are used by the tool *mkwarf* to create weighted ancillary response

---

<sup>1</sup>SAOImage DS9 version 3.0b9, developed by Smithsonian Astrophysical Observatory, <http://hea-www.harvard.edu/RD/ds9/>

files (ARFs) which are files that give information about the effective area and quantum efficiency of the detector, as a function of energy averaged over time. ARFs are used during spectral analysis, where the input spectrum is multiplied by the ARF. This produces the count distribution that would have been obtained by a detector with perfect energy resolution.

Redistribution matrix files (RMFs) are also necessary to perform spectral analysis. These files map energy space into detector pulse height space. Since the detectors are imperfect, the mapping results in the observed counts spreading due to the detector resolution.

For the observations that were CTI corrected using the Penn State CTI corrector (see Section 3.5 for a description of CTI, Section 5.2.2 for a description of the observations used), RMF files were provided with the corrector. For the observations that were CTI corrected with *acis\_process\_events*, the CIAO tool *mkacisrmf* was used to create weighted RMF files.

The spectra were binned using the FTOOLS *grppha* to improve the signal-to-noise ratio. The minimum number of counts per bin for the various regions used in this thesis are shown in Tables 7.2 and 7.3.

The regions used in the following spectral analysis are listed in Table 7.1 and shown in Figure 7.1. The spectral models used in the following chapter are described in detail in Appendix B. All models contain a component which accounts for absorption along the line of sight. A power-law model (Section 2.2) was used to search for synchrotron emission from high energy electrons in a magnetic field. A model describing blackbody emission from a star (Section 2.3) was used to study the compact emission in the

Table 7.1. Regions studied.

Region	Background Subtracted Count Rate <sup>a</sup> (cts/s)	Total Exposure Time (ks)	Area (arcmin <sup>2</sup> )
Compact Source	$0.38 \pm 0.06$	480.2	0.014
PWN (4''-40'')	$2.18 \pm 0.23$	480.2	1.382
PWN (0''-40'')	$2.57 \pm 0.29$	480.2	1.396
Halo (40''-150'')	$(5.30 \pm 0.59) \times 10^{-1}$	255.6	18.217
Northern Knots	$(1.50 \pm 0.15) \times 10^{-1}$	360.6	2.555
Eastern Limb	$(5.03 \pm 0.85) \times 10^{-2}$	315.6	2.260

<sup>a</sup>in the energy range 0.5 - 8.0 keV

centre of the remnant and search for emission from the neutron star directly. A *pshock* model (Appendix B.5) was used to search for thermal emission from shock-heated ejecta or interstellar matter. Thermal bremsstrahlung emission is due to a hot diffuse gas (Section 2.1). A *mekal* model (bremsstrahlung continuum + line emission, Appendix B.6) was also used to search for thermal emission from G21.5-0.9. In addition, Gaussian lines (Appendix B.7) were added on top of models describing the continuum to search for emission from metals, indicating the presence of SN ejecta.

All spectral fitting presented here was performed with *XSPEC*<sup>2</sup> version 11.2.0. All spectra were fit simultaneously, grouped according to CCD temperature and CCD ID (I0/-110°C, I1/-110°C, I2/-110°C, I3/-110°C, S2/-110°C, S3/-110°C, I1/-120°C, I3/-120°C, S2/-120°C, S3/-120°C). A multiplicative constant was included in all fits and allowed to vary among the datagroups to account for different responses in different chips. All other parameters were tied (no variation allowed between individual

<sup>2</sup>X-ray Spectral Fitting Package (XSPEC), <http://xspec.gsfc.nasa.gov/>

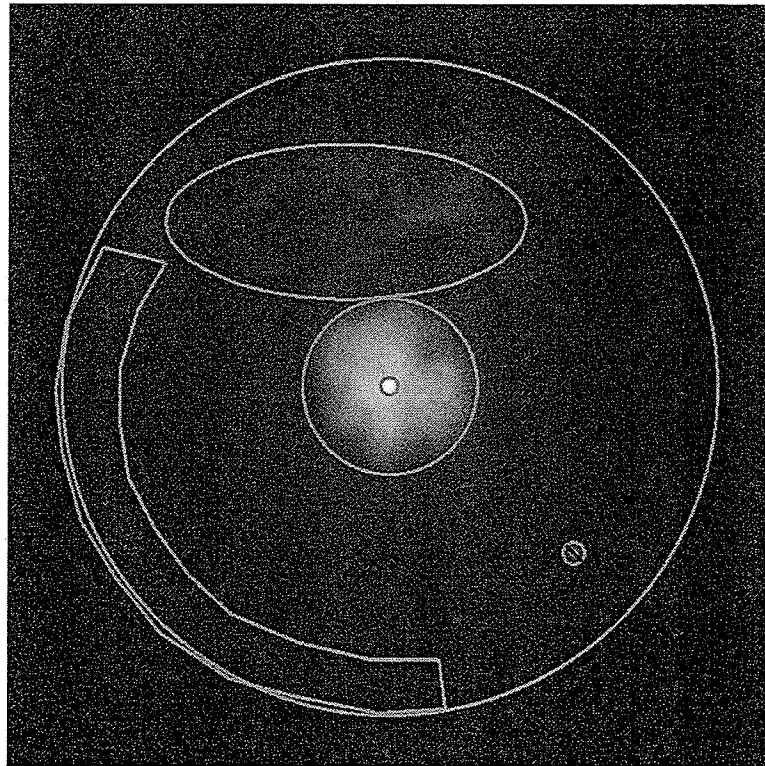


Figure 7.1 - The regions used in the spectral analysis of G21.5-0.9. The concentric circles are located at  $4''$ ,  $40''$ , and  $150''$ . The northern knots and eastern limb are also highlighted. The point source SS 397 was excluded from the data prior to extracting spectra for the halo.

spectra). All errors in this chapter are reported to the 90% confidence level.

## 7.2 PSR J1833-1034

A circular region with  $4''$  radius (as in Section 3.8, a  $4''$  radius contains  $>90\%$  of the energy from a point source (exact % depends on energy)), centred at  $\alpha(2000) = 18^{\text{h}}33^{\text{m}}33^{\text{s}}.54$ ,  $\delta(2000) = -10^{\circ}34'07''.6$ , was fit with an absorbed power-law ( $\text{const} * \text{wabs} * \text{power}$ , see Appendix B). The spectra were each grouped to have a minimum of 50 counts per bin. The best fit using a power-law model had a column density of

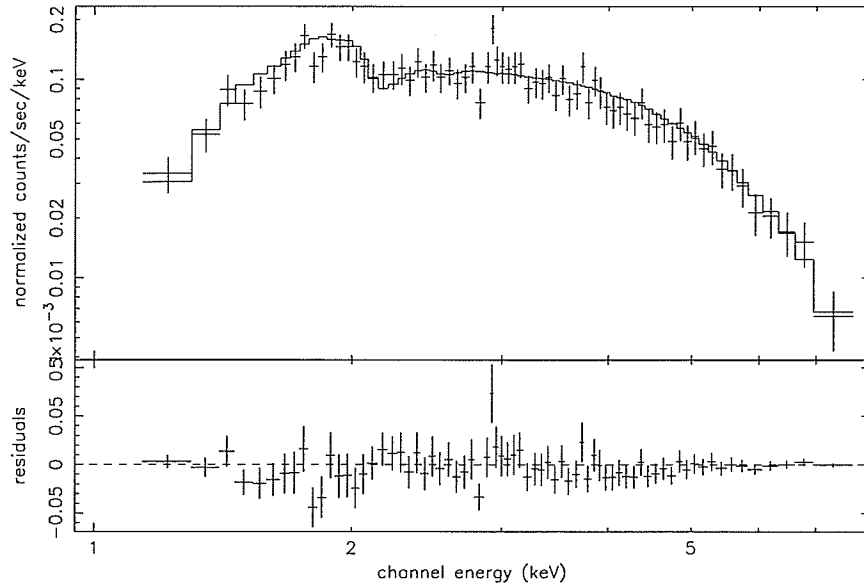


Figure 7.2 - A sample spectrum (obsID 5166) of the pulsar PSR J1833-1034, showing the data (crosses), model (solid line), and residuals (bottom panel) of the fit to an absorbed power-law (*const\*wabs\*power* in *XSPEC*).

$N_{\text{H}} = 2.54_{-0.04}^{+0.05} \times 10^{22}$  atoms  $\text{cm}^{-2}$ , a photon index of  $\Gamma = 1.63_{-0.03}^{+0.03}$ ,  $\nu = 3192$ , and  $\chi^2_{\nu} = 0.762$  (see Table 7.2 for a complete list of parameters, and Figure 7.2 for a sample spectrum). Freezing  $N_{\text{H}}$  to the best fit value obtained for the plerion ( $N_{\text{H}} = 2.33 \times 10^{22}$  atoms  $\text{cm}^{-2}$ , Section 7.3), the photon index was found to decrease slightly to  $\Gamma = 1.51_{-0.02}^{+0.02}$  ( $\nu = 3193$ ,  $\chi^2_{\nu} = 0.777$ ).

Fitting with a blackbody (*const\*wabs\*bbbody*, see Appendix B) gives a temperature of  $kT = 1.21$  keV =  $1.4 \times 10^7$  K ( $kT = 0.94$  keV =  $1.1 \times 10^7$  K if  $N_{\text{H}}$  is frozen to  $2.33 \times 10^{22}$  atoms  $\text{cm}^{-2}$ ),  $\chi^2_{\nu} = 0.951$  (1.82), a flux (0.5 - 8.0 keV) of  $6.73 \times 10^{-12}$  erg  $\text{cm}^{-2}$   $\text{s}^{-1}$  ( $5.97 \times 10^{-12}$  erg  $\text{cm}^{-2}$   $\text{s}^{-1}$ ), and an unabsorbed flux of  $7.9 \times 10^{-12}$  erg  $\text{cm}^{-2}$   $\text{s}^{-1}$  ( $8.9 \times 10^{-12}$  erg  $\text{cm}^{-2}$   $\text{s}^{-1}$ ). The unabsorbed flux,  $l_{\text{unabs}}$ , can be converted to luminosity with the formula  $L = 4\pi r^2 l_{\text{unabs}}$ , where  $r$  is the distance to the neutron star. By using the luminosity of a blackbody,  $L = 4\pi\sigma R^2 T^4$  ( $R$  is

the radius of the star,  $\sigma = 5.670 \times 10^{-5} \text{ erg cm}^{-2} \text{ s}^{-1} \text{ deg}^{-4}$ ), we can derive the radius of the neutron star. The radius is found to be  $R = \sqrt{\frac{r^2 L_{unabs}}{\sigma T^4}} = 0.29 \text{ km}$  for a temperature of 1.21 keV, and  $R = 0.51 \text{ km}$  for a temperature of 0.94 keV. This is unreasonably small for the size of a neutron star and we may instead be observing emission from a “hot spot” on the surface of the star. However, since the power-law produces a better fit (lower  $\chi_\nu^2$ ) to the spectrum of the pulsar than the blackbody model, we are most likely observing X-rays produced in the magnetosphere around the neutron star (Section 2.4).

### 7.3 Plerion ( $r = 0'' - 40''$ )

The overall spectrum from the inner  $40''$  of G21.5-0.9 was fit with a power-law, with a photon index of  $\Gamma = 1.82_{-0.01}^{+0.01}$ , a column density of  $N_{\text{H}} = 2.34_{-0.01}^{+0.02} \times 10^{22} \text{ atoms cm}^{-2}$ ,  $\nu = 9202$  degrees of freedom,  $\chi_\nu^2 = 1.02$ , a flux (0.5 - 8.0 keV) of  $4.7 \times 10^{-11} \text{ erg cm}^{-2} \text{ s}^{-1}$ , and an unabsorbed flux (0.5 - 8.0 keV) of  $9.4 \times 10^{-11} \text{ erg cm}^{-2} \text{ s}^{-1}$ . A sample spectrum from a single observation is shown in Figure 7.3.

Ignoring the emission from the pulsar ( $0'' - 4''$ ), the power-law has a photon index of  $\Gamma = 1.86_{-0.01}^{+0.01}$ , with  $N_{\text{H}} = 2.33_{-0.01}^{+0.02} \times 10^{22} \text{ atoms cm}^{-2}$ ,  $\nu = 8060$ , and  $\chi_\nu^2 = 1.01$ . The flux was found to be  $3.9 \times 10^{-11} \text{ erg cm}^{-2} \text{ s}^{-1}$ , and the unabsorbed flux was  $8.1 \times 10^{-11} \text{ erg cm}^{-2} \text{ s}^{-1}$ . The spectrum of a single observation is shown in Figure 7.4.

There is no evidence of thermal emission from the plerion. Since the plerion is well fit by a power-law, these results are consistent with synchrotron radiation from high energy electrons (Section 2.2).

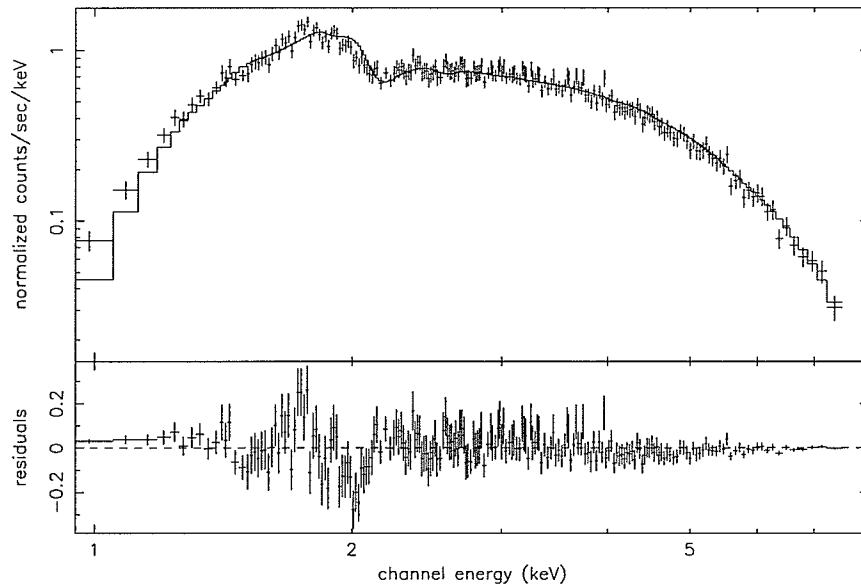


Figure 7.3 - A sample spectrum (obsID 5166) of the plerion ( $r = 0'' - 40''$ ), showing the data (crosses), model (solid line), and residuals (bottom panel) of the fit to an absorbed power-law ( $const*wabs*power$  in *XSPEC*).

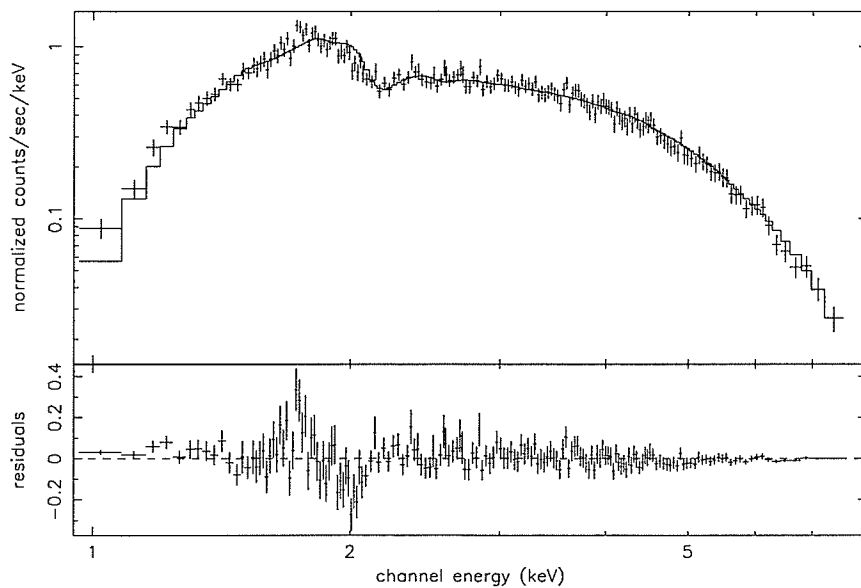


Figure 7.4 - A sample spectrum (obsID 5166) of the plerion ( $r = 4'' - 40''$ ), showing the data (crosses), model (solid line), and residuals (bottom panel) of the fit to an absorbed power-law ( $const*wabs*power$  in *XSPEC*).

The variations in the spectrum of the plerion as a function of radius from the pulsar are looked at in detail in Section 7.8.

The hydrogen column density of  $N_{\text{H}} = 2.33 \times 10^{22} \text{ cm}^{-2}$  will be adopted as the overall column density of G21.5-0.9, and will be used in the following sections.

Using Equation 4.1 and the luminosity of the pulsar + plerion in the energy range 0.2 - 4.0 keV ( $(2.8 \pm 0.2) \times 10^{35} \text{ erg s}^{-1}$ ), an estimate of the spin-down energy loss is found to be  $\dot{E} = (2.8 \pm 0.3) \times 10^{37} \text{ erg s}^{-1}$ , comparable to the pulsar observations of Camilo et al. [14] and Gupta et al. [23].

## 7.4 X-ray Halo ( $r = 40'' - 150''$ )

The entire X-ray halo of G21.5-0.9 was fit with a power-law with a photon index of  $\Gamma = 2.06_{-0.09}^{+0.08}$ , a column density of  $N_{\text{H}} = 1.68_{-0.09}^{+0.10} \times 10^{22} \text{ atoms cm}^{-2}$ ,  $\nu = 1455$ , and  $\chi_{\nu}^2 = 0.372$  (Figure 7.5). Freezing the column density to the best-fit value obtained from the plerion ( $N_{\text{H}} = 2.33 \times 10^{22} \text{ atoms cm}^{-2}$ ), we find that  $\Gamma = 2.55_{-0.04}^{+0.05}$  ( $\nu = 1456$ ,  $\chi_{\nu}^2 = 0.444$ ), which is consistent with the radial profile observed in Section 7.8. The fit is improved by the addition of a thermal *mekal* component (Appendix B) with a temperature of  $kT = 0.20_{-0.06}^{+0.04} \text{ keV} = 2.3_{-0.7}^{+0.5} \times 10^6 \text{ K}$  ( $\nu = 1454$ ,  $\chi_{\nu}^2 = 0.381$ ), or by the addition of a thermal *pshock* component with a temperature of  $kT = 0.22_{-0.04}^{+0.04} \text{ keV}$  and an ionization timescale of  $n_e t = 3.3_{-2.3}^{+12.8} \times 10^8 \text{ s cm}^{-3}$  ( $\nu=1453$ ,  $\chi_{\nu}^2=0.375$ ).

Searching for thermal emission from shock-heated ejecta or interstellar matter using the *pshock* model alone (Appendix B) results in a temperature that is unrealistically high ( $kT = 4.96_{-0.46}^{+0.54} \text{ keV} = 5.8_{-0.5}^{+0.6} \times 10^7 \text{ K}$ ) and an ionization timescale that

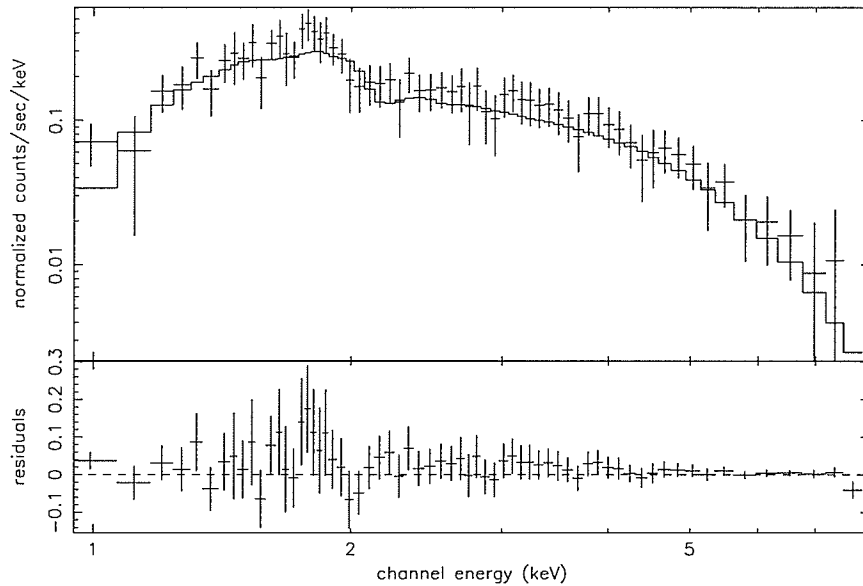


Figure 7.5 - A sample spectrum (obsID 5166) of the X-ray halo ( $r = 40'' - 150''$ ), showing the data (crosses), model (solid line), and residuals (bottom panel) of the fit to an absorbed power-law ( $const * wabs * power$  in *XSPEC*).

is too low ( $n_e t = 6.0_{-5.0}^{+3.9} \times 10^8 \text{ s cm}^{-3}$ ).

This section looked at the overall spectrum of the halo. It is unlikely that a single model will fit the entire halo well since it is composed of bright knots, the limb, and a diffuse halo. Therefore, Sections 7.5 and 7.6 will concentrate on the spectrum of the knots and the limb, respectively.

## 7.5 Northern Knots

Fitting an absorbed power-law to the knots produces an artificially low hydrogen column density ( $N_{\text{H}} = 1.73_{-0.06}^{+0.06} \times 10^{22} \text{ atoms cm}^{-2}$ ) with  $\chi^2_{\nu} = 0.775$  ( $\nu = 1063$ ). Freezing  $N_{\text{H}}$  to the best-fit value of the plerion ( $2.33 \times 10^{22} \text{ atoms cm}^{-2}$ ) gives a photon index of  $\Gamma = 2.48_{-0.03}^{+0.02}$ , an unabsorbed flux of  $6.2 \times 10^{-12} \text{ erg cm}^{-2} \text{ s}^{-1}$ , and

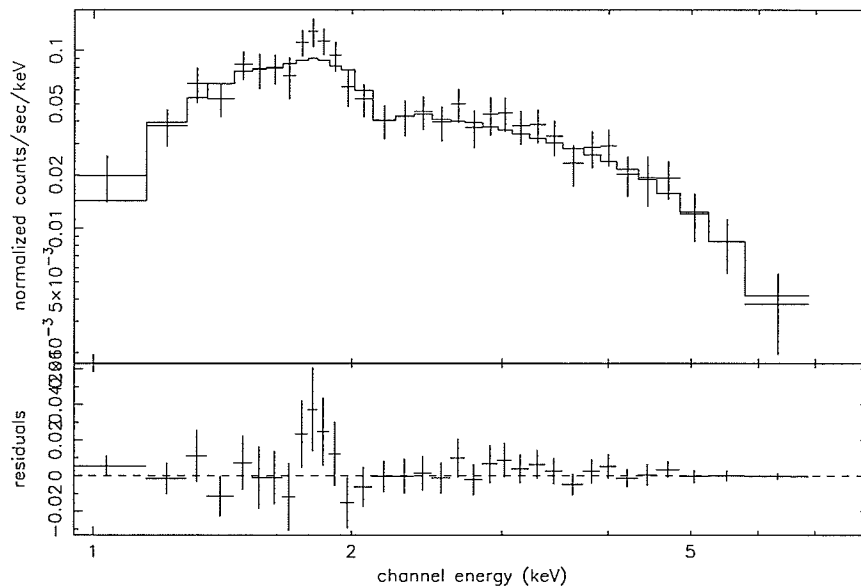


Figure 7.6 - A sample spectrum (obsID 5166) of the northern knots, showing the data (crosses), model (solid line), and residuals (bottom panel) of the fit to an absorbed power-law ( $const*wabs*power$  in *XSPEC*).

an estimated X-ray luminosity (0.5 - 8.0 keV) of  $1.9 \times 10^{34}$  erg  $s^{-1}$  ( $\chi^2_\nu = 0.972$ ,  $\nu = 1064$ ) for the knots. Excess emission is visible in the spectrum of the knots near 1.4, 1.7, 2.3, and 2.7 keV (Figure 7.6), indicating the presence of magnesium, silicon, and sulfur in the knots (element emission lines are known to occur at 1.25 (Mg), 1.74 (Si), and 2.31 (S) keV). Adding Gaussian distributions on top of the power-law ( $const*wabs*(power+gauss)$ , Appendix B) at 1.4, 1.7, 2.3, and 2.7 keV produced F-test probabilities (the probability that an incorrect model will produce the same quality of fit) of  $\sim 3 \times 10^{-7}$ ,  $\sim 3 \times 10^{-3}$ ,  $\sim 3 \times 10^{-7}$ , and  $\sim 5 \times 10^{-6}$  respectively, indicating that the addition of the Gaussians significantly improves the fit. Further, the excess emission in the residuals of Figure 7.6 are evidence of thermal emission from the knots.

The *pshock* model (Appendix B) was used to search for thermal emission that may

be due to shock-heated ejecta or interstellar matter. As shown in Table 7.3, the *pshock* model provides an adequate fit ( $\chi^2_\nu = 0.786$ ,  $\nu = 1062$ ); however with a lower column density, an unrealistically high temperature and a low ionization timescale. Fitting a two component model (*power+pshock*) to the knots, a good fit is also obtained with  $N_H = 2.45^{+0.36}_{-0.25} \times 10^{22}$  atoms  $\text{cm}^{-2}$  (which is consistent with  $N_H$  towards the central plerion), a photon index of  $\Gamma = 2.33^{+0.14}_{-0.10}$ , and a temperature of  $kT = 0.19^{+0.02}_{-0.02}$  keV ( $\chi^2_\nu = 0.755$ ,  $\nu = 1060$ ).

Alternatively, emission from a hot diffuse gas can be searched for using the *mekal* model (Appendix B). Once again, the thermal model alone results in a low column density and high temperature (Table 7.3). Allowing the element abundances to vary we find strong evidence of excess emission due to magnesium. Using a two component model (*power+mekal*) resulted in a column density consistent with that found for the plerion ( $2.31^{+0.24}_{-0.21} \times 10^{22}$  atoms  $\text{cm}^{-2}$ , compared to  $2.33^{+0.02}_{-0.01} \times 10^{22}$  atoms  $\text{cm}^{-2}$ ). This model also produces a photon index of  $\Gamma = 2.30^{+0.09}_{-0.10}$  for the non-thermal component and a temperature of  $kT = 0.17^{+0.02}_{-0.03}$  keV ( $2.0^{+0.2}_{-0.3} \times 10^6$  K) for the thermal component ( $\chi^2_\nu = 0.753$ ,  $\nu = 1061$ ).

The evidence presented here for a thermal origin of the emission from the knots indicates that the knots are composed of shocked ejecta from the SN explosion. We therefore conclude that the northern knots identify the location of the reverse shock, which is propagating backward through SN ejecta toward the plerion. Thermal emission was recently confirmed from the northern knots by Bocchino [9] using data from the XMM-Newton Mission.

## 7.6 Eastern Limb

Due to the lower count rate in the limb, the results are less conclusive than those for the knots. As shown in Table 7.3, the spectrum of the limb has a similar appearance to the spectrum of the knots. A power-law results in a photon index of  $\Gamma = 2.47_{-0.08}^{+0.09}$  for a column density of  $N_{\text{H}} = 2.33 \times 10^{22}$  atoms  $\text{cm}^{-2}$ . In the case of the limb, excess emission above the power-law is observed at 1.2, 1.7, 2.3, and 2.5 keV (Figure 7.7). The addition of Gaussians on top of the power-law at these energies resulted in F-test probabilities of 0.63, 0.96, 0.28, and 0.15 respectively. These values indicate that the improvement to the model may have occurred by chance, rather than due to a more suitable model. Therefore, we conclude that the limb is likely shock-heated ISM (mainly hydrogen) rather than shock-heated ejecta (which would contain heavy elements), and that we have located the long-sought SNR shell (forward shock) for G21.5-0.9.

## 7.7 SS 397

The point source in the southwest of the X-ray halo of G21.5-0.9 was fit with an absorbed blackbody model (*wabs\*body*). The best fit was found to occur for a hydrogen column density of  $N_{\text{H}} = 0.16_{-0.16}^{+0.29} \times 10^{22}$  atoms  $\text{cm}^{-2}$ , and a temperature of  $kT = 1.11_{-0.15}^{+0.24}$  keV. The low column density, when compared with the overall column density for G21.5-0.9, indicates that SS 397 is a foreground object and unrelated to the SNR G21.5-0.9. For this reason, emission from SS 397 was omitted from the datasets when obtaining spectra for the halo (Section 7.4 and 7.8).

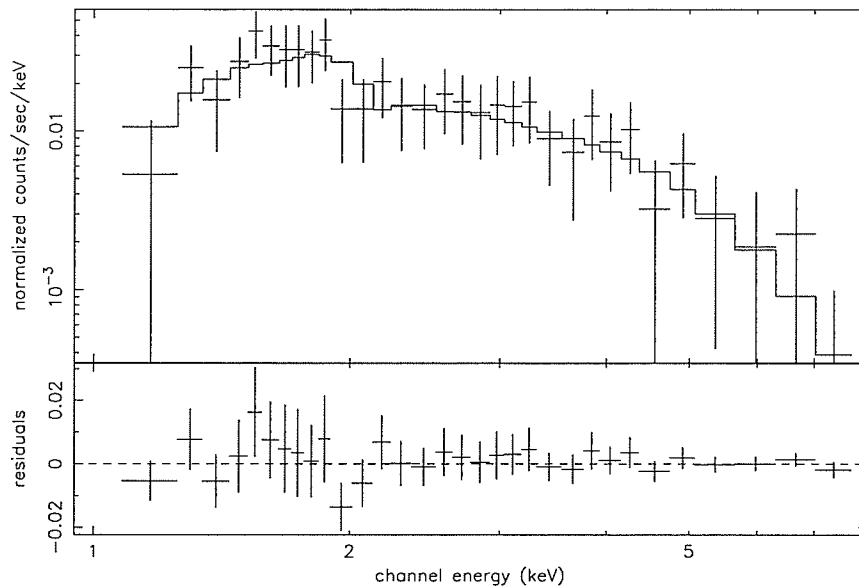


Figure 7.7 - A sample spectrum (obsID 5166) of the eastern limb, showing the data (crosses), model (solid line), and residuals (bottom panel) of the fit to an absorbed power-law (*const\*wabs\*power* in *XSPEC*).

## 7.8 Radial Variations

The variation in the spectrum of G21.5-0.9, as a function of radius from the pulsar, was tested using a power-law (Figures 7.8, 7.9, and 7.10). The power-law spectrum is expected to steepen (i.e. soften) with increasing radius across a plerion, due to the shorter lifetime of higher energy electrons. Concentric rings, centred on  $\alpha(2000) = 18^{\text{h}}33^{\text{m}}33^{\text{s}}.54$ ,  $\delta(2000) = -10^{\circ}34'07''.6$ , were fit with the hydrogen column density allowed to vary, and with  $N_{\text{H}}$  fixed at the best fit value of  $2.33 \times 10^{22}$  atoms  $\text{cm}^{-2}$  (Section 7.3). The photon index was found to increase with radius, from  $\Gamma = 1.61_{-0.02}^{+0.02}$  ( $1.50_{-0.02}^{+0.01}$  when  $N_{\text{H}} = 2.33 \times 10^{22}$  atoms  $\text{cm}^{-2}$ ) at  $0''-5''$ , to  $\Gamma = 2.10_{-0.08}^{+0.09}$  ( $2.23_{-0.03}^{+0.02}$  when  $N_{\text{H}} = 2.33 \times 10^{22}$  atoms  $\text{cm}^{-2}$ ) at the edge of the plerion (Figures 7.9 and 7.10). When  $N_{\text{H}}$  is allowed to vary, the general trend

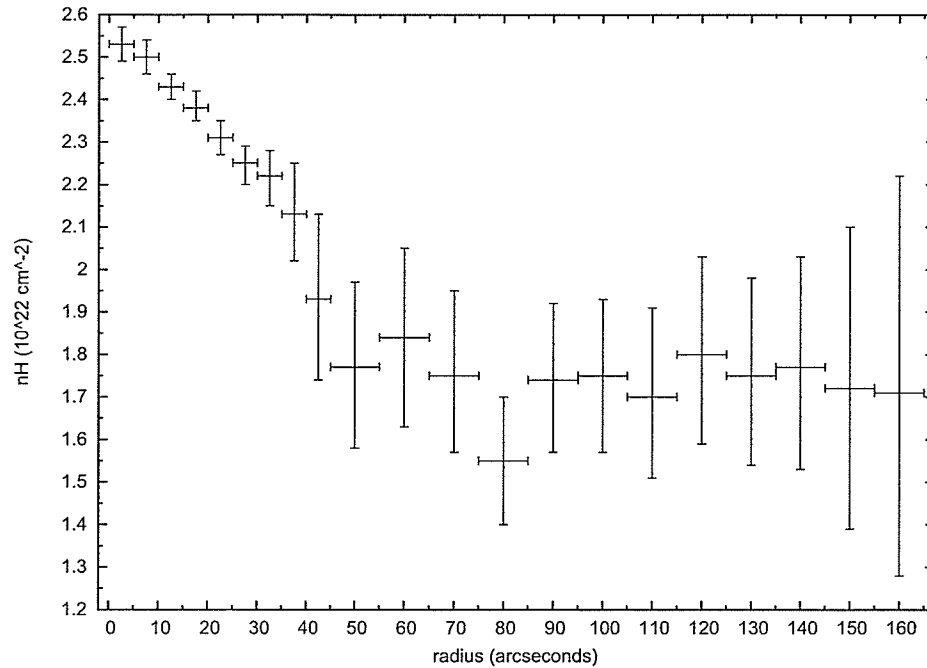


Figure 7.8 - Radial variations in  $N_{\text{H}}$  in the power-law spectrum of G21.5-0.9.

is a decrease in  $N_{\text{H}}$  with an increase in radius across the plerion (Figure 7.8). Above 40'' (the edge of the plerion), the observed number of counts decreases dramatically, but  $\Gamma$  seems to be constant at  $\sim 2.1$  ( $\sim 2.6$  when  $N_{\text{H}} = 2.33 \times 10^{22}$  atoms  $\text{cm}^{-2}$ ). The constant value for the photon index across the halo suggests that the halo is unlikely to be an extension of the plerion ( $\Gamma$  increases with increasing radius in the plerion). The halo is therefore likely to be composed of emission from SN ejecta and shock-heated ISM, with a possible component due to dust-scattering.

Notice that the surface brightness profile in Figure 6.8 shows the main contribution to the northern knots at 80''. The spectral variation plots in Figures 7.8, 7.9, and 7.10 show deviation from a smooth curve at 80''.

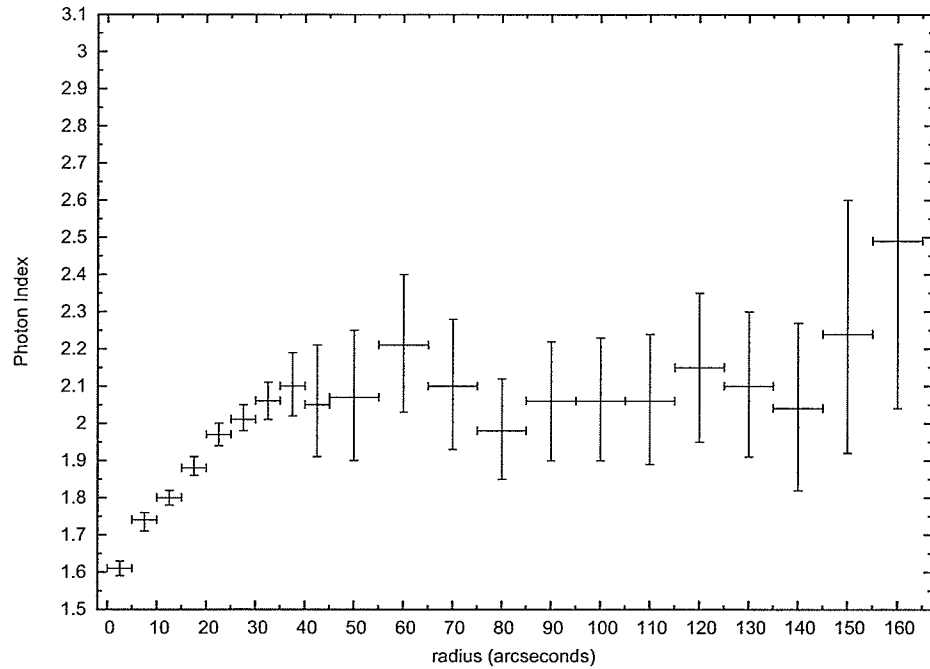


Figure 7.9 - Radial variations in the photon index ( $\Gamma$ ) in the power-law spectrum of G21.5-0.9 when  $N_{\text{H}}$  is allowed to vary.

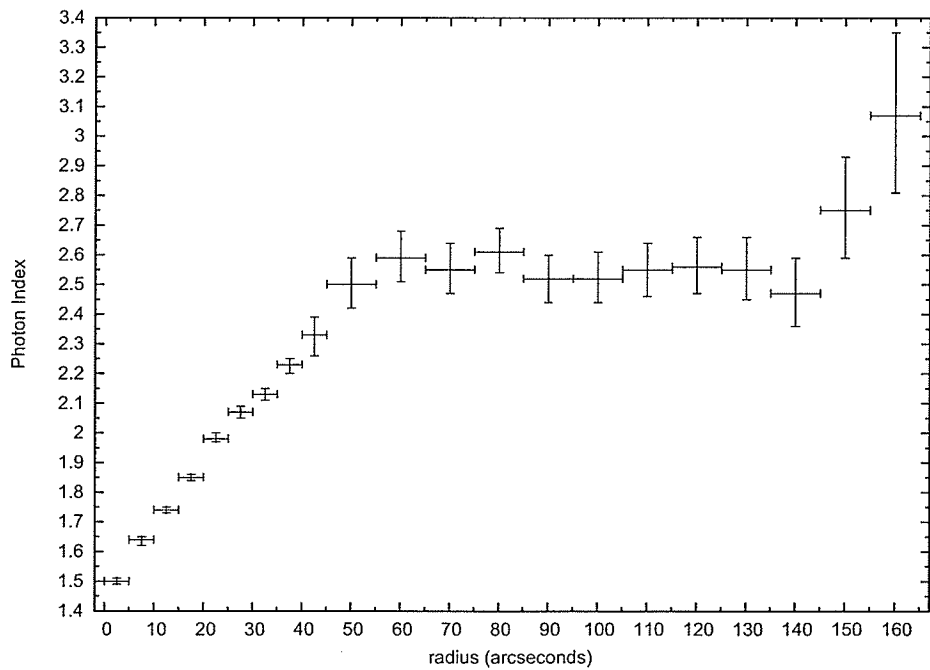


Figure 7.10 - Radial variations in the photon index ( $\Gamma$ ) in the power-law spectrum of G21.5-0.9 when  $N_{\text{H}} = 2.33 \times 10^{22}$  atoms  $\text{cm}^{-2}$ .

Table 7.2. Spectral fitting results for the plerion of G21.5-0.9<sup>a</sup>

		Compact Source	PWN (4''-40'')	PWN (0''-40'')
min # cts/bin		50	100	100
power	$N_{\text{H}}$ ( $10^{22}$ atoms $\text{cm}^{-2}$ )	2.54 (2.49 - 2.59)	2.33 (2.32 - 2.35)	2.34 (2.33 - 2.36)
	$\Gamma$	1.63 (1.60 - 1.66)	1.86 (1.85 - 1.87)	1.82 (1.81 - 1.83)
	norm ( $10^{-3}$ ) <sup>c</sup>	2.59 (2.47 - 2.72)	18.0 (17.7 - 18.3)	20.3 (20.0 - 20.6)
	I0,-110 const	0.56 (0.53-0.59)	0.94 (0.92 - 0.95)	0.88 (0.87 - 0.89)
	I1,-110 const	0.91 (0.89 - 0.93)	0.92 (0.91 - 0.93)	0.92 (0.91 - 0.93)
	I2,-110 const	0.83 (0.79 - 0.87)	0.89 (0.88 - 0.90)	0.88 (0.87 - 0.89)
	I3,-110 const	0.91 (0.89 - 0.93)	0.89 (0.88 - 0.90)	0.90 (0.89 - 0.91)
	S2,-110 const	0.84 (0.82 - 0.86)	0.91 (0.89 - 0.92)	0.90 (0.89 - 0.91)
	S3,-110 const	1.01 (0.99 - 1.03)	0.97 (0.96 - 0.98)	0.98 (0.97 - 0.99)
	I1,-120 const	0.88 (0.86 - 0.90)	0.92 (0.91 - 0.93)	0.91 (0.90 - 0.92)
	I3,-120 const	0.87 (0.86 - 0.89)	0.92 (0.91 - 0.93)	0.92 (0.91 - 0.93)
	S2,-120 const	0.91 (0.89 - 0.94)	0.91 (0.90 - 0.92)	0.91 (0.90 - 0.92)
	S3,-120 const	1.00 (frozen)	1.00 (frozen)	1.00 (frozen)
	$\chi^2_{\nu}$ ( $\nu$ )	0.762 (3192)	1.007 (8060)	1.020 (9202)
	flux ( $10^{-12}$ ) <sup>d</sup>	$7.5 \pm 0.6$	$39.4 \pm 1.7$	$47.0 \pm 2.1$
	unabsorbed flux ( $10^{-11}$ ) <sup>d</sup>	$1.3 \pm 0.2$	$8.1 \pm 0.6$	$9.4 \pm 0.7$
	luminosity ( $10^{34}$ erg $\text{s}^{-1}$ ) <sup>b</sup>	$3.9 \pm 0.6$	$24 \pm 2$	$28 \pm 2$
power	$N_{\text{H}}$ ( $10^{22}$ atoms $\text{cm}^{-2}$ )	2.33 (frozen)		
	$\Gamma$	1.51 (1.49 - 1.53)		
	norm ( $10^{-3}$ ) <sup>c</sup>	2.15 (2.12 - 2.19)		
	I0,-110 const	0.56 (0.53-0.59)		
	I1,-110 const	0.91 (0.89 - 0.93)		
	I2,-110 const	0.83 (0.79 - 0.87)		
	I3,-110 const	0.91 (0.89 - 0.93)		
	S2,-110 const	0.84 (0.82 - 0.86)		
	S3,-110 const	1.01 (0.99 - 1.03)	---	---
	I1,-120 const	0.88 (0.86 - 0.90)		
	I3,-120 const	0.87 (0.86 - 0.88)		
	S2,-120 const	0.91 (0.89 - 0.94)		
	S3,-120 const	1.00 (frozen)		
	$\chi^2_{\nu}$ ( $\nu$ )	0.777 (3193)		
	flux ( $10^{-12}$ ) <sup>d</sup>	$7.7 \pm 0.6$		
	unabsorbed flux ( $10^{-11}$ ) <sup>d</sup>	$1.2 \pm 0.2$		
	luminosity ( $10^{34}$ erg $\text{s}^{-1}$ ) <sup>b</sup>	$3.6 \pm 0.6$		

<sup>a</sup>All confidence ranges are 90%. All models were fit to the data on the range 0.5 - 8.0 keV.

<sup>b</sup>Assuming a distance of 5 kpc.

<sup>c</sup>Units for the normalization factor on the power-law model are photons  $\text{keV}^{-1} \text{cm}^{-2} \text{s}^{-1}$ .

<sup>d</sup>Units of flux are  $\text{erg cm}^{-2} \text{s}^{-1}$ .

Table 7.3. Spectral fitting results for the X-ray halo of G21.5-0.9<sup>a</sup>

		Halo (40''-150'')	Northern Knots	Eastern Limb
min # cts/bin		100	50	20
power	$N_H$ ( $10^{22}$ atoms $\text{cm}^{-2}$ )	1.68 (1.59 - 1.78)	1.73 (1.67 - 1.79)	1.75 (1.57 - 1.95)
	$\Gamma$	2.06 (1.97 - 2.14)	2.04 (1.99 - 2.10)	2.03 (1.86 - 2.20)
	norm ( $10^{-3}$ ) <sup>c</sup>	4.34 (3.89 - 4.86)	1.23 (1.15 - 1.33)	0.401 (0.320 - 0.507)
	I0,-110 const	—	0.93 (0.87 - 0.99)	—
	I1,-110 const	0.90 (0.77 - 1.03)	0.91 (0.88 - 0.94)	0.93 (0.73 - 1.14)
	I2,-110 const	0.90 (0.79 - 1.01)	0.87 (0.81 - 0.93)	0.97 (0.77 - 1.18)
	I3,-110 const	0.94 (0.87 - 1.01)	0.92 (0.88 - 0.95)	0.97 (0.84 - 1.12)
	S2,-110 const	0.91 (0.85 - 0.98)	0.89 (0.88 - 0.93)	0.97 (0.86 - 1.09)
	S3,-110 const	1.00 (0.93 - 1.07)	1.00 (0.96 - 1.04)	0.98 (0.87 - 1.09)
	I1,-120 const	—	0.95 (0.92 - 0.99)	0.85 (0.77 - 0.93)
	I3,-120 const	0.91 (0.87 - 0.94)	0.92 (0.89 - 0.94)	0.87 (0.80 - 0.94)
	S2,-120 const	0.98 (0.90 - 1.06)	0.93 (0.88 - 0.98)	1.02 (0.94 - 1.17)
	S3,-120 const	1.00 (frozen)	1.00 (frozen)	1.00 (frozen)
	$\chi^2_\nu$ ( $\nu$ )	0.372 (1455)	0.775 (1063)	0.391 (909)
	flux ( $10^{-12}$ ) <sup>d</sup>	$8.0 \pm 0.4$	$2.3 \pm 0.1$	$0.76 \pm 0.05$
	unabsorbed flux ( $10^{-11}$ ) <sup>d</sup>	$1.7 \pm 0.2$	$0.44 \pm 0.07$	$0.16 \pm 0.02$
	luminosity ( $10^{34}$ erg $\text{s}^{-1}$ ) <sup>b</sup>	$5.1 \pm 0.6$	$1.3 \pm 0.2$	$0.48 \pm 0.06$
power	$N_H$ ( $10^{22}$ atoms $\text{cm}^{-2}$ )	2.33 (frozen)	2.33 (frozen)	2.33 (frozen)
	$\Gamma$	2.55 (2.51 - 2.60)	2.48 (2.45 - 2.50)	2.47 (2.39 - 2.56)
	norm ( $10^{-3}$ ) <sup>c</sup>	8.65 (8.25 - 9.06)	2.29 (2.22 - 2.36)	0.742 (0.679 - 0.809)
	I0,-110 const	—	0.94 (0.88 - 0.99)	—
	I1,-110 const	0.91 (0.78 - 1.05)	0.91 (0.88 - 0.95)	0.94 (0.73 - 1.15)
	I2,-110 const	0.92 (0.81 - 1.03)	0.88 (0.82 - 0.95)	0.98 (0.78 - 1.19)
	I3,-110 const	0.94 (0.87 - 1.02)	0.92 (0.89 - 0.96)	0.98 (0.84 - 1.12)
	S2,-110 const	0.93 (0.86 - 0.99)	0.90 (0.86 - 0.94)	0.98 (0.87 - 1.10)
	S3,-110 const	1.00 (0.94 - 1.08)	1.01 (0.97 - 1.05)	0.98 (0.87 - 1.10)
	I1,-120 const	—	0.96 (0.92 - 1.00)	0.87 (0.79 - 0.95)
	I3,-120 const	0.91 (0.88 - 0.95)	0.92 (0.89 - 0.95)	0.87 (0.80 - 0.95)
	S2,-120 const	0.99 (0.91 - 1.07)	0.94 (0.89 - 0.98)	1.02 (0.87 - 1.17)
	S3,-120 const	1.00 (frozen)	1.00 (frozen)	1.00 (frozen)
	$\chi^2_\nu$ ( $\nu$ )	0.444 (1456)	0.972 (1064)	0.412 (910)
	flux ( $10^{-12}$ ) <sup>d</sup>	$7.5 \pm 0.3$	$2.2 \pm 0.1$	$0.71 \pm 0.04$
	unabsorbed flux ( $10^{-11}$ ) <sup>d</sup>	$2.6 \pm 0.3$	$0.62 \pm 0.16$	$0.23 \pm 0.04$
	luminosity ( $10^{34}$ erg $\text{s}^{-1}$ ) <sup>b</sup>	$7.8 \pm 0.9$	$1.9 \pm 0.5$	$0.69 \pm 0.12$
pshock	$N_H$ ( $10^{22}$ atoms $\text{cm}^{-2}$ )	1.44 (1.38 - 1.50)	1.48 (1.43 - 1.52)	1.49 (1.36 - 1.63)
	$kT$ keV	4.96 (4.50 - 5.50)	5.06 (4.76 - 5.40)	5.48 (4.38 - 7.09)
	$n_e t$ ( $10^8$ s $\text{cm}^{-3}$ )	5.99 (1 - 9.88)	2.54 (1 - 6.76)	8.60 (1 - 16.0)
	norm ( $10^{-3}$ $\text{cm}^{-5}$ )	11.3 (10.7 - 12.2)	3.28 (3.13 - 3.43)	1.03 (0.92 - 1.19)
	I0,-110 const	—	0.93 (0.88 - 0.99)	—
	I1,-110 const	0.90 (0.77 - 1.03)	0.92 (0.88 - 0.95)	0.93 (0.72 - 1.14)
	I2,-110 const	0.91 (0.80 - 1.02)	0.87 (0.81 - 0.94)	0.97 (0.77 - 1.18)
	I3,-110 const	0.94 (0.87 - 1.01)	0.92 (0.88 - 0.95)	0.98 (0.83 - 1.12)
	S2,-110 const	0.91 (0.85 - 0.98)	0.90 (0.86 - 0.94)	0.98 (0.86 - 1.09)
	S3,-110 const	1.00 (0.93 - 1.07)	1.00 (0.96 - 1.04)	0.98 (0.87 - 1.10)
	I1,-120 const	—	0.96 (0.92 - 1.00)	0.85 (0.77 - 0.94)
	I3,-120 const	0.91 (0.88 - 0.95)	0.92 (0.89 - 0.95)	0.87 (0.80 - 0.94)
	S2,-120 const	0.98 (0.90 - 1.07)	0.93 (0.89 - 0.98)	1.02 (0.87 - 1.18)
	S3,-120 const	1.00 (frozen)	1.00 (frozen)	1.00 (frozen)
	$\chi^2_\nu$ ( $\nu$ )	0.381 (1454)	0.786 (1062)	0.394 (908)
	flux ( $10^{-12}$ ) <sup>d</sup>	$7.8 \pm 0.3$	$2.2 \pm 0.1$	$0.75 \pm 0.05$
	unabsorbed flux ( $10^{-11}$ ) <sup>d</sup>	$1.5 \pm 0.2$	$0.35 \pm 0.04$	$0.17 \pm 0.04$
luminosity ( $10^{34}$ erg $\text{s}^{-1}$ ) <sup>b</sup>	$4.5 \pm 0.6$	$1.1 \pm 0.1$	$0.51 \pm 0.12$	
vpshock	Mg abundance	0 (0 - 8.0)	5.3 (0 - 45.8)	0 (0 - 6.4)
	Si abundance	0.7 (0 - 2.7)	0 (0 - 8.1)	1.1 (0 - 2.8)
	S abundance	11.6 (3.4 - 19.9)	85.6 (42.5 - 128.8)	3.7 (1 - 13.1)
pshock	$N_H$ ( $10^{22}$ atoms $\text{cm}^{-2}$ )	2.33 (frozen)	2.33 (frozen)	2.33 (frozen)
	$kT$ keV	4.07 (3.80 - 4.33)	2.62 (2.55 - 2.69)	4.29 (3.77 - 4.96)

Table 7.3—Continued

	Halo (40''-150'')	Northern Knots	Eastern Limb
$n_{e,t}$ ( $10^9$ s $\text{cm}^{-3}$ )	8.5 (7.8 - 9.1)	0.1 (0.1 - 0.5)	8.2 (7.1 - 9.4)
norm <sup>c</sup> ( $10^{-3}$ )	13.7 (13.1 - 14.4)	6.3 (6.1 - 6.4)	1.26 (1.16 - 1.37)
I0,-110 const	—	0.94 (0.89 - 1.00)	—
I1,-110 const	0.90 (0.77 - 1.03)	0.92 (0.89 - 0.95)	0.93 (0.72 - 1.13)
I2,-110 const	0.91 (0.80 - 1.02)	0.91 (0.84 - 0.97)	0.96 (0.76 - 1.17)
I3,-110 const	0.94 (0.86 - 1.01)	0.93 (0.89 - 0.96)	0.98 (0.83 - 1.12)
S2,-110 const	0.91 (0.84 - 0.97)	0.91 (0.87 - 0.94)	0.98 (0.86 - 1.10)
S3,-110 const	0.99 (0.92 - 1.06)	1.02 (0.98 - 1.06)	0.98 (0.86 - 1.09)
I1,-120 const	—	0.97 (0.93 - 1.01)	0.87 (0.79 - 0.96)
I3,-120 const	0.90 (0.87 - 0.94)	0.93 (0.90 - 0.96)	0.86 (0.79 - 0.93)
S2,-120 const	0.97 (0.89 - 1.05)	0.95 (0.90 - 1.00)	1.02 (0.87 - 1.17)
S3,-120 const	1.00 (frozen)	1.00 (frozen)	1.00 (frozen)
$\chi^2_\nu$ ( $\nu$ )	0.545 (1455)	1.44 (1063)	0.454 (909)
flux ( $10^{-12}$ ) <sup>d</sup>	$7.8 \pm 0.4$	$2.0 \pm 0.1$	$0.74 \pm 0.04$
unabsorbed flux ( $10^{-11}$ ) <sup>d</sup>	$13.1 \pm 4.8$	$0.45 \pm 0.05$	$1.1 \pm 0.5$
luminosity ( $10^{34}$ erg $\text{s}^{-1}$ ) <sup>b</sup>	$39 \pm 2$	$1.4 \pm 0.2$	$3.3 \pm 1.5$
vpshock			
Mg abundance	1.18 (1.05 - 1.30)	0 (0 - 80.9)	1.14 (0.90 - 1.37)
Si abundance	0.59 (0.47 - 0.70)	0 (0 - 62.3)	0.68 (0.47 - 0.89)
S abundance	0.53 (0.29 - 0.78)	0 (0 - 122.6)	0.39 (0 - 0.88)
power+pshock			
$N_{\text{H}}$ ( $10^{22}$ atoms $\text{cm}^{-2}$ )	1.72 (1.61 - 2.12)	2.45 (2.20 - 2.81)	1.86 (1.60 - 2.54)
$\Gamma$	2.08 (1.99 - 2.24)	2.33 (2.23 - 2.47)	2.09 (1.88 - 2.40)
norm ( $10^{-3}$ ) <sup>c</sup>	4.48 (3.95 - 5.19)	1.95 (1.66 - 2.42)	0.44 (0.04 - 0.69)
$kT$ keV	0.08 (0.08 - 1.59)	0.19 (0.17 - 0.21)	0.10 (0.08 - 2.48)
$n_{e,t}$ ( $10^9$ s $\text{cm}^{-3}$ )	2.01 (1E8 - 5E13)	0.42 (1E8 - 2.29E9)	1.67 (1E8 - 5E13)
norm ( $10^0$ $\text{cm}^{-5}$ )	49.2 (0 - 177.3)	1.04 (0.37 - 2.17)	1.99 (0 - 44.73)
I0,-110 const	—	0.93 (0.88 - 0.99)	—
I1,-110 const	0.90 (0.77 - 1.03)	0.91 (0.88 - 0.95)	0.93 (0.73 - 1.14)
I2,-110 const	0.90 (0.79 - 1.01)	0.88 (0.81 - 0.94)	0.97 (0.77 - 1.08)
I3,-110 const	0.94 (0.87 - 1.01)	0.92 (0.88 - 0.95)	0.98 (0.84 - 1.12)
S2,-110 const	0.91 (0.85 - 0.98)	0.90 (0.86 - 0.94)	0.98 (0.86 - 1.10)
S3,-110 const	1.00 (0.93 - 1.07)	1.00 (0.96 - 1.04)	0.98 (0.87 - 1.10)
I1,-120 const	—	0.96 (0.92 - 0.99)	0.85 (0.77 - 0.94)
I3,-120 const	0.91 (0.87 - 0.94)	0.92 (0.89 - 0.95)	0.87 (0.80 - 0.94)
S2,-120 const	0.98 (0.90 - 1.06)	0.93 (0.89 - 0.98)	1.02 (0.87 - 1.10)
S3,-120 const	1.00 (frozen)	1.00 (frozen)	1.00 (frozen)
$\chi^2_\nu$ ( $\nu$ )	0.372 (1452)	0.755 (1060)	0.391 (906)
flux ( $10^{-12}$ ) <sup>d</sup>	$8.0 \pm 0.4$	$2.25 \pm 0.10$	$0.77 \pm 0.05$
unabsorbed flux ( $10^{-11}$ ) <sup>d</sup>	$11.4 \pm 8.2$	$1.9 \pm 1.4$	$1.9 \pm 1.8$
luminosity ( $10^{34}$ erg $\text{s}^{-1}$ ) <sup>b</sup>	$34.1 \pm 2.5$	$5.7 \pm 4.2$	$5.7 \pm 5.4$
thermal flux ( $10^{-15}$ ) <sup>d</sup>	$9.6 \pm 4.9$	$52.5 \pm 7.2$	$17.2 \pm 47.2$
non-thermal flux ( $10^{-12}$ ) <sup>d</sup>	$8.0 \pm 0.4$	$2.19 \pm 0.09$	$0.75 \pm 0.05$
power+pshock			
$N_{\text{H}}$ ( $10^{22}$ atoms $\text{cm}^{-2}$ )	2.33 (frozen)	2.33 (frozen)	2.33 (frozen)
$\Gamma$	2.29 (2.19 - 2.37)	2.29 (2.25 - 2.33)	2.28 (2.15 - 2.43)
norm ( $10^{-3}$ ) <sup>c</sup>	6.28 (5.52 - 6.98)	1.82 (1.72 - 1.91)	0.595 (0.429 - 0.642)
$kT$ keV	0.22 (0.18 - 0.26)	0.18 (0.16 - 0.21)	0.19 (0.11 - 0.38)
$n_{e,t}$ ( $10^8$ s $\text{cm}^{-3}$ )	3.3 (1 - 16.1)	12.1 (1 - 25.1)	1.85 (1 - 41.5)
norm ( $10^0$ $\text{cm}^{-5}$ )	1.06 (0.41 - 1.34)	0.76 (0.37 - 1.39)	0.168 (0.003 - 0.331)
I0,-110 const	—	0.93 (0.88 - 0.99)	—
I1,-110 const	0.90 (0.77 - 1.03)	0.91 (0.88 - 0.95)	0.93 (0.73 - 1.14)
I2,-110 const	0.90 (0.79 - 1.01)	0.88 (0.81 - 0.94)	0.98 (0.77 - 1.19)
I3,-110 const	0.94 (0.87 - 1.01)	0.92 (0.89 - 0.95)	0.98 (0.84 - 1.05)
S2,-110 const	0.91 (0.85 - 0.98)	0.90 (0.86 - 0.94)	0.98 (0.86 - 1.10)
S3,-110 const	1.00 (0.93 - 1.07)	1.00 (0.96 - 1.04)	0.98 (0.87 - 1.10)
I1,-120 const	—	0.96 (0.92 - 0.99)	0.85 (0.77 - 0.94)
I3,-120 const	0.91 (0.87 - 0.94)	0.92 (0.89 - 0.95)	0.87 (0.80 - 0.94)
S2,-120 const	0.98 (0.90 - 1.06)	0.93 (0.89 - 0.98)	1.02 (0.87 - 1.18)
S3,-120 const	1.00 (frozen)	1.00 (frozen)	1.00 (frozen)
$\chi^2_\nu$ ( $\nu$ )	0.375 (1453)	0.755 (1061)	0.393 (907)

Table 7.3—Continued

	Halo (40''-150'')	Northern Knots	Eastern Limb	
	flux ( $10^{-12}$ ) <sup>d</sup>	$7.9 \pm 0.4$	$2.27 \pm 0.11$	$0.74 \pm 0.05$
	unabsorbed flux ( $10^{-11}$ ) <sup>d</sup>	$5.8 \pm 1.5$	$6.0 \pm 7.6$	$0.42 \pm 0.17$
	luminosity ( $10^{34}$ erg s <sup>-1</sup> ) <sup>b</sup>	$17.3 \pm 4.5$	$17.9 \pm 22.7$	$1.26 \pm 0.51$
	thermal flux ( $10^{-13}$ ) <sup>d</sup>	$2.0 \pm 0.1$	$0.61 \pm 0.59$	$0.12 \pm 0.01$
	non-thermal flux ( $10^{-12}$ ) <sup>d</sup>	$7.7 \pm 0.3$	$2.21 \pm 0.09$	$0.73 \pm 0.05$
mekal	$N_{\text{H}}$ ( $10^{22}$ atoms cm <sup>-2</sup> )	1.45 (1.37 - 1.55)	1.48 (1.43 - 1.53)	1.52 (1.36 - 1.67)
	$kT$ keV	5.12 (4.36 - 5.68)	5.22 (4.85 - 5.61)	5.33 (4.31 - 7.18)
	norm ( $10^{-3}$ cm <sup>-5</sup> )	9.13 (8.67 - 9.82)	2.63 (2.54 - 2.73)	0.88 (0.79 - 0.97)
	I0,-110 const	—	0.93 (0.87 - 0.99)	—
	I1,-110 const	0.90 (0.77 - 1.03)	0.92 (0.88 - 0.95)	0.93 (0.73 - 1.14)
	I2,-110 const	0.90 (0.79 - 1.01)	0.88 (0.82 - 0.95)	0.97 (0.77 - 1.18)
	I3,-110 const	0.94 (0.86 - 1.01)	0.92 (0.89 - 0.96)	0.98 (0.84 - 1.13)
	S2,-110 const	0.91 (0.85 - 0.98)	0.91 (0.87 - 0.95)	0.98 (0.87 - 1.10)
	S3,-110 const	1.00 (0.93 - 1.07)	1.00 (0.96 - 1.04)	0.98 (0.87 - 1.10)
	I1,-120 const	—	0.96 (0.92 - 1.00)	0.85 (0.77 - 0.93)
	I3,-120 const	0.91 (0.87 - 0.94)	0.92 (0.89 - 0.95)	0.87 (0.80 - 0.94)
	S2,-120 const	0.98 (0.89 - 1.06)	0.94 (0.89 - 0.95)	1.02 (0.87 - 1.18)
	S3,-120 const	1.00 (frozen)	1.00 (frozen)	1.00 (frozen)
	$\chi^2_{\nu}$ ( $\nu$ )	0.445 (1455)	0.927 (1063)	0.404 (909)
	flux ( $10^{-12}$ ) <sup>d</sup>	$8.6 \pm 0.4$	$2.5 \pm 0.1$	$0.83 \pm 0.05$
	unabsorbed flux ( $10^{-11}$ ) <sup>d</sup>	$1.4 \pm 0.1$	$0.39 \pm 0.04$	$0.14 \pm 0.01$
	luminosity ( $10^{34}$ erg s <sup>-1</sup> ) <sup>b</sup>	$4.3 \pm 0.3$	$1.2 \pm 0.1$	$0.41 \pm 0.03$
vmekal	Mg abundance	1.36 (0.49 - 2.22)	0.84 (0.30 - 1.39)	0.54 (0 - 2.19)
	Si abundance	0.44 (0.06 - 0.81)	0.43 (0.18 - 0.68)	0.47 (0 - 1.21)
	S abundance	0.97 (0.43 - 1.51)	0.88 (0.53 - 1.24)	1.06 (0 - 2.19)
mekal	$N_{\text{H}}$ ( $10^{22}$ atoms cm <sup>-2</sup> )	2.33 (frozen)	2.33 (frozen)	2.33 (frozen)
	$kT$ keV	2.64 (2.56 - 2.73)	2.80 (2.75 - 2.86)	2.76 (2.59 - 2.96)
	norm ( $10^{-3}$ cm <sup>-5</sup> )	14.7 (14.3 - 15.1)	4.10 (4.02 - 4.18)	1.35 (1.27 - 1.42)
	I0,-110 const	—	0.94 (0.89 - 1.00)	—
	I1,-110 const	0.94 (0.80 - 1.07)	0.93 (0.89 - 0.96)	0.96 (0.75 - 1.18)
	I2,-110 const	0.94 (0.83 - 1.06)	0.92 (0.85 - 0.98)	1.00 (0.79 - 1.21)
	I3,-110 const	0.96 (0.89 - 1.04)	0.94 (0.90 - 0.97)	1.00 (0.85 - 1.15)
	S2,-110 const	0.94 (0.88 - 1.01)	0.91 (0.88 - 0.96)	1.00 (0.88 - 1.13)
	S3,-110 const	1.01 (0.94 - 1.09)	1.01 (0.97 - 1.06)	0.98 (0.87 - 1.10)
	I1,-120 const	—	0.98 (0.94 - 1.02)	0.89 (0.81 - 0.98)
	I3,-120 const	0.92 (0.88 - 0.95)	0.93 (0.90 - 0.96)	0.88 (0.81 - 0.96)
	S2,-120 const	1.00 (0.92 - 1.09)	0.96 (0.91 - 1.01)	1.04 (0.88 - 1.20)
	S3,-120 const	1.00 (frozen)	1.00 (frozen)	1.00 (frozen)
	$\chi^2_{\nu}$ ( $\nu$ )	0.639 (1456)	1.541 (1064)	0.478 (910)
	flux ( $10^{-12}$ ) <sup>d</sup>	$7.7 \pm 0.3$	$2.3 \pm 0.1$	$0.73 \pm 0.04$
	unabsorbed flux ( $10^{-11}$ ) <sup>d</sup>	$2.0 \pm 0.1$	$0.52 \pm 0.06$	$0.18 \pm 0.01$
	luminosity ( $10^{34}$ erg s <sup>-1</sup> ) <sup>b</sup>	$6.0 \pm 0.3$	$1.6 \pm 0.2$	$0.54 \pm 0.04$
vmekal	Mg abundance	2.42 (1.87 - 2.97)	2.39 (2.03 - 2.76)	2.02 (0.97 - 3.07)
	Si abundance	0.34 (0.18 - 0.49)	0.34 (0.23 - 0.46)	0.38 (0.07 - 0.70)
	S abundance	0.22 (0.03 - 0.41)	0.20 (0.07 - 0.33)	0.27 (0 - 0.68)
power+mekal	$N_{\text{H}}$ ( $10^{22}$ atoms cm <sup>-2</sup> )	1.72 (1.61 - 1.93)	2.31 (2.10 - 2.55)	1.81 (1.59 - 2.21)
	$\Gamma$	2.08 (1.99 - 2.20)	2.30 (2.20 - 2.39)	2.06 (1.88 - 2.31)
	norm ( $10^{-3}$ ) <sup>c</sup>	4.48 (3.96 - 5.16)	1.83 (1.58 - 2.12)	0.42 (0.33 - 0.59)
	$kT$ keV	0.08 (0.08 - 1.37)	0.17 (0.14 - 0.19)	0.08 (0.08 - 8.43)
	norm ( $10^0$ cm <sup>-5</sup> )	1.88 (0 - 6.42)	0.082 (0.032 - 0.159)	0.43 (0 - 2.61)
	I0,-110 const	—	0.94 (0.88 - 0.99)	—
	I1,-110 const	0.90 (0.77 - 1.03)	0.92 (0.88 - 0.95)	0.93 (0.72 - 1.14)
	I2,-110 const	0.90 (0.79 - 1.01)	0.88 (0.82 - 0.94)	0.97 (0.77 - 1.18)
	I3,-110 const	0.94 (0.87 - 1.01)	0.92 (0.89 - 0.96)	0.98 (0.83 - 1.12)
	S2,-110 const	0.91 (0.85 - 0.98)	0.90 (0.86 - 0.94)	0.98 (0.86 - 1.10)
	S3,-110 const	1.00 (0.93 - 1.07)	1.00 (0.96 - 1.04)	0.98 (0.87 - 1.10)
	I1,-120 const	—	0.96 (0.92 - 1.00)	0.85 (0.77 - 0.94)
	I3,-120 const	0.91 (0.87 - 0.94)	0.92 (0.89 - 0.95)	0.87 (0.80 - 0.94)

Table 7.3—Continued

	Halo (40''-150'')	Northern Knots	Eastern Limb
S2,-120 const	0.98 (0.90 - 1.06)	0.94 (0.89 - 0.98)	1.02 (0.87 - 1.18)
S3,-120 const	1.00 (frozen)	1.00 (frozen)	1.00 (frozen)
$\chi^2_\nu$	0.372 (1453)	0.753 (1061)	0.391 (907)
flux ( $10^{-12}$ ) <sup>d</sup>	$8.0 \pm 0.4$	$2.3 \pm 0.1$	$0.77 \pm 0.05$
unabsorbed flux ( $10^{-11}$ ) <sup>d</sup>	$9.1 \pm 4.6$	$3.6 \pm 3.9$	$2.7 \pm 1.0$
luminosity ( $10^{35}$ erg s <sup>-1</sup> ) <sup>b</sup>	$2.7 \pm 1.4$	$1.1 \pm 1.2$	$0.80 \pm 0.28$
power+mekal			
$N_H$ ( $10^{22}$ atoms cm <sup>-2</sup> )	2.33 (frozen)	2.33 (frozen)	2.33 (frozen)
$\Gamma$	2.34 (2.28 - 2.42)	2.30 (2.27 - 2.33)	2.29 (2.15 - 2.43)
norm ( $10^{-3}$ ) <sup>c</sup>	6.74 (6.25 - 7.36)	1.85 (1.76 - 1.93)	0.60 (0.50 - 0.70)
$kT$ keV	0.20 (0.14 - 0.24)	0.17 (0.14 - 0.19)	0.21 (0.09 - 0.38)
norm ( $10^{-2}$ cm <sup>-5</sup> )	10.4 (4.6 - 62.2)	7.55 (4.02 - 22.43)	6.19 (1.06 - 483.5)
I0,-110 const	—	0.94 (0.88 - 0.99)	—
I1,-110 const	0.90 (0.78 - 1.03)	0.92 (0.88 - 0.95)	0.93 (0.73 - 1.15)
I2,-110 const	0.91 (0.80 - 1.02)	0.88 (0.82 - 0.94)	0.98 (0.77 - 1.18)
I3,-110 const	0.94 (0.87 - 1.02)	0.92 (0.89 - 0.96)	0.98 (0.84 - 1.12)
S2,-110 const	0.92 (0.85 - 0.98)	0.90 (0.86 - 0.94)	0.98 (0.86 - 1.10)
S3,-110 const	1.00 (0.93 - 1.07)	1.00 (0.96 - 1.04)	0.98 (0.87 - 1.10)
I1,-120 const	—	0.96 (0.92 - 1.00)	0.86 (0.78 - 0.94)
I3,-120 const	0.91 (0.87 - 0.95)	0.92 (0.89 - 0.95)	0.87 (0.80 - 0.94)
S2,-120 const	0.98 (0.90 - 1.07)	0.94 (0.89 - 0.98)	1.02 (0.87 - 1.18)
S3,-120 const	1.00 (frozen)	1.00 (frozen)	1.00 (frozen)
$\chi^2_\nu$	0.381 (1454)	0.753 (1062)	0.394 (908)
flux ( $10^{-12}$ ) <sup>d</sup>	$7.8 \pm 0.4$	$2.3 \pm 0.1$	$0.74 \pm 0.05$
unabsorbed flux ( $10^{-11}$ ) <sup>d</sup>	$12.3 \pm 4.2$	$3.6 \pm 3.9$	$0.72 \pm 0.13$
luminosity ( $10^{35}$ erg s <sup>-1</sup> ) <sup>b</sup>	$3.7 \pm 1.3$	$1.1 \pm 1.2$	$0.022 \pm 0.004$

<sup>a</sup>All confidence ranges are 90%. All models were fit to the data on the range 0.5 - 8.0 keV.

<sup>b</sup>Assuming a distance of 5 kpc.

<sup>c</sup>Units for the normalization factor on the power-law model are photons keV<sup>-1</sup> cm<sup>-2</sup> s<sup>-1</sup>.

<sup>d</sup>Units of flux are erg cm<sup>-2</sup> s<sup>-1</sup>.

# CHAPTER 8

## SUMMARY, CONCLUSIONS & FUTURE

This thesis makes use of 6 years of archival *Chandra* data to demonstrate the importance of deep searches for shells surrounding plerionic remnants. The technology incorporated into *Chandra* made it possible to study the SNR G21.5-0.9 in detail at a high spatial and spectral resolution by combining many short observations into one effective exposure of 578.6 ks.

This thesis presents the deepest image of a plerionic SNR to date. We have shown a complex structure in the plerion of G21.5-0.9 that was previously unseen, including wisps and a double-lobed morphology. We have also revealed previously unseen features in the X-ray halo surrounding G21.5-0.9, including limb-brightening in the east and knots in the north of the halo that are joined to the limb in the east.

We have demonstrated for the first time the variable nature of the plerion, identifying knots that appear and disappear with time.

A study of the SNR G21.5-0.9 as a function of distance from the pulsar revealed a photon index that increases outward from the pulsar to the edge of the plerion (due to the longer synchrotron lifetimes of lower energy X-rays) and then remains constant across the X-ray halo. The column density was found to dramatically decrease moving outward from the pulsar, which is unphysical (the hydrogen column density should

be approximately constant across G21.5-0.9 since it is at a distance of 5 kpc and is  $\sim 7$  pc in diameter) and is most likely an artifact of the models used.

Evidence of line emission due to heavy elements such as magnesium, silicon, and sulfur was found in the northern knots of the X-ray halo, suggesting these features are formed from the ejecta of the SN. The spectra of the limb lacked the strong evidence for line emission, suggesting that we have identified the SNR shell. The low intensity of this shell suggests that the remnant is expanding into a low density medium. Adding a thermal component to the models used to analyze the spectra was found to significantly improve the fits and resolved the problem of a lower column density in the halo, providing further evidence that the halo is not an extension of the plerion and that the limb is the long-sought SNR shell.

We proposed that the limb identifies the location of the forward shock (shock-heated ISM) and that the northern knots identify the location of the reverse shock (shock-heated SN ejecta). These features are pointed out in Figure 8.1.

It has been a mystery for decades as to why plerionic remnants were not observed to be surrounded by SNR shells. This study of G21.5-0.9, revealing the first SNR shell around a plerion, provides evidence that plerionic remnants may actually create shells, however they are faint and a deep exposure is required to reveal them. A deep search for shells in other Crab-like SNRs is therefore needed to test this theory. A search for a shell surrounding the Crab Nebula (Seward et al., 2006 [41]) revealed a dust-scattered halo with an intensity of 5% that of the Crab, out to a radial distance of  $18'$ . However, there was no evidence of emission from shock-heated material in the form of a shell.

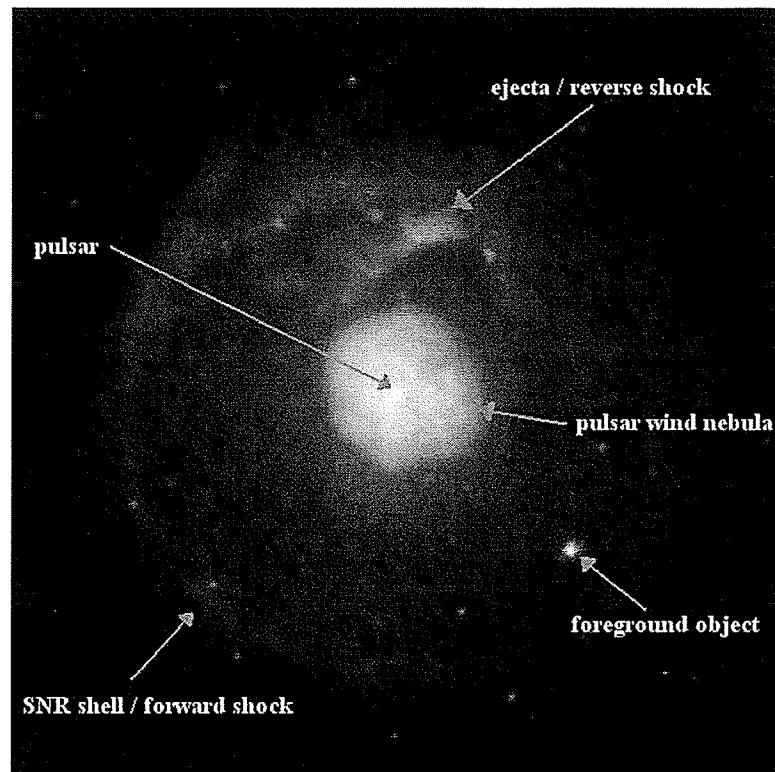


Figure 8.1 - Summary of the components of G21.5-0.9. The pulsar PSR J1833-1034 is located at the centre of the remnant. Detailed and variable structure is visible in the pulsar wind nebula of G21.5-0.9. We have shown that the northern knots are likely the reverse shock (shock-heated SN ejecta) and that the limb is likely the forward shock (shock-heated ISM). The point source SS 397 in the southwest quadrant of the halo was identified as a foreground object. At a distance of 5 kpc, the plerion of G21.5-0.9 has a diameter of 1.9 pc and the halo has a diameter of 7.3 pc.

Now that the SNR shell of G21.5-0.9 has been observed at X-ray wavelengths, a deep search for the shell is needed at radio wavelengths. In addition, since the pulsar has been detected in radio, a timing study of G21.5-0.9 is needed to search for X-ray pulsations.

# APPENDIX A

## SCRIPTS USED IN DATA PREPARATION

### A.1 Creating a cleaned event (evt2) file for *Chandra* data using the CTI corrector in CIAO

```
#!/bin/csh
# Script to create an evt2 file from an evt1 file, using the CTI
# correction available in CIAO.
# Use for ACIS-I, -120 data only.
# Usage: With CIAO running, at prompt type "create_ciao_evt2"

echo "Script to create spectra started ";date

echo "Please enter the observation number:"
set obsid=$(<)
echo "The observation number is set to: ${obsid}"

echo "Please enter the bad pixel file (full path if not in current \
directory):"
set bad=$(<)
echo "The bad pixel file is set to: ${bad}"

echo "Please enter the evt1 file (full path if not in current \
directory):"
set events=$(<)
echo "The event 1 file is set to: ${events}"

echo "Please enter the asol file(s) (full path if not in current \
directory - comma separated list):"
set asolfile=$(<)
echo "The asol file is set to: ${asolfile}"

echo "Is the data VFAINT? (yes or no if FAINT):"
```

```

set vfaint=(<)
echo "vfaint is set to: ${vfaint}"

echo "Please enter the GTI (...flt1.fits.gz) file (full path if \
not in current directory):"
set gtifile=(<)
echo "The GTI file is set to: ${gtifile}"

echo "Please enter the directory to store the new files (full \
path - end with /):"
set dirnew=(<)
echo "The new files will be stored in: ${dirnew}"

punlearn ardlb
pset ardlb AXAF_ACIS0_BADPIX_FILE = "${bad}[BADPIX0]"
pset ardlb AXAF_ACIS1_BADPIX_FILE = "${bad}[BADPIX1]"
pset ardlb AXAF_ACIS2_BADPIX_FILE = "${bad}[BADPIX2]"
pset ardlb AXAF_ACIS3_BADPIX_FILE = "${bad}[BADPIX3]"
pset ardlb AXAF_ACIS4_BADPIX_FILE = "${bad}[BADPIX4]"
pset ardlb AXAF_ACIS5_BADPIX_FILE = "${bad}[BADPIX5]"
pset ardlb AXAF_ACIS6_BADPIX_FILE = "${bad}[BADPIX6]"
pset ardlb AXAF_ACIS7_BADPIX_FILE = "${bad}[BADPIX7]"
pset ardlb AXAF_ACIS8_BADPIX_FILE = "${bad}[BADPIX8]"
pset ardlb AXAF_ACIS9_BADPIX_FILE = "${bad}[BADPIX9]"
plist ardlb

punlearn acis_process_events
pset acis_process_events infile=${events}
pset acis_process_events outfile= \
${dirnew}${obsid}_ciao_gain_evt1.fits
pset acis_process_events acaofffile="${asolfile}"
pset acis_process_events apply_cti=yes
pset acis_process_events apply_tgain=yes
pset acis_process_events gradefile=CALDB
pset acis_process_events gainfile=CALDB
pset acis_process_events badpixfile=${bad}
pset acis_process_events ctifile=CALDB
pset acis_process_events tgainfile=CALDB
pset acis_process_events eventdef=")stdlev1"
pset acis_process_events doevtgrade=yes
pset acis_process_events check_vf_pha=${vfaint}
pset acis_process_events calculate_pi=yes
pset acis_process_events verbose=2
pset acis_process_events stop=none
pset acis_process_events rand_pha=yes

```

```

pset acis_process_events rand_pix_size=0.5
acis_process_events

punlearn dmcop
dmcop "${dirnew}${obsid}_ciao_gain_evt1.fits[EVENTS][grade= \
0,2,3,4,6,status=0]" \
${dirnew}${obsid}_ciao_grade_evt1.fits opt=all verbose=3

punlearn dmcop
dmcop "${dirnew}${obsid}_ciao_grade_evt1.fits[EVENTS][@${gtifile}]" \
${dirnew}${obsid}_ciao_evt2.fits opt=all verbose=3

#exit

```

## A.2 Creating a cleaned event (evt2) file for *Chandra* data using the Penn State CTI corrector

```

#!/bin/csh
# Script to create an evt2 file from an evt1 file, using the CTI
# correction available in the Penn State corrector located at
# /usr/local/alocal/cti/cti/
# Use for ACIS-S, -110 or -120 , or ACIS-I, -110 data only (chips
# 0,1,2,3,6,7).
# Usage: With CIAO running, at prompt type "create_penn_evt2"

echo "Script to create spectra started ";date

echo "Please enter the observation number:"
set obsid=($<)
echo "The observation number is set to: ${obsid}"

echo "Please enter the bad pixel file (full path if not in current \
directory):"
set bad=($<)
echo "The bad pixel file is set to: ${bad}"

echo "Please enter the evt1 file (full path if not in current \
directory):"
set events=($<)
echo "The event 1 file is set to: ${events}"

```

```
echo "Please enter the asol file(s) (full path if not in current \
directory - comma separated list):"
set asolfile=($<)
echo "The asol file is set to: ${asolfile}"

echo "Is the data VFAINT? (yes or no if FAINT):"
set vfaint=($<)
echo "vfaint is set to: ${vfaint}"

echo "Please enter the GTI (...flt1.fits(.gz)) file (full path if \
not in current directory):"
set gtifile=($<)
echo "The GTI file is set to: ${gtifile}"

echo "Please enter the directory to store the new files (full \
path - end with /):"
set dirnew=($<)
echo "The new files will be stored in: ${dirnew}"

#echo "Please enter the chip number (0, 1, 2, 3, 6, or 7):"
#set chip=($<)
#echo "The chip number is set to: ${chip}"

echo "Please enter the temperature (110 or 120):"
set chiptemp=($<)
echo "The temperature is set to: -${chiptemp} degrees C"

punlearn ardlb
pset ardlb AXAF_ACIS0_BADPIX_FILE = "${bad}[BADPIX0]"
pset ardlb AXAF_ACIS1_BADPIX_FILE = "${bad}[BADPIX1]"
pset ardlb AXAF_ACIS2_BADPIX_FILE = "${bad}[BADPIX2]"
pset ardlb AXAF_ACIS3_BADPIX_FILE = "${bad}[BADPIX3]"
pset ardlb AXAF_ACIS4_BADPIX_FILE = "${bad}[BADPIX4]"
pset ardlb AXAF_ACIS5_BADPIX_FILE = "${bad}[BADPIX5]"
pset ardlb AXAF_ACIS6_BADPIX_FILE = "${bad}[BADPIX6]"
pset ardlb AXAF_ACIS7_BADPIX_FILE = "${bad}[BADPIX7]"
pset ardlb AXAF_ACIS8_BADPIX_FILE = "${bad}[BADPIX8]"
pset ardlb AXAF_ACIS9_BADPIX_FILE = "${bad}[BADPIX9]"
pset ardlb AXAF_ACIS0_QEU_FILE = \
"/usr/local/astrotools/public/${chiptemp}C/ccd0_${chiptemp}.geu"
pset ardlb AXAF_ACIS1_QEU_FILE = \
"/usr/local/astrotools/public/${chiptemp}C/ccd1_${chiptemp}.geu"
pset ardlb AXAF_ACIS2_QEU_FILE = \
"/usr/local/astrotools/public/${chiptemp}C/ccd2_${chiptemp}.geu"
```

```

pset ardlib AXAF_ACIS3_QEU_FILE = \
"/usr/local/astrotools/public/${chiptemp}C/ccd3_${chiptemp}.qeu"
pset ardlib AXAF_ACIS6_QEU_FILE = \
"/usr/local/astrotools/public/${chiptemp}C/ccd6_${chiptemp}.qeu"
pset ardlib AXAF_ACIS7_QEU_FILE = \
"/usr/local/astrotools/public/${chiptemp}C/ccd7_${chiptemp}.qeu"
plist ardlib

punlearn dmcoppy
dmcoppy "${events}[ccd_id=0,1,2,3,6,7]" ${dirnew}${obsid}_ccd_evt1.fits

#corrector version 1.45
setenv IDL_PATH '+/usr/local/alocal/cti/cti/: \
+/usr/local/alocal/cti/tara/: \
+/usr/local/alocal/cti/tara/event_browser/: \
+/usr/local/alocal/cti/tara/utilities/: \
+/usr/local/alocal/cti/tara/widget_tools/: \
+/usr/local/alocal/cti/astrotools/pro/'
setenv ASTRO_DATA /usr/local/alocal/cti/astrotools/data/

# perform correction & create $dirnew$obsid_ccd_evt1.no_cti.fits
/usr/local/alocal/cti/cti/correctit2 ${dirnew}${obsid}_ccd_evt1.fits \
",TEMPERATURE=-${chiptemp}"

mv correct_cti.log ${dirnew}correct_cti.log
mv ${obsid}_ccd_evt1.no_cti.fits \
${dirnew}${obsid}_ccd_evt1.no_cti.fits
mv ${obsid}_ccd_evt1.recalc.fits \
${dirnew}${obsid}_ccd_evt1.recalc.fits

punlearn acis_process_events
pset acis_process_events infile=${dirnew}${obsid}_ccd_evt1.no_cti.fits
pset acis_process_events outfile=${dirnew}${obsid}_penn_gain_evt1.fits
pset acis_process_events acaofffile="${asolfile}"
pset acis_process_events apply_cti=no
pset acis_process_events apply_tgain=yes
pset acis_process_events gradefile=NONE
pset acis_process_events gainfile=CALDB
pset acis_process_events badpixfile=${bad}
pset acis_process_events ctifile=NONE
pset acis_process_events tgainfile=CALDB
pset acis_process_events eventdef=")stdlev1"
pset acis_process_events doevtgrade=no
pset acis_process_events check_vf_pha=${vfaint}
pset acis_process_events calculate_pi=no

```

```

pset acis_process_events verbose=2
pset acis_process_events stop=none
pset acis_process_events rand_pha=yes
pset acis_process_events rand_pix_size=0.5
acis_process_events

punlearn dmcop
dmcop "${dirnew}${obsid}_penn_gain_evt1.fits[EVENTS] [grade= \
0,2,3,4,6,status=0]" \
${dirnew}${obsid}_penn_grade_evt1.fits opt=all verbose=3

punlearn dmcop
dmcop "${dirnew}${obsid}_penn_grade_evt1.fits[EVENTS] [@${gtifile}]" \
${dirnew}${obsid}_penn_evt2.fits opt=all verbose=3

#exit

```

### A.3 Creating a spectrum from data corrected for CTI with the CIAO CTI corrector

```

#!/bin/csh
# Script to create spectra for a given region, using the CTI
# correction available in CIAO.
# Use for ACIS-I, -120 data only.
# Uses mkacisrmf which only applies to -120 C, ACIS-0123567 data with
# the time dependent gain adjustment and the CTI correction applied.
# Usage: With CIAO running, at prompt type "create_ciao_spectrum"

echo "Script to create spectra started ";date

echo "Please enter the observation number:"
set obsid=($<)
echo "The observation number is set to: ${obsid}"

echo "Please enter the bad pixel file (full path if not in current \
directory):"
set bad=($<)
echo "The bad pixel file is set to: ${bad}"

echo "Please enter the evt2 file (full path if not in current \

```

```

directory):"
set events=($<)
echo "The event 2 file is set to: ${events}"

echo "Please enter the region file (full path if not in current \
directory):"
set regfile=($<)
echo "The region file is set to: ${regfile}"

echo "Please enter the name of the region to use for naming new \
files:"
set region=($<)
echo "The region is set to: ${region}"

echo "Please enter the background pi file (full path):"
set back=($<)
echo "The background pi file is set to: ${back}"

echo "Please enter the directory to store the new files (full \
path - end with /):"
set dirnew=($<)
echo "The new files will be stored in: ${dirnew}"

punlearn ardlb
pset ardlb AXAF_ACIS0_BADPIX_FILE = "${bad}[BADPIX0]"
pset ardlb AXAF_ACIS1_BADPIX_FILE = "${bad}[BADPIX1]"
pset ardlb AXAF_ACIS2_BADPIX_FILE = "${bad}[BADPIX2]"
pset ardlb AXAF_ACIS3_BADPIX_FILE = "${bad}[BADPIX3]"
pset ardlb AXAF_ACIS4_BADPIX_FILE = "${bad}[BADPIX4]"
pset ardlb AXAF_ACIS5_BADPIX_FILE = "${bad}[BADPIX5]"
pset ardlb AXAF_ACIS6_BADPIX_FILE = "${bad}[BADPIX6]"
pset ardlb AXAF_ACIS7_BADPIX_FILE = "${bad}[BADPIX7]"
pset ardlb AXAF_ACIS8_BADPIX_FILE = "${bad}[BADPIX8]"
pset ardlb AXAF_ACIS9_BADPIX_FILE = "${bad}[BADPIX9]"
plist ardlb

punlearn dmcop
dmcop "${events}[sky=region(${regfile})]" \
${dirnew}${obsid}_${region}_evt2.fits verbose=2

punlearn dmextract
pset dmextract infile="${dirnew}${obsid}_${region}_evt2.fits[bin pi]"
pset dmextract outfile=${dirnew}${obsid}_${region}.pi
pset dmextract wmap="[bin det=8]"
dmextract verbose=2

```

```
punlearn dmcopy
dmcopy "${dirnew}${obsid}_${region}_evt2.fits[energy=500:2000][bin \
det=8]" "${dirnew}${obsid}_${region}.wmap8 verbose=2
```

```
punlearn mkacisrmf
pset mkacisrmf infile=CALDB
pset mkacisrmf outfile=${dirnew}${obsid}_${region}.wrmf
pset mkacisrmf energy=0.1:11.0:0.01
pset mkacisrmf channel=1:1024:1
pset mkacisrmf chantype=pi
pset mkacisrmf wmap=${dirnew}${obsid}_${region}.wmap8
pset mkacisrmf gain=CALDB
mkacisrmf verbose=2
```

```
punlearn mkwarf
pset mkwarf infile=${dirnew}${obsid}_${region}.wmap8
pset mkwarf outfile=${dirnew}${obsid}_${region}.warf
pset mkwarf weightfile=${dirnew}${obsid}_${region}.wgt
#pset mkwarf egridspec=0.27:9.89:0.01
pset mkwarf egridspec="grid(${dirnew}${obsid}_${region}.wrmf[cols \
ENERG_LO,ENERG_HI])"
mkwarf verbose=2
```

```
punlearn dmhedit
dmhedit infile=${dirnew}${obsid}_${region}.pi filelist= \
operation=add key=RESPFILE \
value="'${dirnew}${obsid}_${region}.wrmf'"
```

```
dmhedit infile=${dirnew}${obsid}_${region}.pi filelist= \
operation=add key=ANCRFILE \
value="'${dirnew}${obsid}_${region}.warf'"
```

```
dmhedit infile=${dirnew}${obsid}_${region}.pi filelist= \
operation=add key=BACKFILE value="'${back}'"
```

```
#exit
```

## A.4 Creating a spectrum from data corrected for CTI with the Penn State CTI corrector

```
#!/bin/csh
# Script to create spectra for a given region, using the CTI
# correction from Penn State.
# Use for ACIS-S, -110 or -120 , or ACIS-I, -110 data only (chips
# 0,1,2,3,6,7).
# Usage: With CIAO running, at prompt type "create_penn_spectrum"

echo "Script to create spectra started ";date

echo "Please enter the observation number:"
set obsid=($<)
echo "The observation number is set to: ${obsid}"

echo "Please enter the bad pixel file (full path if not in current \
directory):"
set bad=($<)
echo "The bad pixel file is set to: ${bad}"

echo "Please enter the evt2 file (full path if not in current \
directory):"
set events=($<)
echo "The event 2 file is set to: ${events}"

echo "Please enter the region file (full path if not in current \
directory):"
set regfile=($<)
echo "The region file is set to: ${regfile}"

echo "Please enter the name of the region to use for naming new \
files:"
set region=($<)
echo "The region is set to: ${region}"

echo "Please enter the background pi file (full path):"
set back=($<)
echo "The background pi file is set to: ${back}"

echo "Please enter the directory to store the new files (full \
path - end with /):"
set dirnew=($<)
```

```

echo "The new files will be stored in: ${dirnew}"

echo "Please enter the temperature (110 or 120):"
set chiptemp=(<)
echo "The temperature is set to: -${chiptemp} degrees C"

echo "Please enter the rmf file to be used (full path):"
set rmffile=(<)
echo "The rmf file is set to: ${rmffile}"

punlearn ardlb
pset ardlb AXAF_ACIS0_BADPIX_FILE = "${bad}[BADPIX0]"
pset ardlb AXAF_ACIS1_BADPIX_FILE = "${bad}[BADPIX1]"
pset ardlb AXAF_ACIS2_BADPIX_FILE = "${bad}[BADPIX2]"
pset ardlb AXAF_ACIS3_BADPIX_FILE = "${bad}[BADPIX3]"
pset ardlb AXAF_ACIS4_BADPIX_FILE = "${bad}[BADPIX4]"
pset ardlb AXAF_ACIS5_BADPIX_FILE = "${bad}[BADPIX5]"
pset ardlb AXAF_ACIS6_BADPIX_FILE = "${bad}[BADPIX6]"
pset ardlb AXAF_ACIS7_BADPIX_FILE = "${bad}[BADPIX7]"
pset ardlb AXAF_ACIS8_BADPIX_FILE = "${bad}[BADPIX8]"
pset ardlb AXAF_ACIS9_BADPIX_FILE = "${bad}[BADPIX9]"
pset ardlb AXAF_ACIS0_QEU_FILE = \
"/usr/local/astrotools/public/${chiptemp}C/ccd0_${chiptemp}.qeu"
pset ardlb AXAF_ACIS1_QEU_FILE = \
"/usr/local/astrotools/public/${chiptemp}C/ccd1_${chiptemp}.qeu"
pset ardlb AXAF_ACIS2_QEU_FILE = \
"/usr/local/astrotools/public/${chiptemp}C/ccd2_${chiptemp}.qeu"
pset ardlb AXAF_ACIS3_QEU_FILE = \
"/usr/local/astrotools/public/${chiptemp}C/ccd3_${chiptemp}.qeu"
pset ardlb AXAF_ACIS6_QEU_FILE = \
"/usr/local/astrotools/public/${chiptemp}C/ccd6_${chiptemp}.qeu"
pset ardlb AXAF_ACIS7_QEU_FILE = \
"/usr/local/astrotools/public/${chiptemp}C/ccd7_${chiptemp}.qeu"
plist ardlb

punlearn dmcop
dmcop "${events}[sky=region(${regfile})]" \
${dirnew}${obsid}_${region}_evt2.fits verbose=2

punlearn dmextract
pset dmextract infile="${dirnew}${obsid}_${region}_evt2.fits [bin \
pi=1:685:1]"
pset dmextract outfile=${dirnew}${obsid}_${region}.pi
pset dmextract wmap="[bin det=8]"
dmextract verbose=2

```

```
punlearn dmcopu
dmcopu "${dirnew}${obsid}_${region}_evt2.fits[energy=500:2000][bin \
det=8]" "${dirnew}${obsid}_${region}.wmap8 verbose=2

punlearn mkwarf
pset mkwarf infile=${dirnew}${obsid}_${region}.wmap8
pset mkwarf outfile=${dirnew}${obsid}_${region}.warf
pset mkwarf weightfile=${dirnew}${obsid}_${region}.wgt
pset mkwarf egridspec="grid(${rmffile}[cols ENERG_LO,ENERG_HI])"
mkwarf verbose=2

punlearn dmhedit
dmhedit infile=${dirnew}${obsid}_${region}.pi filelist= \
operation=add key=RESPFILE \
value="'${rmffile}'"

dmhedit infile=${dirnew}${obsid}_${region}.pi filelist= \
operation=add key=ANCRFILE \
value="'${dirnew}${obsid}_${region}.warf'"

dmhedit infile=${dirnew}${obsid}_${region}.pi filelist= \
operation=add key=BACKFILE value="'${back}'"

#exit
```

# APPENDIX B

## XSPEC SPECTRAL MODELS

The observed intensity can be a combination of products and sums of models. The models used in this thesis are summarized below. Multiplicative models are denoted with an  $M$ , whereas additive models are denoted with an  $A$ . For example, the observed intensity for a spectrum fit by `wabs*(power+pshock)` would be

$$I(E) = M_{wabs}(E) (A_{power}(E) + A_{pshock}(E)) \quad (\text{B.1})$$

in units of photons per second per keV.

The following models are described in the *XSPEC* users' manual [2].

### B.1 `const`

Energy-independent multiplicative factor.

$$M_{const}(E) = factor \quad (\text{B.2})$$

### B.2 `wabs`

Photoelectric absorption using Wisconsin cross-sections. (Morrison & McCammon).

$$M_{wabs}(E) = e^{-N_H\sigma(E)} \quad (\text{B.3})$$

where  $\sigma(E)$  is the photo-electric cross-section, and  $N_{\text{H}}$  is the equivalent hydrogen column in units of  $10^{22} \text{ atoms cm}^{-2}$ .

### B.3 power

Simple photon power-law.

$$A_{\text{power}}(E) = KE^{-\alpha} \quad (\text{B.4})$$

where  $\alpha$  is the dimensionless photon index of the power-law and  $K$  is the normalization at 1 keV in units of  $\text{photons keV}^{-1} \text{ cm}^{-2} \text{ s}^{-1}$ .

### B.4 bbody

Blackbody spectrum.

$$A_{\text{body}}(E) = K \frac{8.0525 E^2 dE}{(kT)^4 (e^{E/kt} - 1)} \quad (\text{B.5})$$

where  $kT$  is the temperature in keV and  $K = \frac{L_{39}}{D_{10}^2}$  is the normalization where  $L_{39}$  is the source luminosity in units of  $10^{39} \text{ erg s}^{-1}$  and  $D_{10}$  is the distance to the source in units of 10 kpc.

### B.5 pshock

Constant temperature, plane-parallel shock plasma model.  $kT$  is the plasma temperature in keV.  $abund$  is metal (C, N, O, Ne, Mg, Si, S, Ar, Ca, Fe, Ni) abundances (He is fixed at cosmic abundance).  $\tau_l$  is the lower limit on the ionization timescale in  $\text{s cm}^{-3}$ .  $\tau_u$  is the upper limit on the ionization timescale in  $\text{s cm}^{-3}$ .  $z$  is the redshift.

$norm = \frac{10^{-14}}{4\pi[D_A(1+z)]^2} \int n_e n_H dV$ , where  $D_A$  is the angular size distance to the source in cm, and  $n_e$  and  $n_H$  are the electron and hydrogen densities in  $\text{cm}^{-3}$ .

## B.6 mekal

An emission spectrum from a hot diffuse gas based on the model calculations of Mewe and Kaastra with Fe L calculations by Liedahl. The model includes line emissions from several elements.  $kT$  is the plasma temperature in keV. *abund* is the metal (C, N, O, Ne, Na, Mg, Al, Si, S, Ar, Ca, Fe, Ni) abundances (He is fixed at cosmic abundance).  $z$  is the redshift.  $K$  is the normalization  $norm = \frac{10^{-14}}{4\pi D^2} \int n_e n_H dV$ , where  $D$  is the distance to the source in cm, and  $n_e$  and  $n_H$  are the electron and H densities, respectively, in  $\text{cm}^{-3}$ .

## B.7 gauss

Simple Gaussian line profile. If the width is  $\leq 0$ , the Gaussian is treated as a delta function.

$$A_{gauss}(E) = K \frac{1}{\sigma\sqrt{2\pi}} e^{-0.5\left(\frac{E-par1}{\sigma}\right)^2} \quad (\text{B.6})$$

where *par1* is the line energy in keV,  $\sigma$  is the line width in keV, and  $K$  is the normalization in units of photons  $\text{cm}^{-2} \text{s}^{-1}$ .

# APPENDIX C

## DATA TABLES FOR RADIAL PROFILES

The following tables contain the values used to create the radial profiles in Section 7.8.

Table C.1. Spectral fitting (*const\*wabs\*power*) results for radial profiles.<sup>a</sup>

radius	$N_{\text{H}}$ ( $\times 10^{22}$ atoms $\text{cm}^{-2}$ )	$\Gamma$	norm ( $10^{-3}$ photons $\text{keV}^{-1}$ $\text{cm}^{-2}$ $\text{s}^{-1}$ )	$\chi^2_{\nu}$ ( $\nu$ )
0''-5''	2.53 (2.49 - 2.57)	1.61 (1.59 - 1.63)	2.99 (2.89 - 3.10)	0.74 (8344)
5''-10''	2.50 (2.47 - 2.54)	1.74 (1.71 - 1.76)	3.05 (2.94 - 3.16)	0.73 (7670)
10''-15''	2.43 (2.40 - 2.46)	1.80 (1.78 - 1.82)	4.08 (3.95 - 4.21)	0.71 (9185)
15''-20''	2.38 (2.35 - 2.42)	1.88 (1.86 - 1.90)	3.67 (3.55 - 3.80)	0.67 (7993)
20''-25''	2.31 (2.27 - 2.35)	1.97 (1.94 - 2.00)	2.81 (2.70 - 2.93)	0.67 (6022)
25''-30''	2.25 (2.20 - 2.29)	2.01 (1.98 - 2.05)	2.18 (2.07 - 2.29)	0.59 (4716)
30''-35''	2.22 (2.15 - 2.28)	2.06 (2.01 - 2.11)	1.29 (1.21 - 1.39)	0.54 (2885)
35''-40''	2.13 (2.02 - 2.25)	2.10 (2.02 - 2.19)	0.61 (0.54 - 0.69)	0.47 (1423)
40''-45''	1.93 (1.74 - 2.13)	2.05 (1.91 - 2.21)	0.28 (0.23 - 0.35)	0.39 (709)
45''-55''	1.77 (1.58 - 1.97)	2.07 (1.90 - 2.25)	0.37 (0.30 - 0.47)	0.35 (576)
55''-65''	1.84 (1.63 - 2.05)	2.21 (2.03 - 2.40)	0.42 (0.33 - 0.54)	0.32 (564)
65''-75''	1.75 (1.57 - 1.95)	2.10 (1.93 - 2.28)	0.39 (0.31 - 0.50)	0.34 (609)
75''-85''	1.55 (1.40 - 1.70)	1.98 (1.85 - 2.12)	0.42 (0.35 - 0.51)	0.40 (799)
85''-95''	1.74 (1.57 - 1.92)	2.06 (1.90 - 2.22)	0.43 (0.35 - 0.54)	0.38 (738)
95''-105''	1.74 (1.57 - 1.93)	2.06 (1.90 - 2.23)	0.43 (0.35 - 0.54)	0.37 (731)
105''-115''	1.70 (1.51 - 1.91)	2.06 (1.89 - 2.24)	0.39 (0.31 - 0.50)	0.35 (703)
115''-125''	1.80 (1.59 - 2.03)	2.15 (1.95 - 2.35)	0.42 (0.32 - 0.55)	0.35 (672)
125''-135''	1.75 (1.54 - 1.98)	2.10 (1.91 - 2.30)	0.38 (0.30 - 0.50)	0.38 (686)
135''-145''	1.77 (1.53 - 2.03)	2.04 (1.82 - 2.27)	0.33 (0.25 - 0.45)	0.38 (647)
145''-155''	1.72 (1.39 - 2.10)	2.24 (1.92 - 2.60)	0.26 (0.17 - 0.40)	0.37 (486)
155''-165''	1.71 (1.28 - 2.22)	2.49 (2.04 - 3.03)	0.20 (0.11 - 0.39)	0.40 (380)

<sup>a</sup>All confidence ranges are 90%.Table C.2. Spectral fitting (*const\*wabs\*power*) results for radial profiles when  $N_{\text{H}} = 2.33 \times 10^{22}$  atoms  $\text{cm}^{-2}$ .<sup>a</sup>

radius	$\Gamma$	norm ( $10^{-3}$ photons $\text{keV}^{-1}$ $\text{cm}^{-2}$ $\text{s}^{-1}$ )	$\chi^2_{\nu}$ ( $\nu$ )
0''-5''	1.50 (1.48 - 1.51)	2.51 (2.47 - 2.54)	0.75 (8345)
5''-10''	1.64 (1.62 - 1.65)	2.61 (2.57 - 2.65)	0.73 (7671)
10''-15''	1.74 (1.73 - 1.75)	3.71 (3.66 - 3.75)	0.71 (9186)
15''-20''	1.85 (1.84 - 1.86)	3.49 (3.45 - 3.54)	0.67 (7994)
20''-25''	1.98 (1.97 - 2.00)	2.87 (2.83 - 2.92)	0.67 (6023)
25''-30''	2.07 (2.05 - 2.09)	2.37 (2.32 - 2.41)	0.60 (4717)
30''-35''	2.13 (2.11 - 2.15)	1.45 (1.41 - 1.49)	0.54 (2886)
35''-40''	2.23 (2.20 - 2.25)	0.74 (0.71 - 0.78)	0.48 (1424)
40''-45''	2.33 (2.26 - 2.39)	0.42 (0.39 - 0.45)	0.40 (710)
45''-55''	2.50 (2.42 - 2.59)	0.67 (0.62 - 0.73)	0.38 (577)
55''-65''	2.59 (2.51 - 2.68)	0.71 (0.65 - 0.78)	0.34 (565)
65''-75''	2.55 (2.47 - 2.64)	0.73 (0.66 - 0.79)	0.38 (610)
75''-85''	2.61 (2.54 - 2.69)	1.00 (0.93 - 1.08)	0.47 (800)
85''-95''	2.52 (2.44 - 2.60)	0.81 (0.75 - 0.88)	0.41 (739)
95''-105''	2.52 (2.44 - 2.61)	0.81 (0.75 - 0.88)	0.40 (732)
105''-115''	2.55 (2.46 - 2.64)	0.77 (0.70 - 0.85)	0.38 (704)
115''-125''	2.56 (2.47 - 2.66)	0.74 (0.67 - 0.82)	0.37 (673)
125''-135''	2.55 (2.45 - 2.66)	0.71 (0.64 - 0.79)	0.34 (687)
135''-145''	2.47 (2.36 - 2.59)	0.61 (0.54 - 0.68)	0.40 (648)
145''-155''	2.75 (2.59 - 2.93)	0.50 (0.43 - 0.59)	0.39 (487)
155''-165''	3.07 (2.81 - 3.35)	0.43 (0.34 - 0.54)	0.41 (381)

<sup>a</sup>All confidence ranges are 90%.

# GLOSSARY

**ACIS** The Advanced CCD Imaging Spectrometer.

**ARF** Ancillary Response Function.

**BI** Back Illuminated (CCD).

**CALDB** CALibration DataBase.

**CCD** Charge Coupled Device.

**CIAO** Chandra Interactive Analysis of Observations.

**CTI** Charge Transfer Inefficiency.

**CXC** Chandra X-ray Center.

**CXO** Chandra X-ray Observatory.

**Dec** Declination (also denoted  $\delta$ ).

**FI** Front Illuminated (CCD).

**FITS** Flexible Image Transport System.

**FWHM** Full Width at Half Maximum.

**GTI** Good Time Interval.

**HRC** The High Resolution Camera.

**ISM** InterStellar Medium.

**NS** Neutron Star.

**PSF** Point-Spread Function.

**PSR** PulSaR.

**PWN(e)** Pulsar Wind Nebula(e).

**RA** Right Ascension (also denoted  $\alpha$ ).

**RMF** Redistribution Matrix Function.

**SN(e)** SuperNova(e).

**SNR** SuperNova Remnant.

**XSPEC** X-ray SPECtral Fitting Package.

# BIBLIOGRAPHY

- [1] W. J. Altenhoff, D. Downes, T. Pauls, and J. Schraml. Survey of the Galactic Plane at 4.875 GHz. *Astronomy & Astrophysics Supplement Series*, 35:23–54, 1978.
- [2] K. Arnaud, B. Dorman, and C. Gordon. *Xspec: An X-ray Spectral Fitting Package*. HEASARC, Exploration of the Universe Division, NASA/GSFC, 2006. <http://heasarc.nasa.gov/docs/xanadu/xspec/manual/manual.html>.
- [3] I. Asaoka and K. Koyama. Do all the Crab-like supernova remnants have an X-ray photon index near a value of 2? *Publ. Astron. Soc. Japan*, 42:625–632, 1990.
- [4] R. Bandiera and F. Bocchino. The X-ray halo of G21.5-0.9. *Advances in Space Research*, 33:398–402, 2004.
- [5] R.H. Becker and M.R. Kundu. High-resolution radio observations of three supernova remnants. *The Astrophysical Journal*, 204:427–440, 1976.
- [6] R.H. Becker and A.E. Szymkowiak. High resolution X-ray and radio images of the Crab-like supernova remnant G21.5-0.9. *The Astrophysical Journal*, 248:L23–L26, 1981.
- [7] W. Becker and J. Trümper. The X-ray luminosity of rotation-powered neutron stars. *Astronomy & Astrophysics*, 326:682–691, 1997.

- [8] J. D. Biggs and A. G. Lyne. A search for radio pulsars in globular clusters, supernova remnants and transient X-ray sources. *Mon. Not. R. Astron. Soc.*, 282:691–698, 1996.
- [9] F. Bocchino. Detection of thermal X-ray emission in the halo of the plerionic supernova remnant G21.5-0.9. *Advances in Space Research*, 35:1003–1006, 2005.
- [10] F. Bocchino, E. van der Swaluw, R. Chevalier, and R. Bandiera. The nature of the X-ray halo of the plerion G21.5-0.9 unveiled by XMM-Newton and Chandra. *Astronomy & Astrophysics*, 442:539–548, 2005.
- [11] D.C.-J. Bock, M.C.H. Wright, and J.R. Dickel. The Crab-like supernova remnant G21.5-0.9 at millimeter wavelengths. *The Astrophysical Journal*, 561:L203–L206, 2001.
- [12] R. L. Bowers and T. Deeming. *Astrophysics I: Stars*. Jones and Bartlett Publishers, Inc., 1984.
- [13] R. L. Bowers and T. Deeming. *Astrophysics II: Interstellar Matter and Galaxies*. Jones and Bartlett Publishers, Inc., 1984.
- [14] F. Camilo, S. M. Ransom, B. M. Gaensler, P. O. Slane, D. R. Lorimer, J. Reynolds, R. N. Manchester, and S. S. Murray. PSR J1833-1034: Discovery of the central young pulsar in the supernova remnant G21.5-0.9. *The Astrophysical Journal*, 637:456–465, 2006.
- [15] B. W. Carroll and D. A. Ostlie. *An Introduction to Modern Astrophysics*. Addison-Wesley Publishing Company, Inc., 1996.

- [16] Chandra X-ray Center, Chandra Project Science, MSFC, and Chandra IPI Teams. *The Chandra Proposers' Observatory Guide*. Smithsonian Institution, 2005. <http://cxc.harvard.edu/proposer/POG/index.html>.
- [17] P. A. Charles and F. D. Seward. *Exploring The X-ray Universe*. Cambridge University Press, 1995.
- [18] J. Davelaar, A. Smith, and R.H. Becker. X-ray spectral observations of the Crab-like supernova remnants G21.5-0.9 and 3C 58. *The Astrophysical Journal*, 300:L59–L62, 1986.
- [19] T. DeLaney, B. M. Gaensler, J. Arons, and M. J. Pivovarov. Time variability in the X-ray nebula powered by pulsar B1509-58. *The Astrophysical Journal*, 640:929–940, 2006.
- [20] E. Fürst, T. Handa, K. Morita, P. Reich, W. Reich, and Y. Sofue. Detection of axisymmetric filaments in the filled-center supernova remnant G21.5-0.9. *Publ. Astron. Soc. Japan*, 40:347–356, 1988.
- [21] Y.A. Gallant and R.J. Tuffs. Infrared observations of plerionic supernova remnants: High-energy astrophysics with ISO. In *Proceedings of the Conference "The Universe as seen by ISO", Paris, France, 20-23 October 1998*, pages 313–316. ESA, 1999.
- [22] D. A. Green. *A Catalogue of Galactic Supernova Remnants (2006 April version)*. Astrophysics Group, Cavendish Laboratory, Cambridge, United Kingdom, 2006. <http://www.mrao.cam.ac.uk/surveys/snrs/>.

- [23] Y. Gupta, D. Mitra, D. A. Green, and A. Acharyya. GMRT discovery of PSR J1833-1034: the pulsar associated with the supernova remnant G21.5-0.9. *Current Science*, 89, 2005.
- [24] J. J. Hester, K. Mori, D. Burrows, J. S. Gallagher, J. R. Graham, M. Halverson, A. Kader, F. C. Michel, and P. Scowen. Hubble Space Telescope and Chandra monitoring of the Crab Synchrotron Nebula. *The Astrophysical Journal*, 577:L49–L52, 2002.
- [25] N. E. Kassim. 330 MHz VLA observations of 20 Galactic supernova remnants. *The Astronomical Journal*, 103:943–952, 1992.
- [26] C. F. Kennel and F. V. Coroniti. Confinement of the Crab Pulsar’s wind by its supernova remnant. *The Astrophysical Journal*, 283:694–709, 1984.
- [27] C. F. Kennel and F. V. Coroniti. Magnetohydrodynamic model of Crab Nebula radiation. *The Astrophysical Journal*, 283:710–730, 1984.
- [28] M. G. F. Kirsch, G. Schönherr, E. Kendziorra, M. J. Freyberg, M. Martin, J. Wilms, K. Mukerjee, and M. G. Breittellner. The XMM-Newton view of the Crab. *Astronomy & Astrophysics*, 453:173–180, 2006.
- [29] M. S. Longair. *High Energy Astrophysics I: Particles, photons, and their detection*. Cambridge University Press, 1992.
- [30] M. S. Longair. *High Energy Astrophysics II: Stars, the Galaxy and the interstellar medium*. Cambridge University Press, 1994.

- [31] D. Lorimer and M. Kramer. *Handbook of Pulsar Astronomy*. Cambridge University Press, 2005.
- [32] H. Matheson and S. Safi-Harb. The plerionic supernova remnant G21.5-0.9: In and out. *Advances in Space Research*, 35:1099–1105, 2005.
- [33] H.W. Morsi and W. Reich. 32 GHz radio continuum observations of four plerionic supernova remnants. *Astronomy & Astrophysics Supplement Series*, 69:533–540, 1987.
- [34] C.-Y. Ng and R. W. Romani. Fitting pulsar wind tori. *The Astrophysical Journal*, 601:479–484, 2004.
- [35] N. La Palombara and S. Mereghetti. Timing analysis of the core of the Crab-like SNR G21.5-0.9. *Astronomy & Astrophysics*, 383:916–918, 2002.
- [36] G. G. Pavlov, M. A. Teter, O. Kargaltsev, and D. Sanwal. The variable jet of the Vela Pulsar. *The Astrophysical Journal*, 591:1157–1171, 2003.
- [37] S. Roy and M. Watzke. *Cosmic Shell-Seekers Find a Beauty*. CXC Release 05-05, 2005. [http://chandra.harvard.edu/press/05\\\_releases/press\\\_041905.html](http://chandra.harvard.edu/press/05\_releases/press\_041905.html).
- [38] S. Safi-Harb, I.M. Harrus, R. Petre, G.G. Pavlov, A.B. Koptsevich, and D. Sanwal. X-ray observations of the supernova remnant G21.5-0.9. *The Astrophysical Journal*, 561:308–320, 2001.

- [39] C. J. Salter, D. T. Emerson, H. Steppe, and C. Thum. Observations at 90 and 142 GHz of nine extended galactic radio sources. *Astronomy & Astrophysics*, 225:167–178, 1989.
- [40] C. J. Salter, S. P. Reynolds, D. E. Hogg, J. M. Payne, and P. J. Rhodes. 84 GHz observations of five Crab-like supernova remnants. *The Astrophysical Journal*, 338:171–177, 1989.
- [41] F. D. Seward, P. Gorenstein, and R. K. Smith. Chandra observations of the X-ray halo around the Crab Nebula. *The Astrophysical Journal*, 636:873–880, 2006.
- [42] F. D. Seward and Z.-R. Wang. Pulsars, X-ray synchrotron nebulae, and guest stars. *The Astrophysical Journal*, 332:199–205, 1988.
- [43] S. L. Shapiro and S. A. Teukolsky. *Black Holes, White Dwarfs, and Neutron Stars: The Physics of Compact Objects*. John Wiley & Sons, 1983.
- [44] P. Slane, Y. Chen, N.S. Schulz, F.D. Seward, J.P. Hughes, and B.M. Gaensler. Chandra observations of the Crab-like supernova remnant G21.5-0.9. *The Astrophysical Journal*, 533:L29–L32, 2000.
- [45] S.L. Snowden. Comparison of XMM-Newton EPIC, Chandra ACIS-S3, ASCA SIS and GIS, and ROSAT PSPC results for G21.5-0.9, 1E0102.2-7219, and MS1054.4-0321. In *Proceedings of the Symposium 'New Visions of the X-ray Universe in the XMM-Newton and Chandra Era' 26-30 November 2001*, 2001.

- [46] L. K. Townsley, P. S. Broos, G. P. Garmire, and J. A. Nousek. Mitigating charge transfer inefficiency in the Chandra X-ray Observatory Advanced CCD Imaging Spectrometer. *The Astrophysical Journal*, 534:L139–L142, 2000.
- [47] B.J. Wallace, T.L. Landecker, and A.R. Taylor. HI voids around filled-center supernova remnants. *Astronomy & Astrophysics*, 286:565–578, 1994.
- [48] R.S. Warwick, J-P. Bernard, F. Bocchino, and et.al. The extended X-ray halo of the Crab-like SNR G21.5-0.9. *Astronomy & Astrophysics*, 365:L248–L253, 2001.
- [49] K. W. Weiler and R. A. Sramek. Supernovae and supernova remnants. *Annual Review of Astronomy & Astrophysics*, 26:295–341, 1988.
- [50] A. S. Wilson and K. W. Weiler. G21.5-0.9 - A supernova remnant resembling the Crab Nebula. *Astronomy & Astrophysics*, 53:89–92, 1976.